

Sayyed Ahmad Alavian

Modeling CO₂ Injection in Fractured Reservoirs Using Single Matrix Block Systems

Thesis for the degree of Philosophiae Doctor

Trondheim, October 2011

Norwegian University of Science and Technology
Faculty of Engineering Science and Technology
Department of Petroleum Engineering and Applied
Geophysics



NTNU – Trondheim
Norwegian University of
Science and Technology

NTNU

Norwegian University of Science and Technology

Thesis for the degree of Philosophiae Doctor

Faculty of Engineering Science and Technology
Department of Petroleum Engineering and Applied Geophysics

© Sayyed Ahmad Alavian

ISBN 978-82-471-2735-3 (printed ver.)
ISBN 978-82-471-2736-0 (electronic ver.)
ISSN 1503-8181

Doctoral theses at NTNU, 2011:101

Printed by NTNU-trykk

To my Hometown

Abstract

In this thesis, CO₂ injection in matrix/fracture systems has been studied using a finely-gridded compositional simulator representing a single matrix block. Three laboratory experiments were modeled to investigate whether CO₂ injection in a fracture-matrix system could be simulated using commercial simulators that include basic fluid flow physics, phase behavior, and molecular diffusion.

The first experiment was performed by Karimaie (2007) using an equilibrium, saturated gas-oil fluid system (C₁-n-C₇) at 220 bar and 85 °C. Because no recovery was expected from non-equilibrium thermodynamic mass transfer, reported recovery stemmed only from Darcy displacement driven by gravity and capillary forces. When the oil production stopped from the equilibrium gas displacement, a second injection period with pure CO₂ followed.

The numerical modeling was conducted using a compositional reservoir simulator (SENSOR) without diffusion. The 2-dimensional r-z model used fine grids for the core matrix and surrounding fracture. Automated history matching was used to determine parameters which were not accurately known (fracture permeability, fracture and matrix porosity, and separator conditions), using surface volumetric oil production rates reported experimentally. The final model match was relatively unique with a high degree of confidence in final model parameters. The oil recovery improved significantly with CO₂ injection.

Our model indicated that the recovery mechanism in the Karimaie experiment was dominated, for both equilibrium gas and CO₂ injection, by top-to-bottom Darcy displacement caused by low conductivity in the artificial fracture; little impact of capillary-gravity displacement was found. Changes in CO₂ injection rate had a significant impact on recovery performance. This experiment was also

modeled using ECL300, with the same production performance as SENSOR for the set of history-match parameters determined without diffusion. When molecular diffusion was used in ECL300, results were nearly identical with those found without diffusion.

Two other experiments were performed by Darvish (2007) at a higher temperature and pressure (130 °C and 300 bara) using a similar chalk and live reservoir oil. A similar modeling approach to that described above was also used for these experiments. In both experiments, the matching process based on reported oil production data gave a high degree of confidence in the model. The reported experimental mass fractions of produced-stream components were also matched well.

Our modeling study indicates that gravity drainage affects the displacement process, but that mass transfer – including vaporization, condensation and molecular diffusion – also impact the recovery performance of CO₂ injection in the Darvish experiments. The CO₂ injection rate and initial water saturation were investigated by comparing the two Darvish experiments.

Our studies from all of the Karimaie and Darvish experiments show a strong influence of the surface separator temperature on surface oil production, and this is an important consideration in designing and interpreting laboratory production data consistently.

Once the laboratory recovery mechanisms had been successfully modeled, predictive numerical simulation studies were conducted on field-scale matrix/fractured systems, albeit mostly for single matrix blocks surrounded by a fracture. The effects of several key parameters on recovery production performance were studied in detail for field-scale systems: matrix permeability, matrix block size, matrix-matrix capillary continuity (stacked blocks), and the use of mixtures containing CO₂ and hydrocarbon gas.

The field-scale results were affected by gridding, so grid was refined to the degree necessary to achieve a more-or-less converged solution – i.e. recovery production performance didn't change with further refinement.

We studied the effect of molecular diffusion on oil recovery by CO₂ injection in laboratory experiments and field-scale systems. Because the fluid systems considered had complex phase behavior and a wide range of conditions from strongly immiscible to near-miscible, the diffusion driving potential used was *total component potential* including chemical and gravity effects; concentration-driven diffusion did not represent the more-complex non-equilibrium CO₂ injection processes observed in the laboratory tests.

A key result of this study was that diffusion can have an important effect on oil recovery, and that this effect varies with matrix block size and CO₂ injection rate. We have shown that diffusion has a dominant effect on the recovery mechanism in experimental tests, except at very low rates of CO₂ injection (and equilibrium hydrocarbon gas injection). For the field-scale matrix/fracture systems, diffusion can have a significant effect on the rate of recovery, with the effect becoming noticeable for low reservoir pressures and/or matrix block sizes less than ~40 ft.

Acknowledgements

I would like to especially thank my supervisor and close friend Professor Curtis H. Whitson for guiding me through this work. The thesis would not have been possible without his advice, valuable discussion and support.

Special thanks to Dr. Hassan Karimaie and Dr. Gholam Reza Darvish who made their experimental data available to me, and provided helpful discussions during my modeling of their experiments.

All colleagues and staff at the Department of Petroleum Engineering and Applied Geophysics at NTNU are greatly acknowledged for their cooperation and for creating a very good working environment. For this I would like to thank Marit Valle Raaness, Tone Sanne, Madelein Wold, Ann Lisa Brekken, Turid Halvorsen, Solveig Johnsen and Turid Oline Uvsløkk.

I acknowledge the financial support from Shell and PERA.

Thanks to PERA staff engineers: Dr. Kameshwar Singh, Dr. Mohammad Faizul Hoda, Snjezana Sunjerga and Sissel Ø. Martinsen and also Dr. Øivind Fevang and Dr. Knut G. Uleberg (now at Sataoil) for providing software and helping me during the thesis. I enjoyed and benefited a lot from working with them.

Sincere thanks to Arif Kuntadi and Mohammad Ghasemi for introducing me to Ruby programming.

I wish to express my deepest gratitude to my mother for all support, encouragement and inspiration throughout my life. I am also indebted to my wife and my son for understanding, patience and support during the work of this thesis.

Finally, I would also like to thank all my family members and close friends for support and encouragement.

Sayyed Ahmad Alavian

List of Papers

Throughout this PhD work, five papers were written by the author of this thesis, together with co-author. One paper is published in a reviewed journal, three papers are under review for publishing and also presented in SPE conference. One paper will be presented at an upcoming SPE conference. The papers are included at the end of the thesis.

1. Alavian, S.A., and Whitson C.H. 2010. CO₂ EOR Potential in Naturally-Fractured Haft Kel Field, Iran. SPE Reservoir Evaluation and Engineering: 720-729. SPE-139528-PA.
2. Alavian, S.A., and Whitson C.H. 2009. Modeling CO₂ Injection in a Fractured-Chalk Experiment. Paper SPE 125362 presented at the 2009 SPE/EAGE Reservoir Characterization and Simulation Conference, Abu Dhabi, UAE, 19–21 October.
(Accepted for publication in the Journal of Petroleum Science and Engineering)
3. Alavian, S.A., and Whitson C.H. 2010. Scale Dependence of Diffusion in Naturally Fractured Reservoirs for CO₂ Injection. Paper SPE 129666 presented at the 2010 SPE Improved Oil Recovery Symposium, Tulsa, Oklahoma, USA, 24–28 April.
(The paper is under review for publication in the Journal of Petroleum Science and Engineering)
4. Alavian, S.A., and Whitson C.H. 2010. Modeling CO₂ Injection Including Diffusion in a Fractured-Chalk Experiment. Paper SPE 135339 presented at the 2010 Annual Technical Conference and Exhibition, Florence, Italy, 19–22 September.

(The paper is under review for publication in the Journal of Petroleum Science and Engineering)

5. Alavian, S.A., and Whitson C.H. 2011. Modeling CO₂ Injection Including Diffusion in a Fractured-Chalk Experiment with Initial Water Saturation. Will be presented at SPE Conference.

Table of Contents

Abstract	i
Acknowledgements	v
List of Paper	vii
Table of Contents	ix
List of Tables	xv
List of Figures	xvii
Nomenclature	xxv
Chapter 1 Introduction	1
1.1 Background	1
1.2 Thesis Outline	3
1.3 Reference	4
Chapter 2 Fundamentals and Calculations	7
2.1 Introduction	7
2.2 Diffusion	7
2.2.1 Diffusion Coefficient	8
2.2.2 Diffusion Coefficient in Multicomponent System	10
2.2.3 Diffusion Coefficient in Porous Media	10
2.3 Relative Permeability and Capillary Pressure Curve	11
2.3.1 Three Phase Relative Permeability	12
2.3.2 Capillary Pressure Scaling with IFT	12
2.4 Minimum Miscibility Condition	12

2.4.1 MMP calculation	13
2.5 Numerical Gridding	14
2.6 Reference	14
Chapter 3 Modeling CO₂ Injection in Karimaie Fractured Chalk	
Experiment	19
3.1 Introduction	19
3.2 Rock and Fluid Properties	20
3.3 Experimental Procedure	22
3.4 Uncertainties and error sources	23
3.5 Model Description	24
3.6 Matching Experimental Data	25
3.6.1 Fracture Permeability	25
3.6.2 Equilibrium Gas Injection Rate	28
3.6.3 CO ₂ Injection Rates	29
3.6.4 Surface Separation	30
3.6.5 Regression Parameters	31
3.7 Recovery Mechanism	32
3.8 Designing Fractured Reservoir Experiments using CO ₂	43
3.9 Conclusions	44
3.10 Reference	44
Chapter 4 Modeling CO₂ Injection in Darvish Fractured Chalk	
Experiment (Sw=0%)	47
4.1 Introduction	47
4.2 Rock and Fluid Properties	48
4.3 Experimental Procedure	53

4.4 Model Description.....	54
4.5 Matching Experimental Data	55
4.6 Recovery Mechanism.....	58
4.7 Conclusions	62
4.8 Reference.....	66

Chapter 5 Modeling CO₂ Injection in Darvish Fractured Chalk

Experiment (Sw=26%).....	67
5.1 Introduction	67
5.2 Rock and Fluid Properties	68
5.3 Experimental Procedure	68
5.4 Model Description.....	71
5.5 Matching Experimental Data	72
5.6 CO ₂ Injection Rate Effect	78
5.6.1 Oil Recovery	78
5.6.2 CO ₂ Map Profile	81
5.7 Grid Sensitivity	81
5.8 Diffusion Coefficients Effect	81
5.9 Conclusions	85
5.10 Reference.....	86

Chapter 6 CO₂ Injection in Naturally Fractured Reservoirs – Haft Kel

Study without Diffusion	89
6.1 Introduction	89
6.2 Description of Model	90
6.3 Grid Sensitivity	93
6.4 Prediction of Minimum Miscibility Pressure (MMP).....	94

6.5 Injection-Gas Mechanism.....	95
6.5.1 Equilibrium Gas in a Single Matrix Block.....	95
6.5.2 Mechanism of CO ₂ in a Single Matrix Block	97
6.5.2.1 CO ₂ Lighter Than Oil.....	98
6.5.2.2 CO ₂ Heavier Than Oil.....	104
6.6 Injection-Gas Effect	105
6.6.1 CO ₂ -Dilution Effect	106
6.6.2 Tertiary Recovery by CO ₂ Injection	106
6.6.3 Reservoir-Pressure Effect.....	108
6.7 Matrix-Block Height Effect	110
6.8 Matrix-Block-Permeability Effect.....	112
6.9 Block-to-Block Interaction.....	114
6.10 Conclusions	116
6.11 References	117
Chapter 7 CO₂ Injection in Naturally Fractured Reservoirs – Lab and	
Field Modeling Studies with Diffusion	119
7.1 Introduction	119
7.2 Description of Matrix/Fracture Models.....	120
7.2.1 Haft Kel Field-Scale Model	120
7.2.2 Laboratory Model.....	121
7.3 CO ₂ Displacement Mechanism	123
7.3.1 Lab Test Recovery Performance	123
7.3.2 Field-Scale (Haft Kel) Recovery Performance	126
7.4 Reservoir Pressure Sensitivity.....	128
7.4.1 Core Model.....	128

7.4.2 Field-Scale Matrix	130
7.5 Matrix Block Permeability Sensitivity	131
7.6 Matrix Block Size Sensitivity	131
7.7 Injection Rate Sensitivity	133
7.8 Conclusions	137
7.9 References	138

Appendix A: Simulator Input Data Sets**Appendix B: Papers**

List of Tables

Table 3.1 – Comparison of Reported Oil and Gas Compositions by Karimaie (2007) and Recalculated Compositions Using His Reported EOS. . .	21
Table 3.2 – EOS Properties for SRK Characterization	22
Table 3.3 – SRK Binary Interaction Parameters	22
Table 3.4 – Measured Cumulative Oil and Gas Production.....	26
Table 3.5 – Regression Variables.....	31
Table 3.6 – Diffusion Coefficients for Oil and Gas Phase.....	41
Table 4.1 – Fluid Properties for the 13-Component Peng-Robinson Characterization.	52
Table 4.2 – Binary Interaction Coefficients for the 13-Component Peng-Robinson Characterization.	52
Table 4.3 – Fluid Composition and K-Value at Saturation Pressure (242 bara) an 130 °C	53
Table 4.4 – Gas and Oil Diffusion Coefficients and Initial Oil Composition.....	56
Table 6.1 – Matrix and Fracture Fixed Dimensions and Properties.....	91
Table 6.2 – Fluid Properties For The 11-Component SRK Characterization	91
Table 6.3 – BIPs for The 11-Component SRK Characterization	92
Table 6.4 – Oil Composition for The 11-Component EOS at Different Saturation Pressures	92
Table 6.5 – Equilibrium-Gas Composition for The 11-Component EOS at Different Saturation Pressures.....	93
Table 7.1 – Fluid Properties for The 3 Component SRK Characterization	122

Table 7.2 – Binary Interaction Coefficients for The 3 Component SRK	
Characterization	122
Table 7.3 – Oil Composition for The 3 Component EOS at Different Saturation	
Pressures and Diffusion Coefficients	122
Table 7.4 – Oil Composition for The 11 Component EOS at Different Saturation	
Pressures and Diffusion Coefficients	123

List of Figures

Figure 3.1 – Measured oil production without considering early produced oil and simulation result of assuming gravity-drainage mechanism	27
Figure 3.2 – Early measured oil production of the experiment and simulation results of 5 cm ³ /min injection rate and best fit	28
Figure 3.3 – Measured gas production with matched simulation result and results of 0.1 cm ³ /min injection rate	29
Figure 3.4 – Reported and model gas injection rate profile during the experiment	30
Figure 3.5 – Measured oil production with matched simulation results of equilibrium gas injection period	32
Figure 3.6 – Measured oil production with matched simulation result of equilibrium gas injection and CO ₂ injection periods	33
Figure 3.7 – Core oil saturation profile during equilibrium gas injection period from numerical model with linear core relative permeability	34
Figure 3.8 – Oil saturation map of core after 2.4 hours for matched model with linear core relative permeability (at about 18% oil recovery)	35
Figure 3.9 – Oil saturation map of core after 1 day for matched model with linear core relative permeability (at about 54% oil recovery)	36
Figure 3.10 – Oil saturation map of core after 4.2 day for matched model with linear core relative permeability (at about 70% oil recovery)	37
Figure 3.11 – Saturation pressure versus injected CO ₂ mole percent calculated by swelling test for 1 and 0.4 oil saturation	38
Figure 3.12 – Profile of average oil saturation in the core during equilibrium gas and CO ₂ injection period with and without diffusion	38

Figure 3.13 – CO ₂ mole fraction map of core after 4.25 days for matched model without diffusion effect.....	39
Figure 3.14 – CO ₂ mole fraction map of core after 4.25 days for matched model with diffusion effect.....	40
Figure 3.15 – Profile of CO ₂ gas mole fraction and gas saturation in the core during CO ₂ injection period	41
Figure 3.16 – Profile of n-C ₇ gas mole fraction and gas saturation in the core during CO ₂ injection period	42
Figure 3.17 – Calculated oil recovery factor based on core oil saturation.....	43
Figure 4.1 – Measured and calculated total (gas + oil) density at 130 °C.....	49
Figure 4.2 – Measured and calculated differential oil volume factor at 130 °C.	49
Figure 4.3 – Measured and calculated liquid saturation at 130 °C.....	50
Figure 4.4 – Measured and calculated saturation pressure versus CO ₂ mole injected at 130 °C from CO ₂ swelling test.....	50
Figure 4.5 – Measured and calculated liquid saturation for different CO ₂ mol-% mixtures from CO ₂ swelling test	51
Figure 4.6 – Measured and calculated saturated oil viscosity versus CO ₂ liquid mole fraction at 130 °C	51
Figure 4.7 – Measured and calculated saturated oil viscosity versus CO ₂ liquid mole fraction at 130 °C	56
Figure 4.8 – Measured produced oil mass with matched simulation results for two set of core relative permeability with 80 md fracture permeability at 30 °C separator temperature.....	57
Figure 4.9 – Measured and calculated heavy components mass fraction of produced oil at separator condition.....	58
Figure 4.10 – Reported and calculated molecular weight of produced oil at separator condition.....	59

Figure 4.11 – Calculated liquid saturation versus CO ₂ liquid mole fraction from constant pressure (300 bara) and temperature (130 °C) swelling test	60
Figure 4.12 – Calculated oil recovery factor based on mole, mass and oil saturation from matched model with linear core relative permeability	61
Figure 4.13 – Calculated mole based oil recovery of light and intermediate components from matched model with linear core relative permeability	62
Figure 4.14 – Calculated mole based oil recovery of heavy components from matched model with linear core relative permeability	62
Figure 4.15 – Mole based oil recovery results from numerical sensitivity models at 30 °C separator temperature	63
Figure 4.16 – CO ₂ mole fraction profile of core after 12 hours for matched model with linear core relative permeability (at about 36% oil recovery)	64
Figure 4.17 – CO ₂ mole fraction profile of core after 5 days for matched model with linear core relative permeability (at about 79% oil recovery)	65
Figure 5.1 – Oil and gas relative permeability used in the matched model	69
Figure 5.2 – Oil and water relative permeability used in the matched model	69
Figure 5.3 – Measured and calculated cumulative volume of CO ₂ injected	71
Figure 5.4 – Model and Valhall (after Webb et. al.) capillary pressure curves ...	73
Figure 5.5 – Profile of CO ₂ injection rate in experiment-1 (S _w =0.0) and experiment-2 (S _w =0.263)	74
Figure 5.6 – Profile of separator temperature in experiment-1 (S _w =0.0) and experiment-2 (S _w =0.263)	75

Figure 5.7 – Measured produced oil mass with matched simulation results for three core water relative permeability and with and without water-oil capillary pressure.....	75
Figure 5.8 – Measured produced water volume with matched simulation results for three core water relative permeability and with and without water-oil capillary pressure.....	76
Figure 5.9 – Measured and calculated heavy components mass fraction of produced oil at separator condition.....	77
Figure 5.10 – Reported and calculated molecular weight of produced oil at separator condition.....	77
Figure 5.11 – Calculated mole based oil recovery factor of two experiments versus HCPV injected from matched model	79
Figure 5.12 – Calculated mole based component recovery of two experiments versus HCPV injected from matched model	79
Figure 5.13 – Calculated mole based component recovery of two experiments versus HCPV injected from matched model	80
Figure 5.14 – Calculated mole based oil recovery factor of two experiments versus time from matched model.....	80
Figure 5.15 – CO ₂ mole fraction profile of core after 5 hours for matched model of experiment-2 (at about 36% oil recovery).....	82
Figure 5.16 – CO ₂ mole fraction profile of core after 2.8 days for matched model of experiment-2 (at about 78.5% oil recovery).....	83
Figure 5.17 – Mole based oil recovery results from grid sensitivity models	84
Figure 5.18 – Mole based oil recovery results from numerical sensitivity models	84
Figure 5.19 – Effect of diffusion coefficient and diffusion drive on mole based oil recovery factor	85

Figure 6.1 – Effect of grid cells on oil recovery vs. time for single matrix block using equilibrium-gas injection at system pressure of 1400 psia ...	94
Figure 6.2 – Slimtube simulation using CO ₂ injection gas. Oil recovery at 1.2 PVs of gas injected vs. pressure for different number of grid cells	95
Figure 6.3 – Comparison of CO ₂ and Haft Kel oil densities as a function of pressure (at reservoir temperature of 110 °F).....	97
Figure 6.4 – Effect of different injection gas on oil recovery vs. time for single matrix block at system pressure of 1400 psia.....	98
Figure 6.5 – Early stage CO ₂ gas displacement, gas saturation profile inside matrix block after 1410 days at system pressure of 1400 psia (at 71% oil recovery)	99
Figure 6.6 – Mid stage CO ₂ gas displacement, gas saturation profile inside matrix block after 3600 days at system pressure of 1400 psia (at 79% oil recovery).....	100
Figure 6.7 – Late stage CO ₂ gas displacement, gas saturation profile inside matrix block after 7100 days at system pressure of 1400 psia (at 84% oil recovery)	101
Figure 6.8 – Late stage CO ₂ gas displacement, interfacial tension profile inside matrix block after 7100 days at system pressure of 1400 psia (at 84% oil recovery)	103
Figure 6.9 – IFT profile for single matrix block using CO ₂ injection gas at system pressure of 2500 psia	104
Figure 6.10 – Oil saturation profile for single matrix block using CO ₂ injection gas at system pressure of 2500 psia.....	105
Figure 6.11 – Effect of CO ₂ dilution on oil recovery vs. time for single matrix block at system pressure of 1400 psia	107

Figure 6.12 – Effect of injection gas, inject different concentration of CO ₂ after equilibrium and Methane injection on oil recovery vs. time for single matrix block at system pressure of 1400 psia	108
Figure 6.13 – Effect of reservoir pressure on oil recovery vs. time for single matrix block system using equilibrium gas (dash line) and CO ₂ (solid line) injection.....	109
Figure 6.14 – Comparison of CO ₂ injection gas with equilibrium gas oil recovery at 10000 days vs. reservoir pressure for Single matrix block system	110
Figure 6.15 – Effect of matrix block height on oil recovery vs. time for single matrix block using equilibrium (dash line) and CO ₂ (solid line) injection gas at system pressure of 1400 psia.....	111
Figure 6.16 – Effect of matrix block permeability on oil recovery vs. time for single matrix block using equilibrium (dash line) and CO ₂ (solid line) injection gas at system pressure of 1400 psia.....	113
Figure 6.17 – Time of reaching certain oil recovery vs. Matrix block permeability for single matrix block using equilibrium and CO ₂ injection gas at system pressure of 1400 psia.....	113
Figure 6.18 – Total oil recovery vs. time for different number of stacked matrix blocks using equilibrium gas injection at system pressure of 1400 psia.....	115
Figure 6.19 – Total oil recovery vs. time for different number of stacked matrix blocks using CO ₂ gas injection at system pressure of 1400 psia .	115
Figure 7.1 – Effect of reservoir pressure on oil recovery vs. time for C ₁ -C ₅ lab system using CO ₂ injection with (solid lines) and without diffusion (dash lines).....	124

Figure 7.2 – CO ₂ gas displacement with diffusion, core oil saturation profile after 1 day for C ₁ -C ₅ lab system at 1000 psia (at about 60% oil recovery)	125
Figure 7.3 – Comparison of reservoir pressure effect on oil recovery vs. time for C ₁ -C ₅ (solid lines) and Haft Kel (dash lines) lab system using CO ₂ injection with diffusion.....	126
Figure 7.4 – CO ₂ gas displacement, oil saturation profile inside core after 16 days for Haft Kel lab system at 1000 psia (at about 17% oil recovery)	127
Figure 7.5 – Effect of reservoir pressure on oil recovery vs. time for 8-ft cube Haft Kel single matrix block system using CO ₂ injection with (solid lines) and without diffusion (dash lines)	128
Figure 7.6 – CO ₂ gas displacement, matrix block oil saturation profile after 300 days for 8-ft cube Haft Kel single matrix block system at 1000 psia (at about 21.5 % oil recovery)	129
Figure 7.7 – Oil saturation profile for 8-ft cube Haft Kel single matrix block using CO ₂ injection gas at 10000 days.....	130
Figure 7.8 – Effect of matrix block permeability on oil recovery vs. time for 8-ft cube Haft Kel single matrix block using CO ₂ injection gas at various system pressure.	131
Figure 7.9 – Effect of matrix block dimension on oil recovery vs. time for Haft Kel single matrix block using CO ₂ injection gas at system pressure of 1000 psia.....	128
Figure 7.10 – Effect of matrix block dimension on oil recovery vs. time for Haft Kel single matrix block using CO ₂ injection gas at system pressure of 1500 psia.....	132
Figure 7.11 – Effect of injection rate on 0.8 md core during CO ₂ gas injection for C ₁ -C ₅ lab system at 1000 psia.....	134

Figure 7.12 – Effect of injection rate on 5 md core during CO ₂ gas injection for C ₁ -C ₅ lab system at 1000 psia.....	135
Figure 7.13 – Effect of injection rate on 0.8 md core during CO ₂ gas injection for Haft Kel lab system at 1000 psia.....	135
Figure 7.14 – Effect of injection rate on 0.8 md single matrix block during CO ₂ gas injection for 8-ft cube Haft Kel system at 1000 psia.....	136
Figure 7.15 – Effect of injection rate on 0.8 md single matrix block during CO ₂ gas injection for 8-ft cube Haft Kel system at 1500 psia.....	137

Nomenclature

B_o	= oil formation volume factor, L^3/L^3 ,
c	= molar concentration, n/L^3
D_i	= diffusion coefficient of component i , L^2/t , cm^2/s
D_i^a	= activity-corrected diffusion coefficient of component i , L^2/t , cm^2/s
D_i^T	= thermal diffusion coefficient of component i , L^2/t , cm^2/s
D_g	= gas diffusion coefficient, L^2/t , cm^2/s
D_o	= oil diffusion coefficient, L^2/t , cm^2/s
F	= formation resistivity
f_i	= fugacity of component i , m/Lt^2
G	= gravity acceleration
h	= height, L
h_0	= reference height, L
J_i	= molar flux of component i per unit area
k_r	= relative permeability
M_i	= component i molecular weight, m/n
M_g	= gas molecular weight, m/n
M_o	= oil molecular weight, m/n
m	= cementation factor in porous media
m_k	= current mass of component i in place, m, kg
m_{ki}	= initial mass of component i in place, m, kg
m_{op}	= produced oil mass at surface condition, m, kg
m_{oi}	= initial oil mass in place at experiment condition, m
N	= number of grid cells
N_x	= number of grid cells in x-direction
N_y	= number of grid cells in y-direction
N_z	= number of grid cells in z-direction
n_k	= current moles of component i in place
n_{ki}	= initial moles of component i in place
p	= pressure, m/Lt^2 , bara
P_C	= capillary pressure, m/Lt^2 , bara or psia
$P_{C,lab}$	= measured capillary pressure, m/Lt^2 , bara or psia
P_{cgo}	= drainage gas-oil capillary pressure, m/Lt^2 , bara or psia
P_{cwoi}	= imbibition water-oil capillary pressure, m/Lt^2 , bara or psia
P_i	= parachor of component i
R	= gas constant
RF	= oil recovery factor
RF_{comp}	= mole based component recovery factor

RF_{mole}	= mole based oil recovery factor
RF_{mass}	= mass based oil recovery factor
RF_{so}	= saturation based oil recovery factor
RF_{surf}	= oil recovery factor based on produced oil mass at surface condition
s	= components volume shift
S_g	= gas saturation
S_{gc}	= critical gas saturation
S_o	= oil saturation
S_{oi}	= initial oil saturation
S_{org}	= residual oil saturation to gas
S_{orw}	= residual oil saturation to water
S_{wc}	= connate water saturation
T	= temperature, T
T_{ci}	= critical temperature of component i , T
V_{oi}	= initial oil volume in place, L ³ , m ³
v_{ci}	= critical molar volume of component i , L ³ /n
x_i	= oil mole fraction of component i
y_i	= gas mole fraction of component i
Z_i	= critical compressibility factor
ϵ/κ	= Lennard-Jones 12-6 potential parameter
μ_i	= chemical potential of component i
μ_{i0}	= reference chemical potential of component i
ρ_g	= gas density, m/L ³ , kg/m ³
ρ_M	= molar density, n/L ³
ρ_{Mpc}	= pseudo-critical molar density, n/L ³
ρ_{pr}	= pseudo-reduced molar density
ρ_o	= oil density, m/L ³ , kg/m ³
σ	= characteristic length
σ_{go}	= gas-oil interfacial tension, m/t ² , mN/m
σ_{lab}	= reference gas-oil interfacial tension, m/t ² , mN/m
τ	= tortuosity
ϕ	= porosity
Ω_{ij}	= low-pressure diffusion coefficient correlation parameter

SI Metric Conversion Factors

bbbl x 1.589 873	E - 01 = m ³
D x 9.869 23	E - 13 = m ²
dyne/cm x 1.000 000	E + 00 = mN/m
ft x 3.048*	E - 01 = m
ft ³ x 2.831 685	E - 01 = m ³
°F (oF+459.67)/1.8	E - 01 = K
in x 2.54*	E - 02 = m
in ² x 6. 4516*	E - 04 = m

lbm/ft ³ x 2.831 685	E - 02 = m
psi x 6.894 757	E + 03 = Pa
°R °R/1.8	E - 01 = K

*Conversion factor is exact.

Chapter 1

Introduction

1.1 Background

CO₂ injection has recently been shown to provide significant enhanced oil recovery from naturally fractured reservoirs¹. Li *et al.* (2000) performed CO₂ injection at 1750 psig on artificially-fractured cores after water flooding in a dead-oil system. Gravity drainage was suggested to be the dominant recovery mechanism in these tests, with significant tertiary oil recovery after water flooding. The authors observed that the recovery of initial oil at the start of the CO₂ injection declined as the rock permeability decreased and the initial water saturation increased. Darvish *et al.* (2006) performed CO₂ injection experiments on an outcrop chalk core that was surrounded by an artificial fracture, at reservoir conditions where the core was initially saturated with live oil. These authors reported that gas produced at an early stage was enriched with methane. During later stages, the amount of intermediate components increased in the production stream, and that heavier components were recovered toward the end of the experiment. This result was also reported by Moortgat, Firoozabadi and Farshi (2010) in a paper that presented simulation studies of the Darvish *et al.* (2006) experiments.

Trivedi and Babadagli (2008) investigated the injection flow rate effect on first contact miscible displacement in a matrix/fracture system that used heptane

¹ Holm and Josendal (1974), among many others, have studied CO₂ injections in unfractured rock.

(C₇) as the injectant displacing kerosene or mineral oil at atmospheric conditions. These authors reported that higher solvent injection rates yielded higher rates of oil production during the early stages of the experiment, whereas lower injection rates resulted in greater ultimate oil recovery.

Er, Babadagli and Zhenghe (2010) investigated micro-scale matrix/fracture interactions during CO₂ injection in a synthetic fractured system. The authors used a glass bead model with normal decane (n-C₁₀) as the oil and CO₂ as the injectant. They concluded that for immiscible CO₂ displacement, the amount of oil trapped in the matrix was reduced with increasing injection rates. They also observed that for miscible CO₂ conditions, oil was recovered faster with increasing injection rate.

Morel *et al.* (1993) and Le Romancer *et al.* (1994a) studied the effects of diffusion on a C₁-C₅ oil mixture by injecting methane (C₁), nitrogen (N₂) and CO₂ into an outcrop core. Hua, Whitson and Yuanchang (1991) simulated Morel's experiments with a model that combined an analytical calculation for the fracture and a numerical model for the core. These authors showed that the correction of the capillary pressure curve for the changes in interfacial tension was due to diffusion-driven compositional variation. Recently, Jamili, Willhite and Green (2010) simulated both of these previous experiments using a (self-built, non-commercial) numerical model. These authors reported that diffusion was the main mass transfer mechanism between the matrix and fracture during nitrogen (N₂) injection. In other CO₂ experiments conducted by Le Romancer, diffusion and convection were both shown to be important.

Asghari and Torabi (2008) performed CO₂ gravity drainage experiments with a synthetic dead oil (n-C₁₀), above and below the CO₂ MMP. These authors were not able to match their laboratory experiments using a simulation model.

Hoteit and Firoozabadi (2009) studied diffusion in fractured media for gas injection and recycling schemes, using a (self-built, non-commercial) numerical model. They reported that diffusion improved the amount of oil recovery and

delayed gas breakthrough. In their modeling study, these authors did not consider matrix gas-oil capillary pressure.

Le Romancer, Defives and Fernandes (1994b) performed 1-D experiments on a chalk core that was saturated with a methane-pentane (C_1 - C_5) mixture in the presence of different levels of water saturation, using two different injection gases (N_2 and C_1). They concluded that the effect of water saturation on recovery strongly depended on the nature of the diffusing gas. In their methane injection experiments, the oil was produced into a fracture faster for higher water saturations. In their nitrogen (N_2) injection experiments, the methane rate of production was proportional to the hydrocarbon mass initially present, whereas the rate of pentane production remained unchanged.

1.2 Thesis Outline

The present thesis contains two main sections: a) a modeling study of experimental tests performed at NTNU by H. Karimaie (Chapter 3) and G.R. Darvish (Chapters 4 and 5); and b) a detailed study of CO_2 injection recovery mechanisms in field-scale matrix/fracture systems (Chapters 6 and 7).

The mechanism of small-scale, laboratory CO_2 injection was investigated by modeling lab experiments, assessing the ability of commercial numerical simulators to model physical phenomena contributing to oil recovery by CO_2 injection.

Once it was established that physics-based numerical models could model accurately the laboratory tests, without unphysical parameters or empirical pseudo-physics (e.g. relative permeability model adjustments), these models were extended to field-scale matrix/fracture systems to quantify recovery performance affected by capillary-gravity effects, non-equilibrium thermodynamics and diffusion-controlled mass transfer – and which mechanisms controlled recovery under different assumptions of matrix-fracture geometry and injection rate.

Nomenclature is provided at the beginning of the thesis. Conclusions, recommendations for further work and references are provided at the end of each chapter. Consequently, chapters can be read separately, and more-or-less independently. Samples of input data sets are given in Appendix A.

1.3 References

- Asghari, K and Torabi, F. 2008. Effect of Miscible and Immiscible CO₂ Flooding on Gravity Drainage: Experiment and Simulation Results., Paper SPE 110587 presented at the 2008 SPE/DOE Improved Oil Recovery Symposium, Tulsa, Oklahoma, U.S.A., 19-23 April.
- Chang, Y., and Coats B.K and Nolen, J.S. 1998. A Compositional Model for CO₂ Floods Including CO₂ Solubility in Water. SPE Reservoir Evaluation and Engineering, **1**(2): 155-160. SPE-35164-PA.
- Darvish, G.R., Lindeberg, E., Holt, T., Utne, S.A. and Kleppe, J. 2006. Reservoir Conditions Laboratory Experiments of CO₂ Injection into Fractured Cores. Paper SPE 99650 presented at the 2006 SPE Europec/EAEG Annual Technical Conference and Exhibition, Vienna, Austria, 12-15 June.
- Er, V., Babadagli, T and Zhenghe X. 2010. Pore-Scale Investigation of the Matrix-Fracture Interaction during CO₂ Injection in Naturally Fractured Oil Reservoir. Energy Fuels 2010, **24**: 1421-1430.
- Holm, L.W. and Josendal, V.A. 1974. Mechanism of Oil Displacement by Carbon Dioxide. Journal of Petroleum Technology **26**(12): 1427-1438.
- Hoteit, H. and Firoozabadi, A. 2006. Numerical Modeling of Diffusion in Fractured Media for Gas Injection and Recycling Schemes. Paper SPE 103292 presented at the 2006 SPE Annual Technical Conference and Exhibition, San Antonio, Texas, U.S.A., 24-27 September.
- Hua, H. Whitson, C.H., and Yuanchang, Q. 1991. A Study of Recovery Mechanisms in a Nitrogen Diffusion Experiment. Presented at the 9th European IOR Symposium, Stavanger, Norway, May.

-
- Jamili, A. and Willhite, G.P and Green, D.W. 2006. Modeling Gas-Phase Mass Transfer Between Fracture and Matrix in Naturally Fractured Reservoirs. Paper SPE 132622 presented at the SPE Western Regional Meeting, Anaheim, California, U.S.A., May.
- Le Romancer, J.F., Defives, D., Kalaydjian, F. and Fernandes, G. 1994a. Influence of the Diffusion Gas on the Mechanism of Oil Recovery by Gas Diffusion in Fractured Reservoir. Presented at the IEA Collaborative Project on Enhanced Oil Recovery Workshop and Symposium, Bergen, Norway, August.
- Le Romancer, J.F., Defives, D. and Fernandes, G. 1994b. Mechanism of Oil Recovery by Gas Diffusion in Fractured reservoir in Presence of Water. Presented at the SPE/DOE Ninth Symposium on Improved Oil Recovery, Tulsa, USA, April.
- Li, H., Putra, E., Schechter, D.S. and Grigg, R.B. 2000. Experimental Investigation of CO₂ Gravity Drainage in a Fractured System. Paper SPE 64510 presented at the SPE Asia Pacific Oil and Gas Conference and Exhibition, Brisbane, Australia, 16-18October.
- Moortgat, J., Firoozabadi, A. and Farshi M.M., 2009. A New Approach to Compositional Modeling of CO₂ Injection in fractured Media Compared to Experimental Data. Paper SPE 124918 presented at the 2009 SPE Annual Technical Conference and Exhibition, New Orleans, Louisiana, U.S.A., 4-7 October.
- Morel, D.D., Bourbiaux B., Latil, M., and Thiebot B. 1990. Diffusion Effect in Gas Flooded Light Oil Fractured Reservoir. Paper SPE 20516 presented at the 65th SPE Annual Technical Conference and Exhibition, New Orleans, Louisiana, U.S.A., September.
- Trivedi, J. and Babadagli, T. 2008. Efficiency of Diffusion Controlled Miscible Displacement in Fractured Porous Media. *Transport in Porous Media*, **71**(3): 379-394.

Chapter 2

Fundamentals and Calculations

2.1 Introduction

This chapter presents some fundamental concepts and calculations used in the research – e.g., diffusion coefficient estimation and relative permeability modeling.

2.2 Diffusion

Diffusion plays an important role in some of the experiments that are modeled in the next sections. Fick presented the equation for molecular diffusion in 1885 and stated that the flux of a substance diffusing through a unit area of cross section is proportional to the concentration gradient that is measured perpendicular to the cross section:

$$J_i = -cD_i \frac{\partial x_i}{\partial d} \dots\dots\dots(2.1)$$

However, diffusion in a hydrocarbon fluid is also affected by factors other than the concentration gradient. Therefore, it is more appropriate to use a diffusion flux that is driven by the total potential given by chemical, gravity, and thermal forces (Bird, Stewart and Lightfoot 1960):

$$J_i = -cD_i^a x_i \frac{1}{RT} \frac{\partial}{\partial d} [\mu_i - M_i G(h - h_0) + M_i D_i^T \ln(T)] \dots\dots\dots (2.2)$$

$$\text{where } \mu_i = \mu_{i0} + RT \ln(f_i) \dots\dots\dots (2.3)$$

If gravity and the thermal diffusion term in Eq. (2.2) are omitted, Eq. (2.2) can be written as:

$$J_i = -cD_i^a x_i \frac{\partial}{\partial d} (\ln f_i)_{T,P} \dots\dots\dots (2.4)$$

Using the chain rule, Eq. (2.4) can be rewritten as:

$$J_i = -cD_i^a \frac{\partial (\ln f_i)}{\partial \ln(x_i)} \frac{\partial x_i}{\partial d} \dots\dots\dots (2.5)$$

Comparing Eq. (2.1) and Eq. (2.5), the activity-corrected diffusion coefficient D_i^a (Reid, Prausnitz and Poling 1987) is given by:

$$D_i^a = \frac{D_i}{\partial \ln(f_i) / \partial \ln(x_i)} \dots\dots\dots (2.6)$$

2.2.1 Diffusion Coefficient

Several diffusion correlation coefficients are given in the literature (Poling, Prausnitz and O'Connell. 2004 and Riazi 2005). We used the following equations to calculate the oil and gas diffusion coefficients. Sigmund (1976a) proposed correlations for high pressure and temperature that are widely used in petroleum engineering:

$$\frac{\rho_M D_{ij}}{\rho_M^o D_{ij}^o} = 0.99589 + 0.096016 \rho_{pr} + 0.22035 \rho_{pr}^2 + 0.032874 \rho_{pr}^3 \dots\dots\dots (2.7)$$

To avoid a negative D_{ij} for $\rho_{pr} > 3.7$ and to allow for a better prediction of the measured liquid diffusion coefficients, da Silva and Belery (1989) recommended the following extrapolation for $\rho_{pr} > 3.0$:

$$\frac{\rho_M D_{ij}}{\rho_M^o D_{ij}^o} = 0.18839 \exp(1 - \rho_{pr}) \dots\dots\dots (2.8)$$

where pseudo-reduced molar density (ρ_{pr}) is calculated from:

$$\rho_{pr} = \frac{\rho_M}{\rho_{Mpc}} \quad \dots\dots\dots (2.9)$$

and pseudo-critical molar density (Reid, Prausnitz and Poling 1987) is obtained from:

$$\rho_{Mpc} = \frac{\sum_{i=1}^n z_i v_{ci}^{2/3}}{\sum_{i=1}^n z_i v_{ci}^{5/3}} \quad \dots\dots\dots (2.10)$$

The low-pressure binary diffusion coefficient (D_{ij}^o) can be calculated using Chapman-Enskog theory (Hirschfelder, Curtiss and Bird 1954; Bird, Stewart and Lightfoot 1960; Neufield, Janzen and Aziz 1972; Reid, Prausnitz and Poling 1987):

$$D_{ij}^o = 0.001883 \frac{T^{3/2} [(1/M_i) + (1/M_j)]^{0.5}}{p^o \sigma_{ij}^2 \Omega_{ij}} \quad \dots\dots\dots (2.11a)$$

where

$$\Omega_{ij} = \frac{1.06036}{T_{ij}^{0.1561}} + \frac{0.193}{\exp(0.47635T_{ij})} + \frac{1.03587}{\exp(1.52996T_{ij})} + \frac{1.76474}{\exp(3.89411T_{ij})} \quad \dots\dots\dots (2.11b)$$

$$T_{ij} = \frac{T}{(\varepsilon/k)_{ij}} \quad \dots\dots\dots (2.11c)$$

$$(\varepsilon/k)_{ij} = [(\varepsilon/k)_i (\varepsilon/k)_j]^{1/2} \quad \dots\dots\dots (2.11d)$$

$$(\varepsilon/k)_i = 65.3 T_{ci} Z_{ci}^{18/5} \quad \dots\dots\dots (2.11e)$$

$$\sigma_{ij} = 0.5(\sigma_i + \sigma_j) \quad \dots\dots\dots (2.11f)$$

$$\text{and } \sigma_i = 0.1866 \frac{v_{ci}^{1/3}}{Z_{ci}^{6/5}} \quad \dots\dots\dots (2.11g)$$

with the diffusion coefficient, D_{ij}^o , in cm^2/s ; molecular weight, M , in gr/gmol ; temperature, T , in K ; pressure, p , in bar ; characteristic length, σ , in \AA ; Lennard-Jones 12-6 potential parameter, ε/k , in K ; critical volume v_c in cm^3/gmol and critical compressibility factor Z_c .

We used the idea-gas law, $\rho_M^o = p^o/RT$, to determine the low-pressure density-diffusivity product (Bird, Stewart and Lightfoot 1960; Sigmund 1976a; Whitson and Brule 2000):

$$\rho_M^o D_{ij}^o = (2.2648 \times 10^{-5}) \frac{T^{1/2} [(1/M_i) + (1/M_j)]^{0.5}}{\sigma_{ij}^2 \Omega_{ij}} \dots\dots\dots (2.11a)$$

2.2.2 The Diffusion Coefficient in a Multicomponent System

The diffusion coefficient for each component in a multicomponent system is calculated using Wilke's equation (Wilke 1950):

$$D_{im} = \frac{1 - z_i}{\sum_{\substack{j=1 \\ j \neq i}}^N (z_j / D_{ij})} \dots\dots\dots (2.12)$$

Eq. (2.12) is based on the Stefan-Maxwell diffusion equations and is simply a weighted harmonic mean. Sigmund (1976b) reported that Eq. (2.12), which was developed for gas mixtures, may be used also for liquid mixtures.

2.2.3 Diffusion Coefficient in Porous Media

The diffusion path of the components in a porous media deviates from a straight line because of the presence of solid particles. Consequently, the diffusion coefficient of a component must be corrected for the tortuosity, τ . The following equation has been suggested in the literature (Petersen 1958, van Brakel and Heertjes 1974, Ullman and Aller 1982) for correcting the diffusion coefficient for tortuosity in porous media:

$$D_{i,eff} = \frac{D_i}{\tau^2} \dots\dots\dots (2.13)$$

where $D_{i,eff}$ is the effective diffusion coefficient in a porous media, and D_i is the diffusion coefficient in the absence of a porous media.

Shen and Chen (2007) reviewed the impact of tortuosity on the diffusion coefficient. Empirically, tortuosity is related to the porosity (ϕ) and the formation resistivity (F) as follows:

$$\tau^2 = (F\phi)^n \dots\dots\dots (2.14)$$

Substituting Archie's law, $F=a/\phi^m$ (Archie 1942), into Eq.(2.14) gives tortuosity in terms of porosity (Lerman 1979, Ullman and Aller 1982 and Nelson and Simmons 1995):

$$\tau^2 = (a\phi^{1-m})^n \dots\dots\dots (2.15)$$

Substituting Eq. (2.15) with $n=a=1$ into Eq. (2.13) gives:

$$D_{i,eff} = D_i\phi^{m-1} \dots\dots\dots (2.16)$$

where m is the cementation factor in the porous media. In the present study, m is equal to 2.

In this work, any pressure and composition dependency of the diffusion coefficients are not considered.

2.3 Relative Permeability and Capillary Pressure Curve

In the next chapters, we use the following equations to calculate the relative permeability and capillary pressure in all numerical simulation (SENSOR Manual 2009):

$$k_{rw} = k_{rwr0} [(S_w - S_{wc}) / (1 - S_{orw} - S_{wc})]^{n_w} \dots\dots\dots (2.17)$$

$$k_{row} = k_{rocw} [(1 - S_{orw} - S_w) / (1 - S_{orw} - S_{wc})]^{n_{ow}} \dots\dots\dots (2.18)$$

$$k_{rog} = k_{rocw} [(1 - S_{org} - S_{wc} - S_g) / (1 - S_{org} - S_{wc})]^{n_{og}} \dots\dots\dots (2.19)$$

$$k_{rg} = k_{rgro} [(S_g - S_{gc}) / (1 - S_{org} - S_{wc} - S_{gc})]^{n_g} \dots\dots\dots (2.20)$$

$$P_{cwoi} = b_1 + b_2 [1 - (S_w - S_{wc}) / (1 - S_{wc})]^{b_3} - b_4 [(S_w - S_{wc}) / (1 - S_{wc})]^{b_5} \dots\dots\dots (2.21)$$

$$P_{cgo} = c_1 + c_2 [(S_g) / (1 - S_{wc})]^{c_3} \dots\dots\dots (2.22)$$

where S_{wc} is the connate water saturation; S_{orw} is the residual oil saturation to water; S_{org} is the residual oil saturation to gas; S_{gc} is the critical gas saturation; k_{rwr0} is the relative permeability of water at $S_w=1-S_{orw}$ and $S_g=0$; k_{rgro} is the relative permeability of gas at $S_w=S_{wc}$ and $S_g=S_{org}$; k_{rocw} is the relative permeability of oil at $S_w=S_{wc}$ and $S_g=0$; n_w , n_{ow} , n_g and n_{og} are the exponents of the relative permeability; P_{cwoi} is the imbibition water-oil capillary pressure; and P_{cgo} is the gas-oil capillary pressure.

2.3.1 Three Phase Relative Permeability

Because mobile oil, gas and water exist in the modeling, three-phase oil relative permeabilities are needed. Extended Stone's first method (Stone 1970 and Fayers 1973), in which the minimum or residual oil saturation is treated as a function of S_g , was used:

$$S_{om} = S_{org}S_{gn} + S_{orw}(1 - S_{gn}) \quad \dots\dots\dots (2.23a)$$

$$S_{gn} = \frac{S_g}{1 - S_{wc} - S_{org}} \quad \dots\dots\dots (2.23b)$$

where S_{om} is the minimum oil saturation, S_{org} is the residual oil saturation to gas, S_{orw} is the residual oil saturation to water and S_{wc} is the connate water saturation.

2.3.2 Capillary Pressure Scaling with IFT

The capillary pressure is scaled with the interfacial tension (IFT) according to:

$$P_{cgo} = \left(\frac{\sigma}{\sigma_{ref}}\right)P_{cgo,lab} \quad \dots\dots\dots (2.24)$$

where $P_{cgo,lab}$ is the original capillary pressure input in the model, σ_{ref} is the reference IFT and σ is the IFT calculated using an equation developed by Weinaug and Katz (1943):

$$\sigma_{go} = \left[\sum P_i \left(x_i \frac{\rho_o}{M_o} - y_i \frac{\rho_g}{M_g} \right) \right]^4 \quad \dots\dots\dots (2.25)$$

2.4 Minimum Miscibility Conditions

The minimum conditions at which the resulting mixture of two fluids mixed together at any proportion is homogeneous in compositions and is identical in intensive properties.

Because the reservoir temperature is usually assumed to be constant in reservoir engineering, the minimum miscibility conditions refer to either the minimum miscibility pressure (MMP), when the compositions of the two fluids are fixed, or the minimum miscibility enrichment (MME), when the oil composition and the reservoir pressure are specified. No fluid interface between

the two fluids exists when these fluids are fully miscible and their IFT becomes zero. In the absence of any dispersion, if the reservoir oil is fully miscible with an injection gas at the minimum miscibility conditions, the residual oil saturation behind the injection gas front is essentially zero, and the microscopic oil recovery is expected ~100%.

The process of achieving miscibility at the minimum miscibility conditions can vary depending on the compositions of the displacing and displaced fluids and on the reservoir temperature. Fluids may become miscible upon first contact, which is called first-contact miscibility. Most fluids are not first-contact miscible but can achieve miscibility during continuous contact by interphase mass transfer. These fluids are termed multi-contact miscible, much more common in hydrocarbon reservoirs. Several multi-contact miscible mechanisms have been proposed and summarized in the literature (Stalkup 1983; Zick 1986; Whitson and Brule 2000) based on the compositions of the two fluids, the pressure and temperature: vaporizing gas drive (VGD), condensing gas drive (CGD) and condensing/vaporizing gas drive (C/V).

2.4.1 MMP calculation

Several methods for determining the MMP are available in the literature, such as the slimtube experiment (Orr *et al.* 1982), the single-cell, forward- and backward-contact algorithms (Stalkup 1982), the multi-cell algorithm (Cook *et al.* 1969a and 1969b), the slimtube-type compositional numerical simulations (Zick 1986), a proprietary multi-cell algorithm (Zick 1986), and analytical methods that are based on the method of characteristics (Johns and Orr 1996 and Wang and Orr 1998). A rising bubble apparatus (Novosad and Costain 1988) has also been suggested as an alternative to the slimtube experiment

If it is designed, conducted, and interpreted properly, the slimtube experiment is considered to define a “true thermodynamic” MMP. This method is usually expensive and time-consuming. Alternatively, 1D slimtube-type simulations can be used to evaluate the MMP_{1D} . For any method a properly tuned equation of state (EOS) model is required, capable of modeling the important phase behavior,

such as forward and/or backward-contact experiments, swelling tests and MMP experiments. In the present study, the MMP values were calculated by a the *PhazeComp* PVT program or by a 1D numerical simulation that requires elimination of numerical dispersion (Høier 1997).

2.5 Numerical Gridding

One needs to continue refining the grid size in each dimension until the performance no longer changes and has appeared a “converged” solution. The first sensitivity that should be performed in a numerical study is the grid-sensitivity analysis. However, this analysis may not be possible when the laboratory experiments are simulated because the numerical effect should be eliminated or reduced to a minimum in the model results. Therefore, the simulation should start with the fine grid model, and then the grid sensitivity should be assessed at the end of simulation to determine how this sensitivity can affect the model results. We present the investigation of the numerical grid effect in Chapters 5 and 6.

2.6 References

- Bird, R.B., Stewart, W.E. and Lightfoot, E.N., 1960. Transport Phenomena. John Wiley & Sons Inc, New York.
- Coats Engineering, 2009. SENSOR Manual, www.coatsengineering.com, October.
- Cook, A. B., Johnson, F. S., Spencer, G. B., Bayazeed, A.F. and Walker, C. J., 1969a. Effects of Pressure, Temperature, and Type of Oil on Vaporization of Oil During Gas Cycling, RI 7278, USBM(1969).
- Cook, A. B., Johnson, F. S., Spencer, G. B., Bayazeed, A.F. and Walker, C. J., 1969b. Realistic K Values of C₇₊ Hydrocarbons for Calculating Oil Vaporization During Gas Cycling at High Pressures. JPT **21**(7):901-915.
- da Silva, F.V and Belery, P., 1989. Molecular Diffusion in Naturally Featured Reservoirs: a Decisive Recovery Mechanism., Paper SPE 19672 presented at

- the 64th SPE Annual Technical Conference and Exhibition, San Antonio, Texas, U.S.A., 8-11 October.
- Fayers F.J. 1973. Extension of Three-Phase Relative Permeability and Residual Oil Data. *Journal of Canadian Petroleum Technology*, **251**:419-425
- Hirschfelder, J.O., Curtiss C.F. and Bird R.B., 1954. *Molecular Theory of Gas and Liquids*, Wiley, New York.
- Høier, L. 1997. *Miscibility Variation in Compositionally Grading Petroleum Reservoir*. PhD Dissertation, NTNU, Trondheim, Norway.
- Johns, R.T. and Orr, F.M., Jr., 1996. Miscible Gas Displacements of Multicomponent Oils. *SPEJ* **1**(1):39-50.
- Lerman, A., 1979. *Geochemical Processes: Water and Sediment Environments*. Wiley, New York.
- Neufeld, P.D., Janzen, A.R. and Aziz R.A., 1972. Empirical Equations to Calculate 16 of the Transport Collision Integrals $\Omega(l, s)^*$ for the Lennard-Jones (12-6) Potential. *Journal of Chemical Physics*, **57**(3), DOI: 10.1063/1.1678363.
- Nelson, J.S., Simmons, E.C., 1995. Diffusion of Methane and Ethane through The Reservoir Cap Rock: Implications for The Timing and Duration of Catagenesis. *AAPG Bulletin* **79**, 1064-1074.
- Novosad, Z. and Costain, T.G., 1988. New Interpretation of Recovery Mechanisms in Enriched Gas Drives. *Journal of Canadian Petroleum Technology*. March-April, **21**(2): 54-60.
- Orr, F.M.J., Silva, M.K., Lien, C.L. and Pelletier, M.T., 1982. Laboratory Experiments to Evaluate Field Prospects for CO₂ Flooding. *JPT* **34**(4):888-898.
- Petersen, E.E., 1958. Diffusion in a pore of varying cross section. *American Institute of Chemical Engineers Journal* **4**:343-345.
- Poling, B.E., Prausnitz, J.M. and O'Connell, J.P., 2004. *The Properties of Gases and Liquids*. Fifth Edition, McGraw-Hill, New York.

-
- Reid, R.C., Prausnitz, J.M. and Poling, B.E., 1987. *The Properties of Gases and Liquids*. Fourth Edition, McGraw-Hill, New York.
- Riazi, M.R. 2005. *Characterization and Properties of Petroleum Fractions*. First Edition, ASTM, Philadelphia.
- Sigmund, P.M., 1976a. Prediction of Molecular Diffusion at Reservoir Condition. Part I - Measurement and Prediction of Binary Dense Gas Diffusion Coefficients. *Journal of Canadian Petroleum Technology*, Apr-Jun, **15**(2). DOI: 10.2118/76-02-05
- Sigmund, P.M., 1976b. Prediction of Molecular Diffusion At Reservoir Conditions. Part II - Estimating the Effects Of Molecular Diffusion And Convective Mixing In Multicomponent Systems. *Journal of Canadian Petroleum Technology*, Jul-Sept, **15**(3). DOI: 10.2118/76-03-07.
- Stalkup, F.I. Jr. 1982: Status of Miscible Displacement. paper SPE 9992 presented at the 1982 SPE International Petroleum Exhibition and Symposium, Beijing, China.
- Stalkup, F.I. Jr. 1983. *Miscible Displacement*. Henry L. Doherty Monograph Series, SPE, Richardson, Texas, USA, 8.
- Stone, H.L., 1970. Probability Model for Estimating Three-Phase Relative Permeability. *J. Pet. Tech.* 249:214-218, *Trans. AIME* 249.
- Ullman, W.J., Aller, R.C., 1982. Diffusion Coefficients in Near Shore Marine Sediments. *Limnology Oceanography* **27**: 552–556.
- van Brakel, J., Heertjes, P.M., 1974. Analysis of Diffusion in Macroporous Media in Terms of a Porosity, a Tortuosity and a Constrictivity Factor. *International Journal of Heat and Mass Transfer* **17**: 1093–1103.
- Wang, Y. and Orr, F.M., Jr., 1998. Calculation of Minimum Miscibility Pressure. paper SPE 39683 presented at the 1998 SPE/DOE Improved Oil Recovery Symposium, Tulsa, April 19-22.
- Weinaug C.F. and Katz D.L. 1943. Surface Tension of Methane-Propane Mixtures. *Ind. & Eng. Chem.* **35**(2): 239–246.

-
- Whitson, C.H. and Brule M.R., 2000. Phase Behavior. Monograph Vol. **20**, Richardson, TX.
- Wilke, C.R., 1950. Diffusion Properties of Multicomponent Gases. Chemical Engineering Progress, **46**(2): 95-104.
- Zick, A.A., 1986: "A Combined Condensing/Vaporizing Mechanism in the Displacement of Oil by Enriched Gases," paper SPE 15493 presented at the 1986 SPE Annual Technical Conference and Exhibition, New Orleans, Oct. 5-8.
- Zick Technologies: MMPz Manual, www.zicktech.com.
- Zick Technologies: *PhazeComp*, www.zicktech.com.

Chapter 3

Modeling CO₂ Injection in Karimaie Fractured Chalk Experiment

3.1 Introduction

Karimaie (2007) performed equilibrium gas injection followed by CO₂ injection in a series of experiments on chalk and carbonate cores at reservoir conditions, where the cores were initially saturated with live synthetic oil. This chapter presents a numerical modeling study of CO₂ injection in a chalk core based on experimental data, as reported by Karimaie (2007). The experiment consisted of a vertically-oriented 19.6 cm long chalk outcrop core initially saturated with reservoir synthetic oil consisting of C₁ and n-C₇ at a temperature of 85 °C and pressure of 220 bar. After saturating the core with the oil mixture by displacement, a small “fracture” volume surrounding the core was created by heating the solid Wood’s metal that originally filled the volume between the core and core holder.

Gas injection was conducted initially using an equilibrium C₁-n-C₇ gas at 220 bar. This gas should have had no recovery by thermodynamic mass transfer, only from immiscible Darcy-controlled displacement driven by pressure gradients and gravity-capillary forces. Once oil production ceased in this first displacement, a second period with pure CO₂ gas injection followed.

Our numerical modeling was conducted with a compositional reservoir simulator. The 2-dimensional r-z model used fine grids for the core matrix and the surrounding fracture.

In a fractured system, matrix permeability controls the rate of recovery. The pressure gradients along fractures are negligible for high permeability fractures where most injected gas flows through the fracture space and the main production mechanism from the matrix is gravity drainage. That means the ratio between the matrix and fracture permeability determines whether viscous displacement (Darcy flow by pressure gradients) governs the displacement, or not. Therefore, fracture permeability should be sufficiently high in an experiment to eliminate viscous displacement in the core. Uncertainty analysis and sources of experimental error had to be studied to understand and simulate the Karimaie experiment.

3.2 Rock and Fluid Properties

Chalk core from Faxø area outcrop in Denmark was used in the Karimaie experiment, with similar rock properties to North Sea chalk. The core had a cylindrical shape with a length of 19.6 cm and 3.8 cm in diameter. Core porosity and permeability were reported as 44% and 5 md, respectively (Karimaie 2007; Karimaie and Torsæter 2009).

Relative permeabilities were not reported by Karimaie (2007) and Karimaie and Torsæter (2009). The capillary pressure curve presented (Karimaie 2007) was water-oil drainage capillary pressure of Ekofisk chalk core measured by Talukdar (2002). In our modeling study, we used instead a C₁-n-C₅ capillary pressure data set from Faxø outcrop chalk core measured by Christoffersen (1992). The water-oil capillary pressure curve was measured with a centrifuge, while the C₁-n-C₅ capillary curve was measured by a high-pressure, porous-plate method. Porosity and permeability of the core used to interpret the water-oil P_{cow} curve was 31% (anomalously low for outcrop chalk) and 1.94 md, respectively. Porosity and permeability of the core used to obtain C₁-n-C₅ P_{cgo} curve were 46.5% and 5 md, respectively. Reference IFT of the water-oil system was not reported, whereas

C₁-n-C₅ was reported and equal to 1.5 mN/m. Reference IFT was used to scale capillary pressure. We found it more appropriate to use the C₁-n-C₅ capillary pressure.

Reported compositions were not measured. 33% of C₁ with 67% of n-C₇ mass fraction were mixed and then flashed at P=220 bar and T= 85 °C. The liquid phase was used as live oil for the experiment and gas injected as equilibrium gas. Karimaie simulated the above process in a PVT simulator to calculate reported EOS oil and gas compositions. Using his reported equation of state (EOS) we were not able to reproduce his reported oil and gas compositions (**Table 3.1**).

Table 3.1 – Comparison of Reported Oil and Gas Compositions by Karimaie (2007) and Recalculated Compositions Using His Reported EOS.

Component	Calculated compositions from reported EOS		Reported compositions	
	x _i	y _i	x _i	y _i
C ₁	0.6885	0.9197	0.7034	0.8825
nC ₇	0.3115	0.0803	0.2966	0.1175

Given this finding, the reported oil and gas compositions and EOS were not used in our study. Bubble point pressure, oil density and interfacial tension (IFT) were measured by the SINTEF PVT lab. *PhazeComp* PVT software using the SRK EOS was used to determine the laboratory oil composition with a 220 bar saturation pressure at 85 °C. The resulting oil composition consisted of 68.44 and 31.56 mole percent of C₁ and n-C₇, respectively. Deviation of calculated oil density (0.413 g/cm³) at 220 bar was about 1.6 % which is in the range of laboratory measurement error. The EOS together with parachor method was tuned to match measured IFT at 220 bar (0.15 mN/m). EOS parameters used in this study are given in **Tables 3.2** and **3.3**.

Table 3.2 – EOS Properties for The SRK Characterization

Component	MW	Tc, K	Pc, bara	Zc	Vshift	ω	Parachor
CO ₂	44.01	304.12	73.74	0.2743	0.2175	0.225	80.00
C ₁	16.04	190.56	45.99	0.2862	-0.0025	0.011	64.23
n-C ₇	100.20	540.20	27.40	0.2611	0.1435	0.350	281.33

Table 3.3 – SRK Binary Interaction Parameters

	CO ₂	C ₁	n-C ₇
CO ₂	0.00000	0.12000	0.15000
C ₁	0.12000	0.00000	0.01574
n-C ₇	0.15000	0.01574	0.00000

3.3 Experimental Procedure

This section describes an experiment originally designed to study gravity drainage in a fracture-matrix system by injecting equilibrium gas followed by CO₂. The experimental procedure is described by Karimaie (2007), Karimaie and Torsæter (2009) and personal communication with Karimaie. Uncertainties and possible sources of lab error are discussed in the next section.

A dried cylindrical chalk core was placed in a steel core holder. The core holder inner length and diameter were 20 cm and 4.2 cm respectively. The core diameter was 3.8 cm and had 19.6 cm length. The fracture was represented by a 2 mm space between core and core holder. Core porosity was reported as 44%, and absolute permeability measured with n-heptane (n-C₇) at room temperature was ~ 5 md (Karimaie 2007; Karimaie and Torsæter 2009).

Due to large permeability contrast between the core and the surrounding space (artificial fracture), it was complicated to saturate the core with live oil. Oil would flow through the high permeable space leaving the core only partially saturated with live oil. Therefore, the space between the core and the core holder wall was initially filled with Wood's metal. The metal melting point is 70 °C; the experiment was conducted at 85 °C. Prior to saturating the core, the Wood's metal was melted and poured into the space between the core and core holder. The fracture was sealed with the metal and had zero permeability after cooling the system.

The core was evacuated and saturated with dead n-C₇. The dead n-C₇ oil was injected at several injection rates to determine absolute permeability. The system was then pressurized and live oil was injected into the core at a rate of 0.1 cm³/min. During injection, the pressure was kept above 220 bar (saturation pressure) and three pore volumes of live oil were injected. Then the system was heated to 85 °C at a constant pressure and Wood's metal was removed from the annular space by injecting live oil. Oil was injected from the top and the melted Wood's metal drained from the bottom of the core holder. Fracture porosity was not measured after the metal was removed from the system. Total core+fracture permeability was not measured after removal of the Wood's metal.

Oil in the fracture was replaced by equilibrium gas. Reported gas injection rate at the beginning of displacement was 5 cm³/min and was later reduced to 0.1 cm³/min. The time at which the rate was changed was not reported. The experiment continued with equilibrium gas injection until no more oil was produced. After 4.2 days of equilibrium gas injection, CO₂ injection was started and lasted for 2.2 days.

With respect to measured surface oil production, Karimaie and Torsaeter (2009) state "The standard volumes of liquid and gas obtained were measured after passing two step condensers at a constant temperature of 5°C (41°F) and -4°C (24.8°F), respectively, to condense any heavy hydrocarbons that may have been carried along with it."

3.4 Uncertainties and error sources

Core porosity defines the fluid in place, but had no direct impact on the fluid displacement process. Core diameter varied between 3.8 and 3.7 cm along the core height. Core diameter variation caused uncertainty in core and fracture pore volume, justifying our use of core (matrix) and fracture porosity as uncertainties used as regression parameters.

Ideally, the study of gravity drainage requires that viscous displacement in the core be eliminated or minimized. Unfortunately, it was observed in the Karimaie experiments that some Wood's metal remained in the space between the core and

core holder. Reported fracture porosity was 93%, and fracture permeability may have been reduced. Porosity reduction of the fracture will affect fracture pore volume. Fracture permeability reduction could affect the recovery mechanism, changing from gravity-dominant to viscous-dominant for gas injection.

Another uncertainty is surface separation efficiency in the lab tests, and the correct modeling of the separation process. It was reported that the produced stream was passed through a two-step condenser 5°C (41°F) and -4°C (24.8°F). But according to direct discussion with Karamaie and observation of the laboratory system, the stream was passed through coiled pipe in an ice-fresh-water bath (condenser) and then flashed to a measuring cylinder at atmospheric pressure. The measuring cylinder was placed in an ice-brine bath. Stream temperature might not reach 5 °C (41 °F) after passing through the condenser. The whole stream was not passed through a -4 °C (24.8 °F) condenser, only the flashed liquid was cooled. According to these observations, temperature of the gas-oil separation was not known with any accuracy, and it is difficult to model accurately.

3.5 Model Description

The matrix block and fractures were initially filled with oil. The fractures were assumed to have negligible capillary pressure. The matrix and the fracture dimensions were the same as core and fracture in the experiment. A two-dimensional radial gridded model was used, where the matrix block was surrounded by two horizontal fractures at the top and bottom and one vertical fracture. Fine gridding was needed for CO₂ gas injection to reduce numerical dispersion and achieve better results. Ten and 51 grid cells were used in radial and vertical directions, respectively.

The *SENSOR* and *Eclipse 300* simulators with implicit solution method were used for simulation models. *Eclipse 300* was used to examine diffusion effects on the production behavior. A 3-component SRK EOS was used. The EOS properties of the components are summarized in Table 3.2 and the binary

interaction parameters are given in Table 3.3. SENSOR and Eclipse 300 models gave the same results without diffusion.

An analytical capillary pressure and relative permeability formulation were used as described in section 2.3. C₁- n-C₅ capillary pressure measured by Christoffersen (1992) at similar core was taken as core capillary pressure in the model. This capillary pressure was scaled with IFT according to the Eq. (2.24) where reference interfacial tension (IFT) is 1.5 mN/m. There was no capillary pressure in the fracture. *Eclipse 300* had the same formulation for scaling capillary pressure and calculating IFT.

The *Pipe-It/Streamz* software was used to calculate cumulative oil and gas production from reservoir simulation results. One separator was defined to simulate produced stream in the experiment. Atmospheric pressure was considered as separator pressure same as the experiment. As mentioned above separator temperature was not measured during the experiment, thus, it was used as a regression parameter.

3.6 Matching Experimental Data

3.6.1 Fracture Permeability

In our work, measured cumulative oil production from the outset of injection (**Table 3.4**) was history-matched. Karimaie (2007) and Karimaie and Torsæter (2009) report recovery factors based on the assumption that injected gas replaces only oil in the space between the core and core holder at early times, and that no oil was produced from the core during that time. That means the oil production before 0.083 day (about 2 hours) amounting to 24 cc in Table 3.4 (compared with 90.5 cc total production during entire test) was neglected in their oil recovery calculation. Their assumption of zero flow resistance in the fracture was shown to be suspect, if not wrong, based on our analysis. Together with some uncertainty in core porosity (i.e. initial oil in place in the core), we decided not to use the Karimaie-reported oil recovery factors in history matching, but instead to match reported surface oil volumes produced from the outset of injection.

To illustrate the impact of fracture flow resistance on oil recovery from the core in the Karimaie experiments, we setup two comparison models where the matrix block is filled initially with oil, and the fracture was initialized with equilibrium injection gas. This condition corresponds to the Karimaie *assumption* at the end of the 0.083 days when all the oil had been removed from the fracture and gas had yet to enter the core.

Table 3.4 – Measured Cumulative Oil and Gas Production

Time days	Cumulative Oil Production cm ³	Cumulative Gas Production L	Time days	Cumulative Oil Production cm ³	Cumulative Gas Production L
0.000	0.0	0.00	2.339	68.0	65.96
0.010	6.0	0.05	2.397	68.0	67.03
0.016	8.0	0.10	2.470	70.0	68.49
0.020	10.0	0.89	2.523	70.0	69.87
0.027	12.0	3.27	2.589	71.0	70.95
0.037	14.0	5.34	3.084	76.0	85.39
0.044	16.0	9.20	3.318	76.0	90.59
0.051	18.0	12.68	3.350	76.0	91.00
0.057	20.0	15.87	3.517	78.0	96.75
0.066	22.0	17.10	4.130	82.0	116.83
0.083	24.0	18.05	4.233*	83.0	117.87
0.182	27.0	18.78	4.264	83.0	122.43
0.191	28.0	18.87	4.277	84.0	123.38
0.244	28.0	19.33	4.291	84.0	124.09
0.368	32.0	21.46	4.391	85.0	133.47
0.757	40.0	30.01	4.410	86.0	138.29
0.908	46.0	38.37	4.437	87.0	140.20
1.128	46.0	38.89	4.462	88.0	145.10
1.141	46.0	39.06	4.483	88.0	145.68
1.208	52.0	44.38	4.606	88.0	147.12
1.254	52.0	44.81	4.639	88.0	150.54
1.280	52.0	45.22	4.668	88.0	151.11
1.313	60.0	54.67	5.154	90.0	166.10
1.462	60.0	56.03	5.187	90.0	166.32
1.487	61.0	56.61	5.458	90.0	169.08
1.506	62.0	56.89	5.500	90.0	172.01
2.037	64.0	59.50	5.520	90.0	172.17
2.085	64.0	60.12	6.129	90.5	191.71
2.108	65.0	60.50	6.229	90.5	197.84
2.116	65.0	60.90	6.379	90.5	202.16
2.320	68.0	65.42			
*CO ₂ injection start					

The fractures had zero capillary pressure and high permeability (100 D) to ensure that flow resistance in the fracture was negligible and that oil recovery from the core was controlled by capillary-gravity drainage. Core porosity and separator temperature were set to 44% and 5 °C (41 °F), respectively, in both models. One model used a capillary pressure curve, where gas drainage was expected only if the core height was greater than the capillary entry height (2.7 cm). In the other model we assumed zero capillary pressure in the core, to provide an extreme (albeit unphysical) case of oil drainage from the core.

Our first model used a chalk capillary pressure curve, the shape of which dictates the rate of oil recovery from the core as gravity and capillary forces balance. Clearly, there exists some uncertainty in the capillary pressure curve and its scaling with IFT (constant for the equilibrium gas injection test). **Fig. 3.1** shows predicted oil production compared with the reported oil recovery by Karimaie using oil production data after 0.083 days. Predictions are significantly lower than reported.

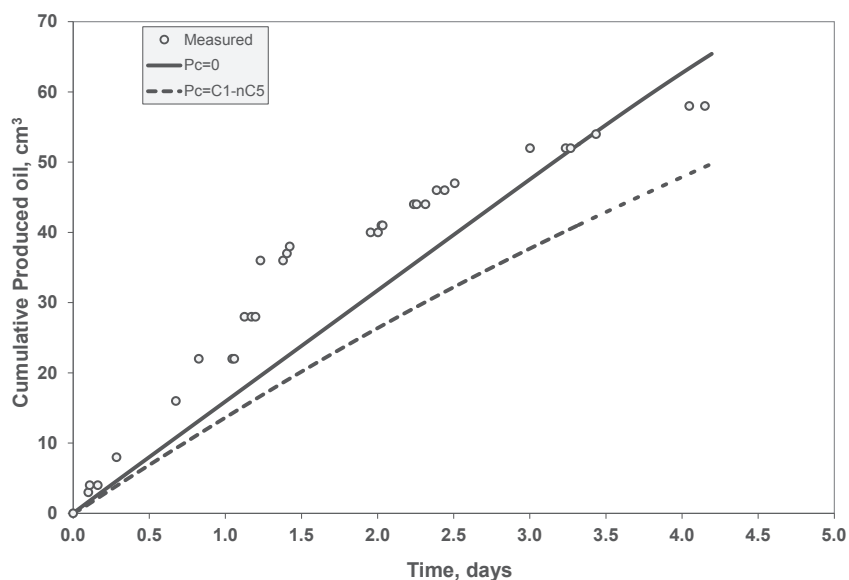


Figure 3.1 – Measured oil production without considering early produced oil and simulation result of assuming gravity-drainage mechanism.

As an extreme treatment of core capillary pressure, we used zero capillary pressure in a second model. The only driving force of recovery is now gravity. Fig. 3.1 shows that even in the absence of capillary pressure in the core, predicted oil recovery was lower than reported recoveries up to 3 days, and had a very different production rate profile than reported.

Our conclusion, as shown in the final model history match of the Karimaie data, was that the oil production from the core starts immediately after gas was injected, and that the core and fracture jointly produce oil over a period significantly longer than 0.083 days. The fracture resistance was found to be significant, and not justifying the assumption of an infinite conductivity fracture.

3.6.2 Equilibrium Gas Injection Rate

It was reported that equilibrium gas was injected at high rate ($5 \text{ cm}^3/\text{min}$) from the top and then decreased to $0.1 \text{ cm}^3/\text{min}$ after 0.083 days. Fig. 3.2 clearly shows a rate change at 0.015 days. However, using $5 \text{ cm}^3/\text{min}$ injection rate in the model

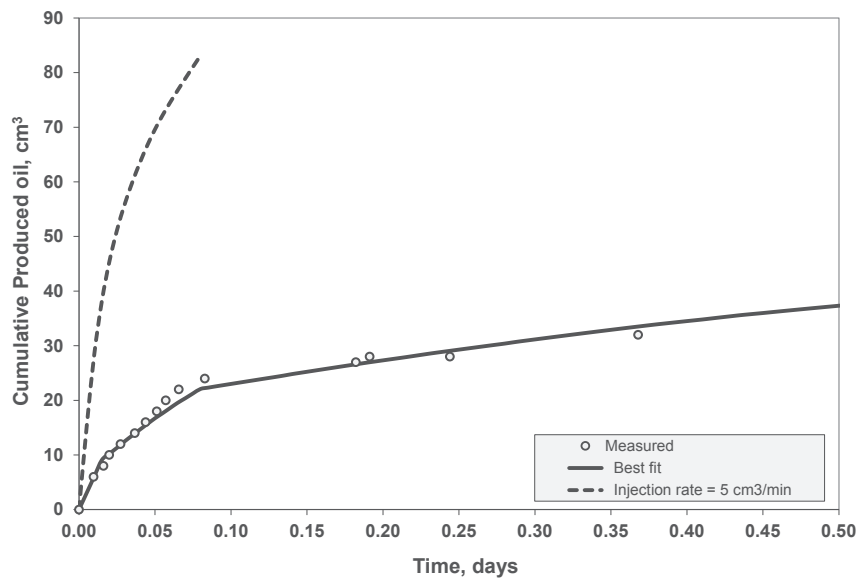


Figure 3.2 – Early measured oil production of the experiment and simulation results of $5 \text{ cm}^3/\text{min}$ injection rate and best fit.

during the time period up to 0.083 days leads to significantly higher oil production than reported experimentally. Our final model used the following injection rates: 1 cm³/min (0<t<0.015 days=22 min), 0.386 cm³/min (0.0150<t<0.083 days=120 min), and 0.1 cm³/min (t>0.083 days); this is to be compared with reported injection rates: 5 cm³/min (0<t<0.083 days), and 0.1 cm³/min (t>0.083 days).

3.6.3 CO₂ Injection Rates

Cumulative gas production was matched reasonably well during equilibrium gas injection, as illustrated in **Fig. 3.3**. There was a rapid increase in gas production when CO₂ injection started. This could be caused by: (a) increasing gas injection rate, (b) change in effective surface temperature and/or (c) decreasing gas formation volume factors. CO₂ was injected from the top, and gas produced from the bottom of core holder. It was expected that equilibrium gas would be produced early during CO₂ injection. On the other hand, Fig. 3.3

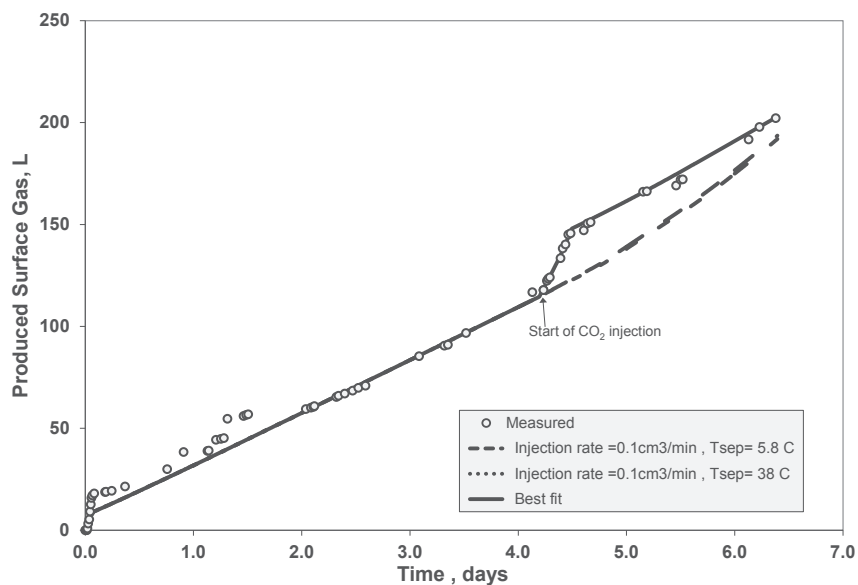


Figure 3.3 – Measured gas production with matched simulation result and results of 0.1 cm³/min injection rate.

indicates that increasing temperature alone could not justify this change of gas production profile. Karimaie does not report an injection rate increase when CO₂ injection starts, but according to gas production behavior in Fig. 3.3 and later communication with Karimaie, the injection rate was in fact increased at about 4 days. By trial and error we found that CO₂ injection rate was increased from 0.1 cm³/min to 0.364 cm³/min at 4.2 days, and then reduced to 0.07 cm³/min at 4.5 days, this CO₂ injection rate profile giving a consistent match to produced gas rate. The final injection rate profile during the entire experiment is shown in **Fig. 3.4**.

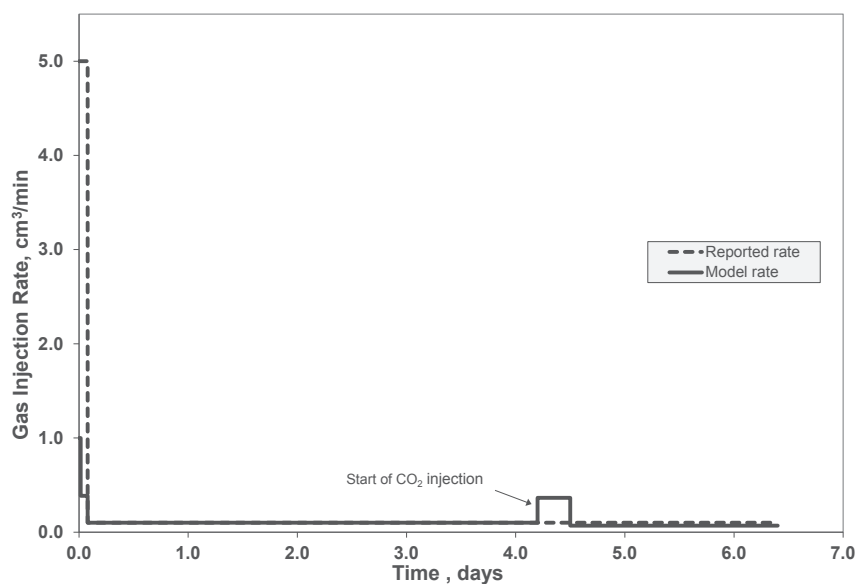


Figure 3.4 – Reported and model gas injection rate profile during the experiment.

3.6.4 Surface Separation

The produced mixture from the core holder was separated with a simple process, namely a flash to atmospheric pressure and temperature controlled by a pre-separation ice-water bath. The effective surface process temperature is assumed to vary with the injection rate, and particularly CO₂ injection because CO₂ has lower thermal conductivity than equilibrium gas. We found that the assumed

separator temperature had a pronounced effect on volume produced, and the surface temperature model used for CO₂ injection was 30 °C (86 °F) in the period 4.2<t<4.5 days, and 26.7 °C (80 °F) for t>4.5 days.

3.6.5 Regression Parameters

A number of laboratory parameters were considered as uncertain to the extent that their value could be adjusted as part of the history matching process. These include: (a) fracture permeability, (b) core residual oil saturation, (c) core porosity, (d) fracture porosity, and (e) separator temperature. Core relative permeability was also considered uncertain, but instead of using an IFT-dependent relative permeability model, we simply considered two cases – mild curvature with exponents $n_g=n_{og}=2$ in Eqs. (2.19) and (2.20), and low-IFT/near-miscible straight-line curves ($n_g=n_{og}=1$). Automated regression was run to obtain a best fit of the measured cumulative oil produced by adjusting the five parameters above (a)-(e). Initial values, lower and upper limits of the regression parameters are given in **Table 3.5**. Because the experiment was conducted at a low IFT (0.15 mN/m) for equilibrium gas injection, and even lower for CO₂ injection, we used two sets of oil-gas relative permeabilities using saturation exponents of 2 and 1 both models giving a reasonable match of lab data (**Fig. 3.5**). Best-fit parameters for core and fracture porosities determined with straight-line relative permeabilities were more consistent with values reported by the lab. IFT decreased during CO₂ injection from 0.15 to 0.0001 mN/m at the displacement front, and therefore the n=1 relative permeability model was considered the most appropriate to simulate the

Table 3.5 – Regression Variables

	Final		Initial value	Lower limit	Upper limit
	n=1	n=2			
Relative permeability	n=1	n=2			
Residual oil saturation (%)	5.1	5.8	10.0	5.0	20.0
Fracture permeability (md)	26.3	20.4	30.0	10.0	100.0
Core porosity (%)	44.5	48.0	44.0	44.0	48.0
Fracture porosity (%)	93.6	89.1	90.0	85.0	100.0
Separator temperature of equilibrium gas injection (°C)	5.8	7.0	5.0	-4.0	15.6

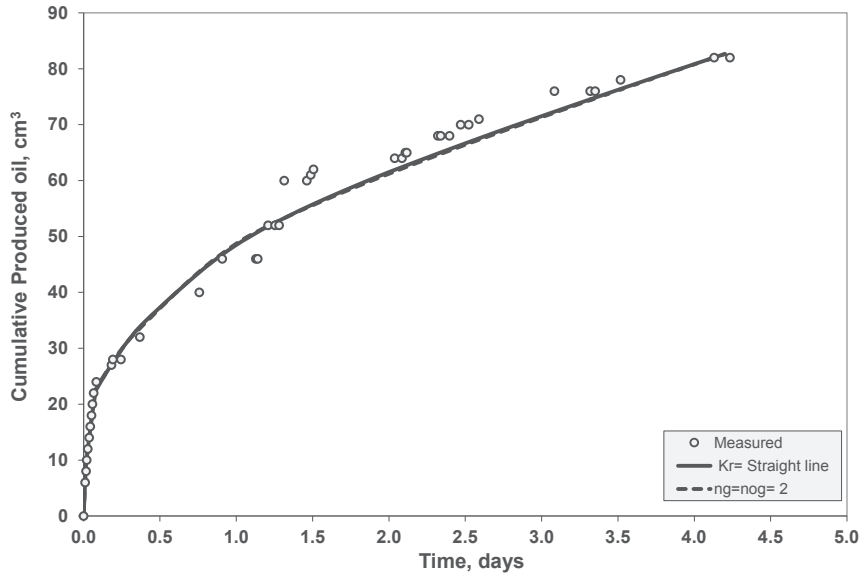


Figure 3.5 – Measured oil production with matched simulation results of equilibrium gas injection period.

CO₂ injection period. Fig. 3.6 shows measured cumulative oil production and simulation results.

3.7 Recovery Mechanism

Reported oil recovery factor was not reliable because (a) it was based on the invalid assumption that only fracture oil, located in the space between the core and core holder, is produced at early times, and (b) initial oil in place used to calculate reported recovery factors was found to be erroneous. In this study, the model oil recovery factor is calculated from oil saturations and is used to study the oil recovery mechanism.

Viscous/gravity ($R_{v/g}$) dimensionless ratios was used to understand the importance of the various recovery mechanisms during production (Wylie and Mohanty 1999; Stalkup 1983; Løvoll et al. 2005):

$$R_{v/g} = \frac{\Delta P_{visc}}{\Delta P_{grav}} = \frac{u\mu_o}{kg\Delta\rho_{og}} \dots\dots\dots(3.1)$$

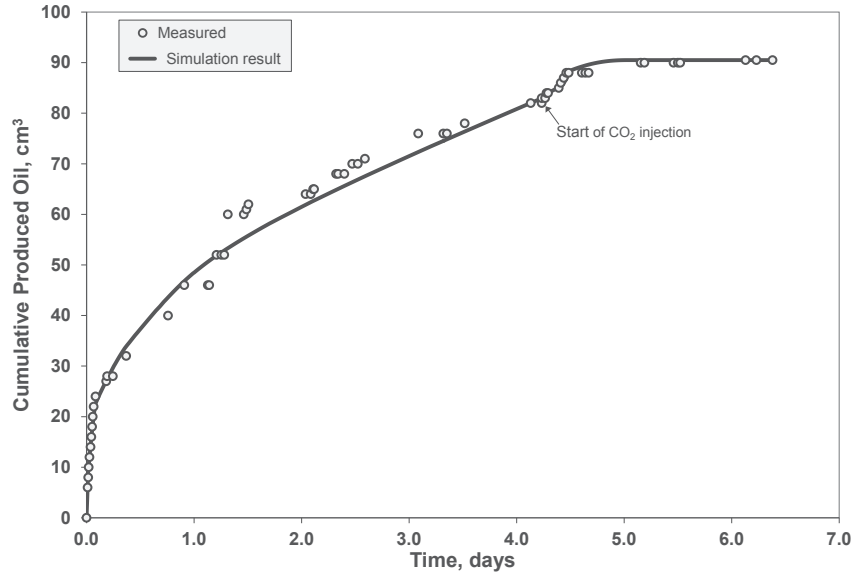


Figure 3.6 – Measured oil production with matched simulation result of equilibrium gas injection and CO₂ injection periods.

where u is linear Darcy velocity in z -direction, μ_o is oil viscosity, k is matrix-block permeability, $\Delta\rho_{og}$ is oil and gas density difference and g is gravity-acceleration constant.

This experiment was conducted to study low interfacial tension gravity drainage in fractured porous media. However, as mentioned above, fracture permeability was not sufficiently large to study fracture-matrix gravity drainage. One characteristic of gravity drainage with equilibrium-gas injection is that oil below the capillary threshold height is not recovered. As shown in **Figs. 3.7-3.10** the displacement front from our history-matched model does not stop above the capillary threshold height (2.7 cm), and hence gravity drainage alone could not be the recovery mechanism. We found that viscous displacement was dominant during equilibrium-gas injection, as verified from a frontal viscous/gravity ratio $R_{v/g}$ of 5.5 calculated at the fifth hour of the experiment.

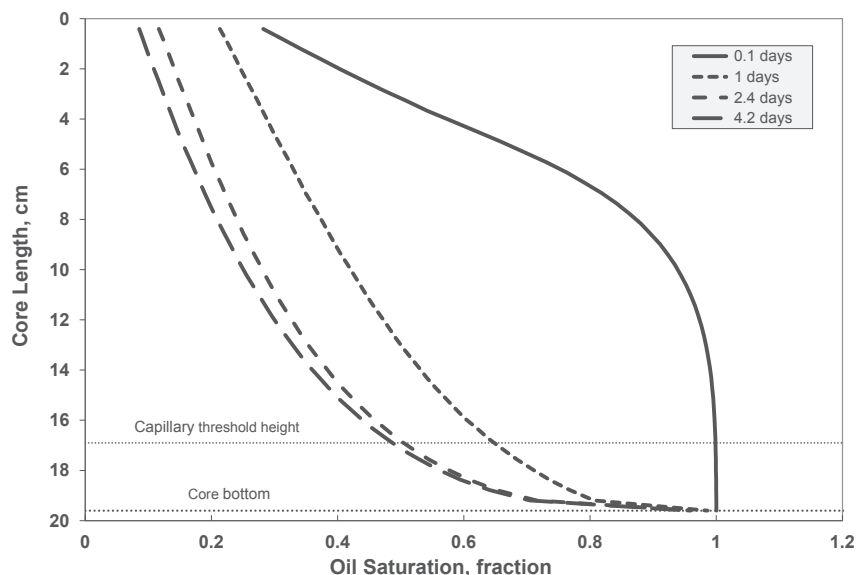


Figure 3.7 – Core oil saturation profile during equilibrium gas injection period from numerical model with linear core relative permeability.

More oil was produced after injecting CO_2 , as shown in Fig. 3.6. At the end of the experiment no oil production was observed while still injecting CO_2 . The model shows that 100% oil recovery was achieved after somewhat more than one PV CO_2 injected. As seen in Fig. 3.11, CO_2 is first-contact miscible with the equilibrium oil and first-contact miscible after reaching 30 mol-% CO_2 content when contacting an equilibrium oil-gas mixture having approximately 60% gas saturation initially. A 100% recovery after about 1 PV CO_2 injected is expected given the thermodynamic miscibility conditions and an efficient top-down, gravity-stable core displacement.

Diffusion was another mechanism that could play a role in production during CO_2 injection period. We examined the effect of diffusion by running the model with and without diffusion transport. As describe in section 2.2, diffusion coefficients were calculated from the extended Sigumnd correlation (da Silva and Belery 1989), given in Table 3.6. As illustrated in Fig. 3.12 average oil saturation of the core was identical for runs with and without diffusion.

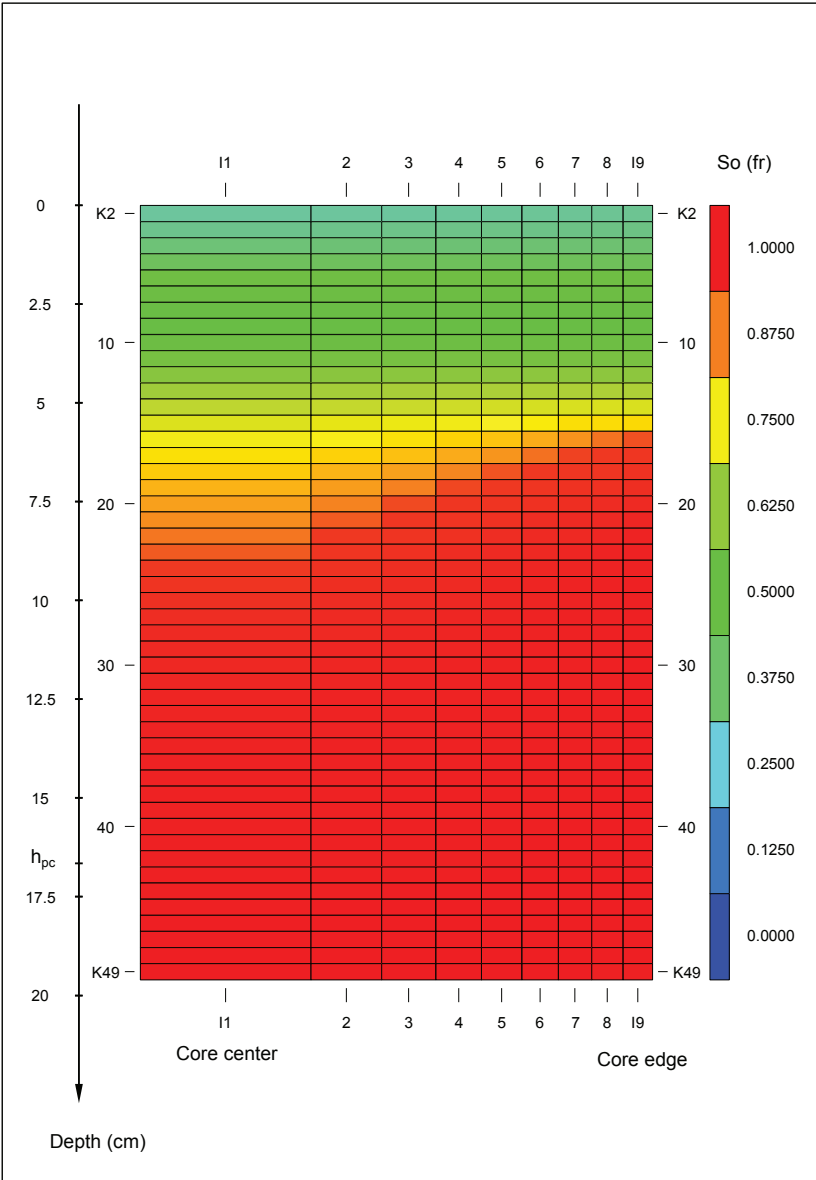


Figure 3.8 – Oil saturation map of core after 2.4 hours for matched model with linear core relative permeability (at about 18% oil recovery).

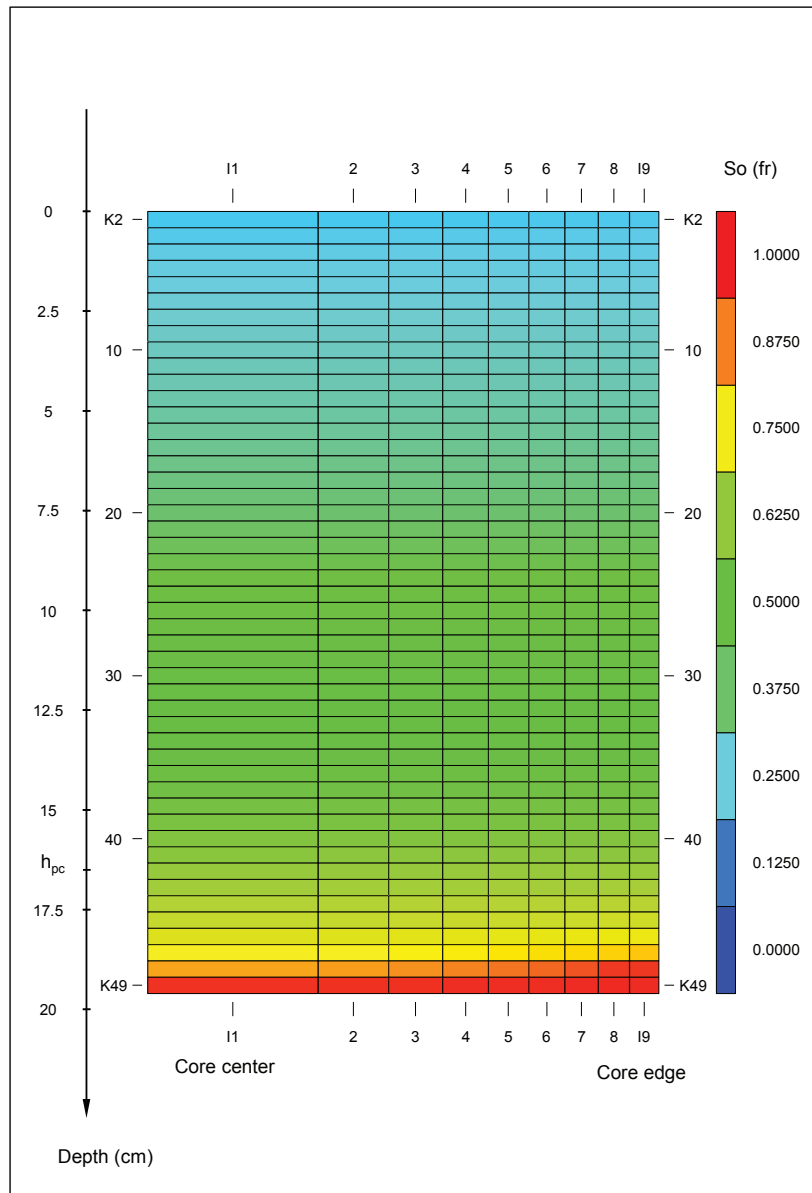


Figure 3.9 – Oil saturation map of core after 1 day for matched model with linear core relative permeability (at about 54% oil recovery).

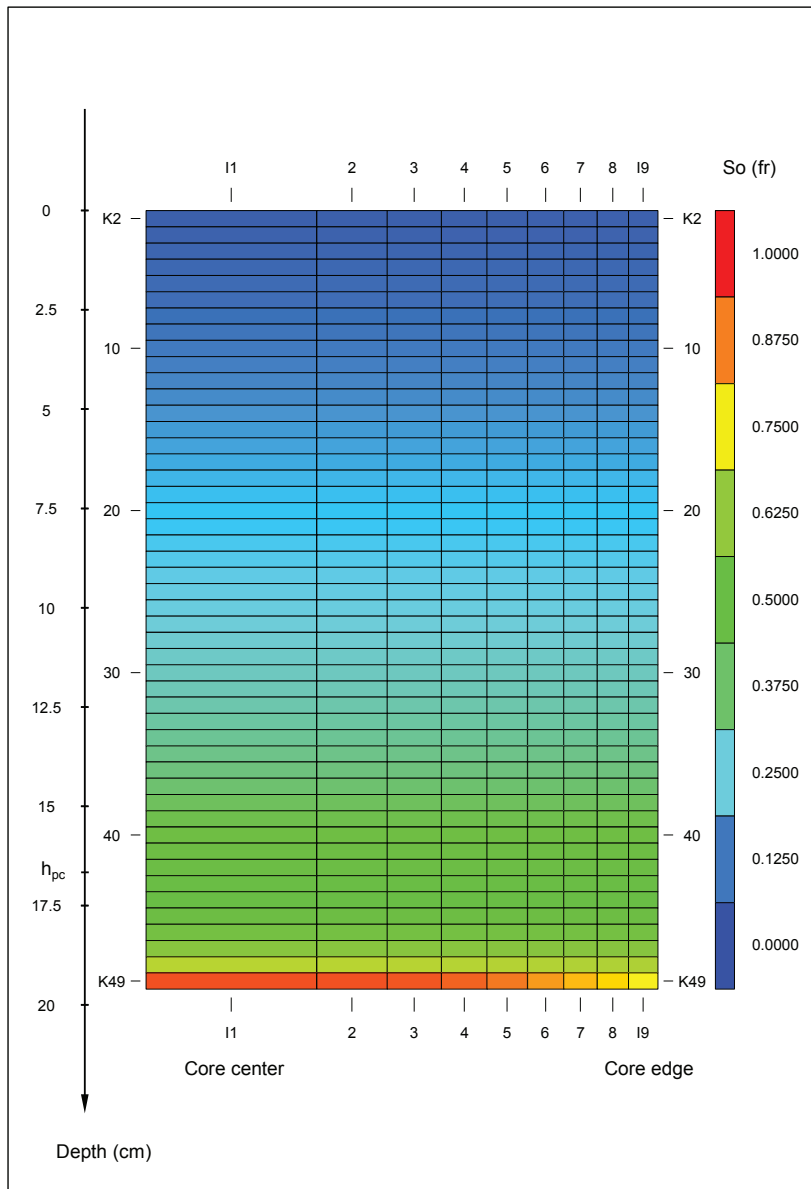


Figure 3.10 – Oil saturation map of core after 4.2 day for matched model with linear core relative permeability (at about 70% oil recovery).

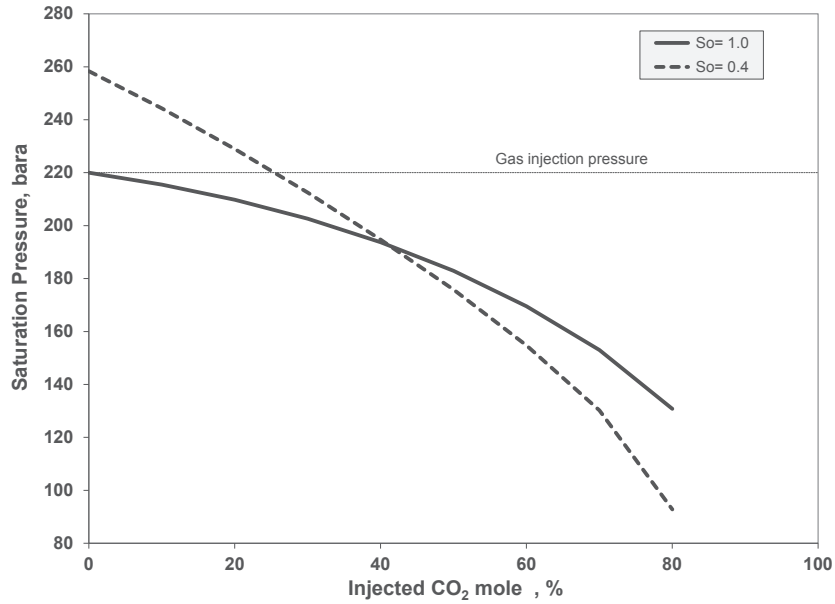


Figure 3.11 – Saturation pressure versus injected CO₂ mole percent calculated by swelling test for 1 and 0.4 oil saturation.

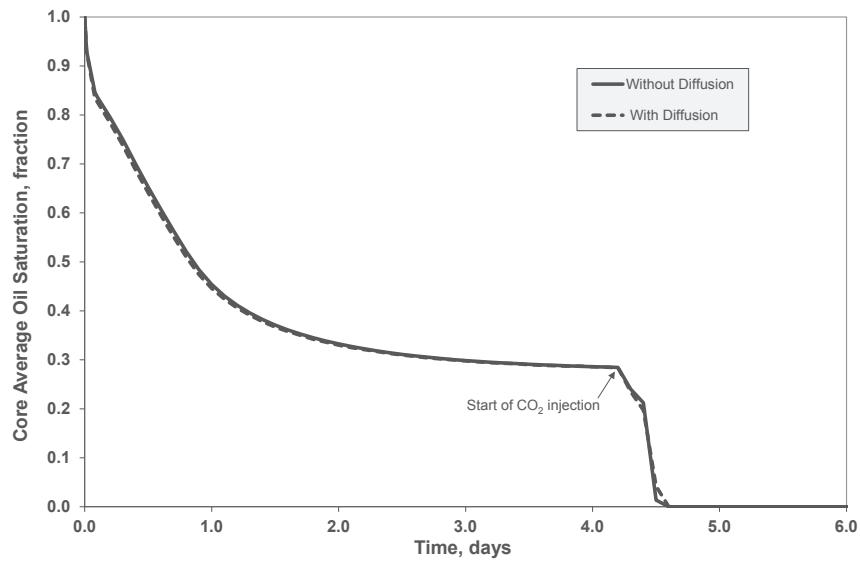


Figure 3.12 – Profile of average oil saturation in the core during equilibrium gas and CO₂ injection period with and without diffusion.

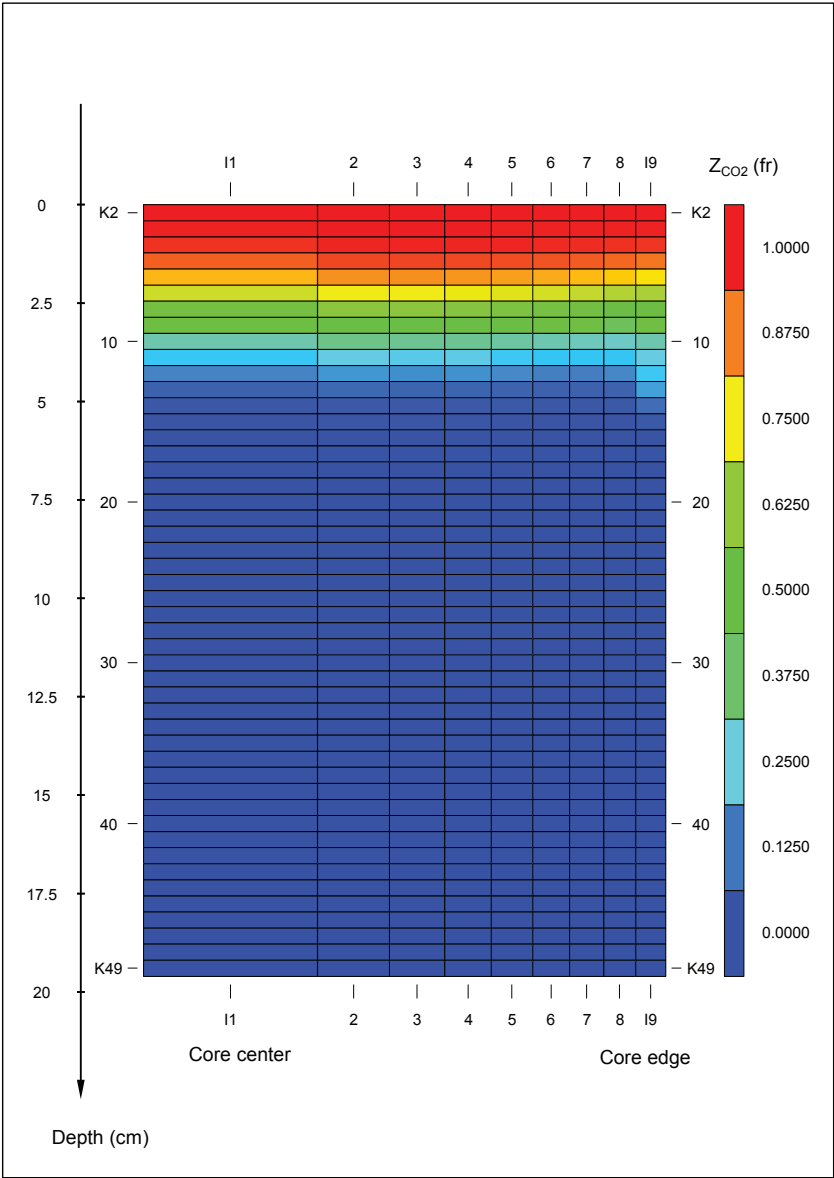


Figure 3.13 – CO₂ mole fraction map of core after 4.25 days for matched model without diffusion effect.

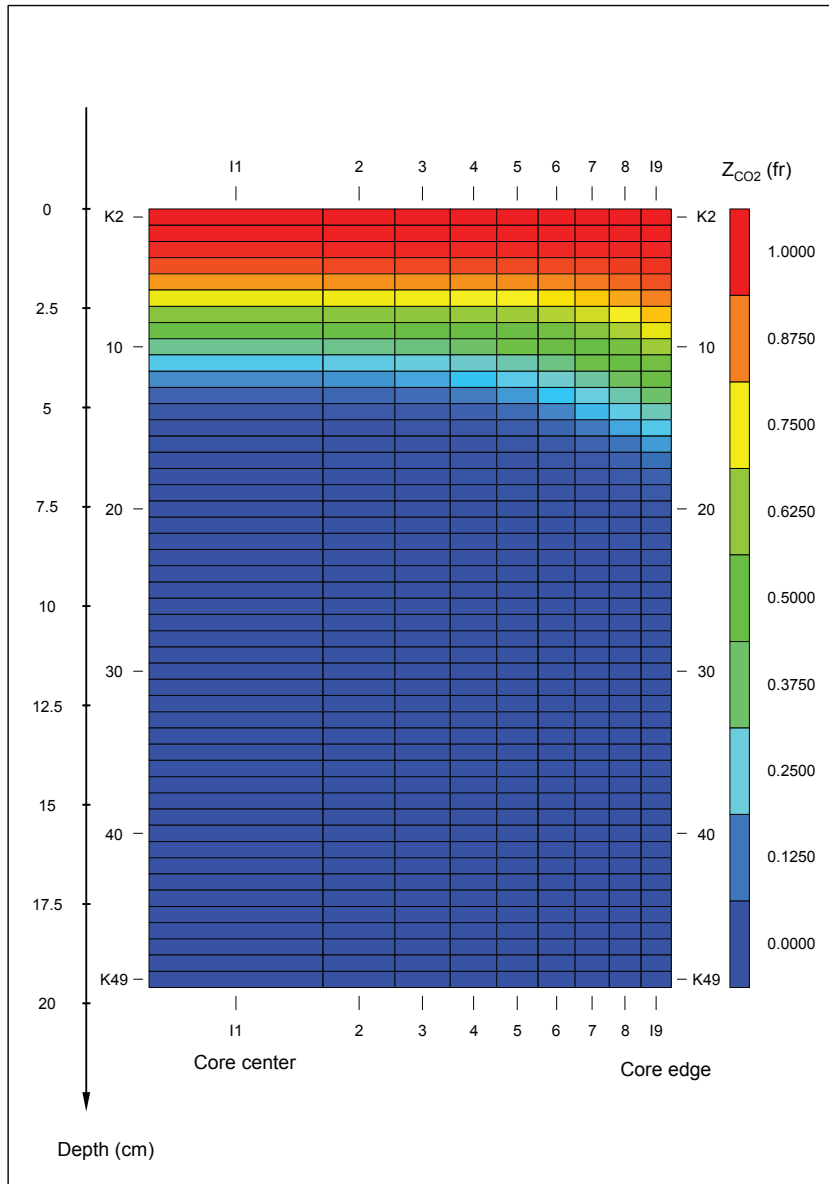


Figure 3.14 – CO₂ mole fraction map of core after 4.25 days for matched model with diffusion effect.

Comparison of CO₂ map at 4.25 days (102 hours) for diffusion and non-diffusion cases revealed small differences, as shown in **Figs. 3.13** and **3.14**. Our results agree with Hoteit and Firoozabadi (2006) who show that diffusion has minor effect in viscous-dominated displacements.

Table 3.6 – Diffusion Coefficients for Oil and Gas Phase

Component	D _o (cm ² /s)	D _g (cm ² /s)	D _g /D _o
C ₁	1.04E-05	3.43E-05	3.3
n-C ₇	1.04E-05	3.43E-05	3.3
CO ₂	1.27E-05	6.45E-05	5.1

Near-miscible and viscous displacements were the main two production mechanisms during CO₂ injection. Pressure gradient caused CO₂ to enter into the core and the core oil was displaced miscibly by CO₂. Model oil saturation profile and gas mole fractions indicate that an oil bank builds ahead of the miscible front (where S_g→0), as illustrated in **Figs. 3.15** and **3.16**. Note that the oil carrying capacity of gas ahead of and behind the front increases with time.

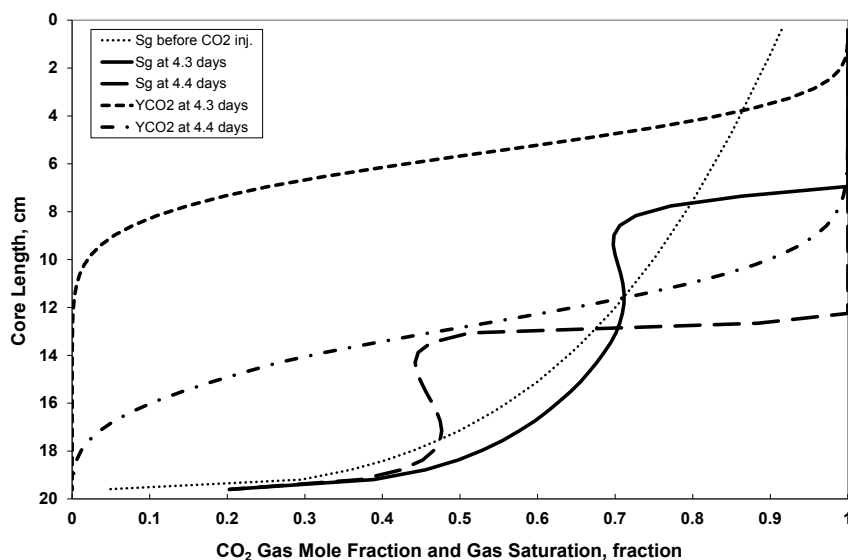


Figure 3.15 – Profile of CO₂ gas mole fraction and gas saturation in the core during CO₂ injection period.

Because oil was produced from both the matrix and the fracture at early times, it is difficult to calculate matrix recovery factor based on produced oil. Therefore matrix oil recovery was calculated from total average oil saturation S_o in the core using the following relation:

$$RF = \left(1 - \frac{S_o}{S_{o_{ini}}}\right) \dots\dots\dots(3.2)$$

For model results at a given time, the calculated oil recovery from Eq. (3.2) is slightly higher than oil recovery calculated based on production. The difference stems mainly from the oil carried in solution in the gas behind the displacement front, this oil being produced (by surface condensation) only after the enriched CO_2 -rich gas reaches the end of the core and is produced. Calculated oil recovery is shown in **Fig. 3.17**. About 70% of the initial oil in place in the core was recovered by equilibrium gas injection and all residual oil was produced by CO_2 injection at the end of the experiment.

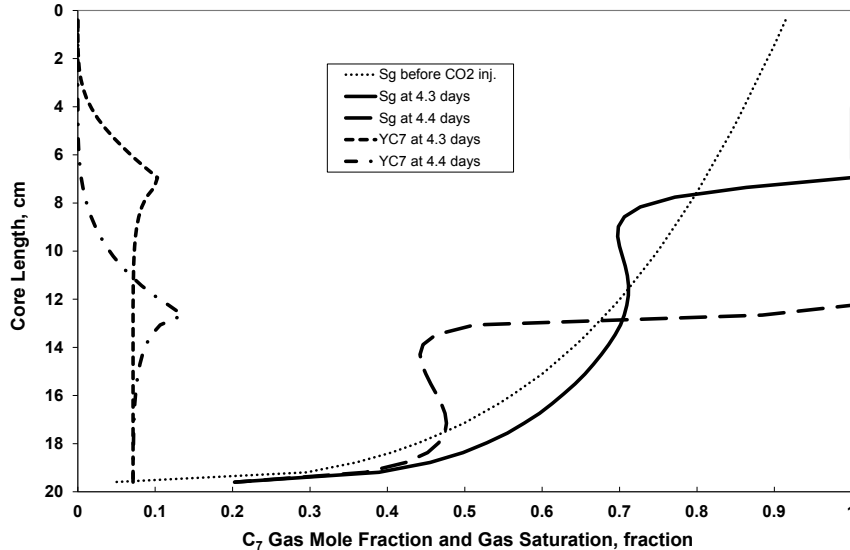


Figure 3.16 – Profile of n-C₇ gas mole fraction and gas saturation in the core during CO₂ injection period.

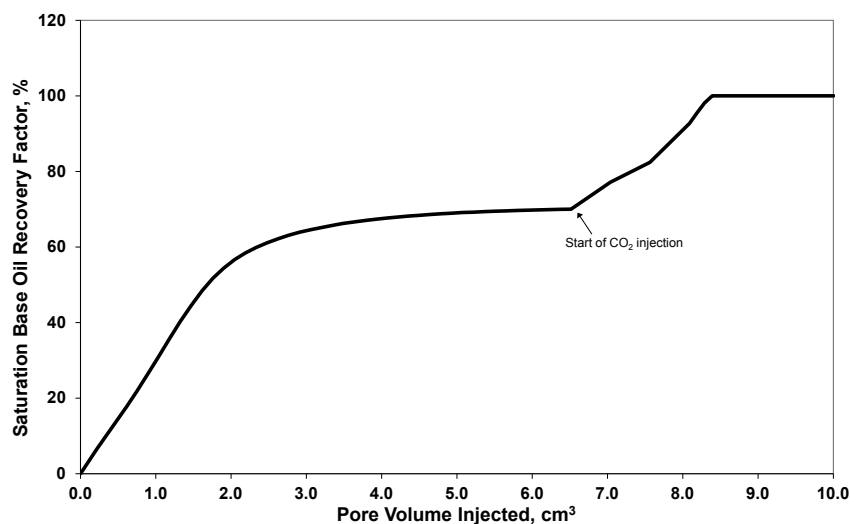


Figure 3.17 – Calculated oil recovery factor based on core oil saturation.

3.8 Designing Fractured Reservoir Experiments using CO₂

We recommend the following experimental design procedures when performing CO₂ injection experiments for fractured reservoirs:

1. Fracture (core-annulus) permeability should be measured after the core is initialized with oil. A rule-of-thumb for fracture conductivity is that total core+fracture pressure drop is small compared the pressure drop when flow occurs only through the core.
2. Continuous measurement of separator temperature and pressure.
3. Oil and gas produced mass and volume should be reported, together with periodic surface oil densities.
4. Periodic measurement of produced surface gas and surface oil stream assumptions.
5. Oil and gas compositions initially saturating the core should be determined experimentally.
6. Additional PVT experiment like a swelling test that includes bubblepoint, near-critical, and dewpoint mixtures should be conducted for tuning the EOS model.

7. Determine relevant (drainage and/or imbibition) capillary pressure and relative permeability of core used in the experiment.

3.9 Conclusions

Based on analysis of experimental results and a history-matched numerical model which describes accurately all key laboratory performance data; we make the following conclusion, which are specific to this particular experimental study:

1. Viscous displacement is significant and gravity-capillary drainage is not significant in the Karimaie experiments due to low “fracture” (core-annulus) permeability.
2. The laboratory data history matched include cumulative oil and gas produced during displacements with equilibrium gas and CO₂ injection.
3. During the CO₂ injection period, near-first-contact miscible displacement is the dominant production mechanism.
4. Separator conditions play an important role in measuring and modeling oil production for high-pressure, high-temperature CO₂ injection experiments – mainly because reservoir gas contains significant oil in solution which is produced by condensation at surface conditions.
5. Diffusion has no impact on the CO₂ injection recovery mechanism because of the dominant viscous-force displacement.

3.10 Reference

Christoffersen, K. 1992. High-Pressure Experiments with Application to Naturally Fractured Chalk Reservoirs. PhD Dissertation, NTNU, Trondheim, Norway.

Coats Engineering: *SENSOR*, www.coatsengineering.com.

Hoteit, H. and Firoozabadi, A. 2006. Numerical Modeling of Diffusion in Fractured Media for Gas Injection and Recycling Schemes. Paper SPE 103292 presented at the 2006 SPE Annual Technical Conference and Exhibition, San Antonio, Texas, U.S.A., 24-27 September.

- Karimaie, H. 2007. Aspects of Water and Gas Injection in Fractured Reservoir. PhD Dissertation, NTNU, Trondheim, Norway.
- Karimaie, H. and Torsæter, O. 2009. Low IFT Gas-Oil Gravity Drainage in Fractured Carbonate Porous Media. *Journal of Petroleum Science and Engineering*.
- Løvoll, G., Meheust, Y., Måløy, K. L., Aker, E., and Schmittbuhl, J. 2005. Competition of gravity, capillary and viscous forces during drainage in a two-dimensional porous medium, a pore scale study. *Energy* 30 (6): 861–872. doi:10.1016/j.energy.2004.03.100.
- Petrostreamz AS: *Pipe-It/Streamz*, www.petrostreamz.com.
- Talukdar, S. 2002. Ekofisk Chalk: core measurements, stochastic reconstruction, network modeling and simulation. PhD Dissertation, NTNU, Trondheim, Norway.
- Schlumberger: *ECLIPSE 300* Reservoir Engineering Software. 2009. www.slb.com.
- Stalkup, F.I. Jr. 1983. Miscible Displacement. Henry L. Doherty Monograph Series, SPE, Richardson, Texas, USA, 8.
- Wylie, P.L. and Mohanty, K.K. 1999. Effect of Wettability on Oil Recovery by Near-Miscible Gas Injection. *SPE Res Eval & Eng* 2 (6): 558–564. SPE-59476-PA. doi: 10.2118/59476-PA.
- Zick Technologies: *PhazeComp*, www.zicktech.com.

Chapter 4

Modeling CO₂ Injection in Darvish Fractured Chalk Experiment (Sw=0%)

4.1 Introduction

This chapter presents a modeling study of a CO₂ injection in a chalk core based on the laboratory data that were reported by Darvish *et al.* (2006). The experiment consisted of a vertically-oriented, 60-cm-long chalk outcrop core that was initially saturated with live reservoir oil at 130 °C and 300 bar. After saturating the core with the oil mixture by displacement, a small fracture volume surrounding the core was created by heating the solid Wood's metal that originally filled the volume between the core and core holder. CO₂ was then injected for 22 days. The experiment was performed at a pressure above the minimum miscibility pressure (MMP), as defined by a traditional 1D multi-contact displacement process (MMP_{1D}).

Darvish *et al.* (2006) was not able to match the experimental data to the numerical compositional model. This lack of a match may have resulted from the use of an improper equation of state (EOS) or incorrect input data in their models. Moortgat, Firoozabadi and Farshi (2009) modeled the experiment using the combined discontinuous Galerkin, mixed-hybrid, finite-element and discrete-fracture techniques. Our modeling study was conducted using a compositional reservoir simulator. The 2D, r-z model used a fine grid for the core and surrounding fracture.

4.2 Rock and Fluid Properties

A chalk core from the Faxø area outcrop in Denmark was used in this experiment; it has rock properties that are similar to those of North Sea chalk. The core had a cylindrical shape with a length of 59.6 cm and a diameter of 4.6 cm. The core porosity and permeability have been reported as 44.4% and 4 md, respectively (Darvish *et al.* 2006; Darvish 2007).

Relative permeabilities and capillary pressures for the core were not measured. We used the C_1 - n - C_5 capillary pressure of a Faxø outcrop chalk core, as measured by Christoffersen (1992). The linear and Corey-type relative permeabilities (Eqs. (2.19) and (2.20)) were used for modeling the experiment. The gas and oil exponents for the Corey-type relative permeabilities were 2.4 and 3.8, respectively, with unit end points.

The reservoir fluid was flashed to standard conditions ($T= 15.5$ °C, $P= 1$ bar), and the flashed oil and gas compositions were measured using the techniques in Darvish 2007. These fluids were used to determine the reservoir fluid composition at a bubble point pressure of 242 bar and a temperature of 130 °C by combining it with the measured gas/oil ratio (GOR) of 133.2 Sm^3/Sm^3 . The EOS model had 39 components, including the non-hydrocarbons N_2 and CO_2 , the hydrocarbon components C_1 , C_2 , C_3 , i - C_4 , n - C_4 , i - C_5 , n - C_5 , and C_6 and the single-carbon number (SCN) components C_7 , C_8 , ..., C_{33} and C_{34} with a C_{35+} residue. The EOS was reduced to thirteen components with five heavy pseudo-components. The lumped components were chosen to be the same as the pseudo-components that were reported by Darvish in 2007 because the reported oil-produced mass fractions were to be compared with the numerical model results. The Peng-Robinson (1979) equation of state (PR-EOS) with a volume shift was used. The PR-EOS was tuned to match the measured constant composition expansion (CCE), the differential liberation expansion (DLE) and the CO_2 swelling test experiments. The comparisons of the measured and calculated properties are shown in **Figs. 4.1 – 4.5**. The Lohrenz-Bray-Clark (LBC) compositional viscosity correlation is usually adequate for gas viscosity

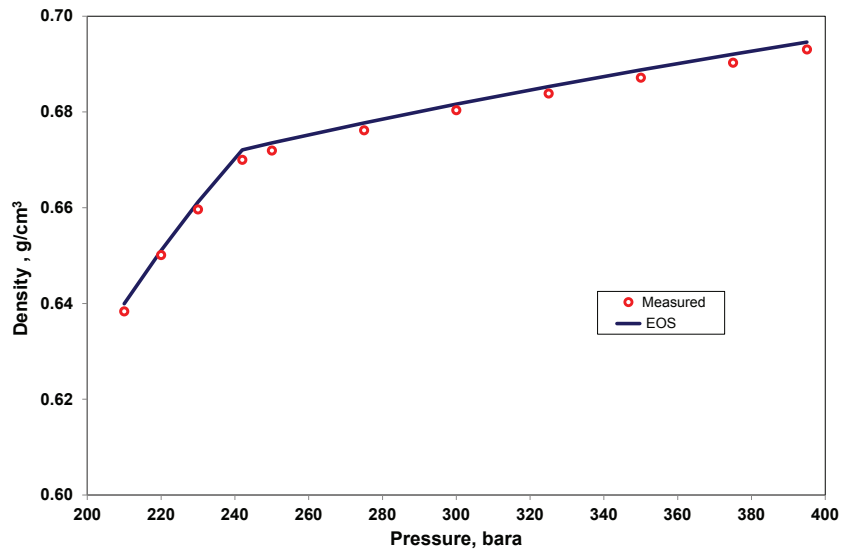


Figure 4.1 – Measured and calculated total (gas + oil) density at 130 °C.

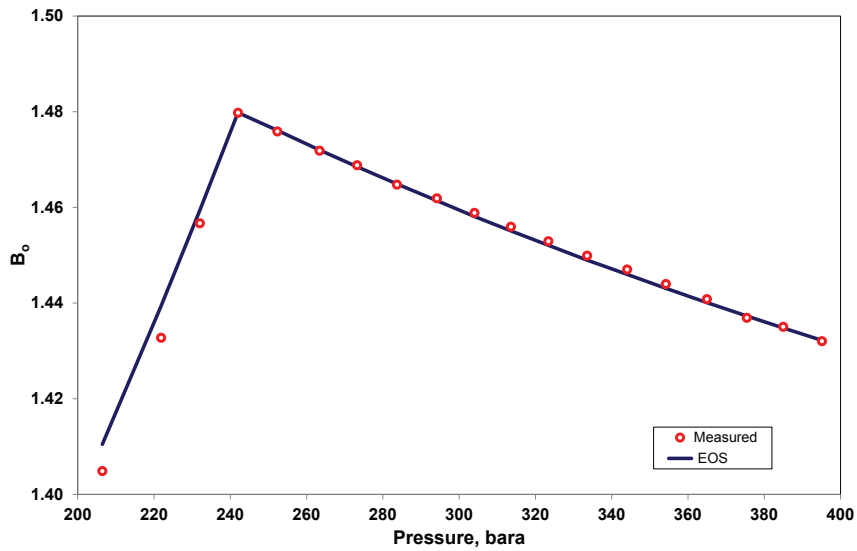


Figure 4.2 – Measured and calculated differential oil volume factor at 130 °C.

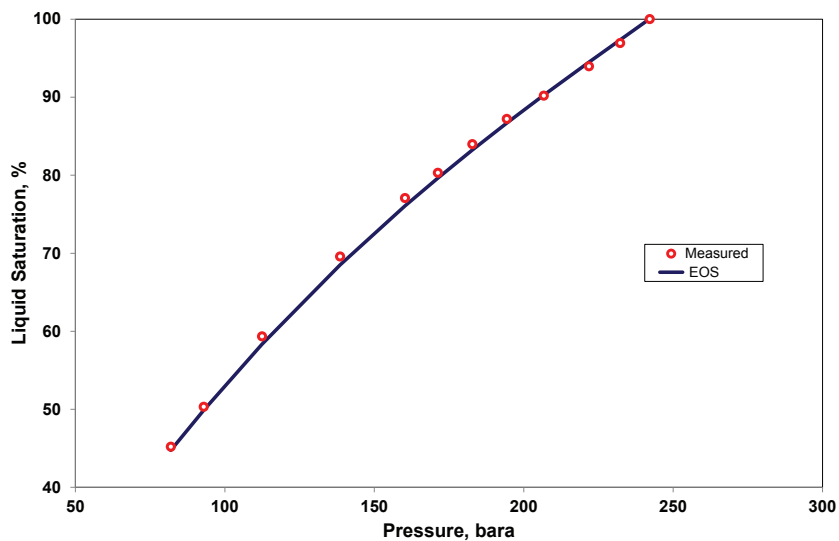


Figure 4.3 – Measured and calculated liquid saturation at 130 °C.

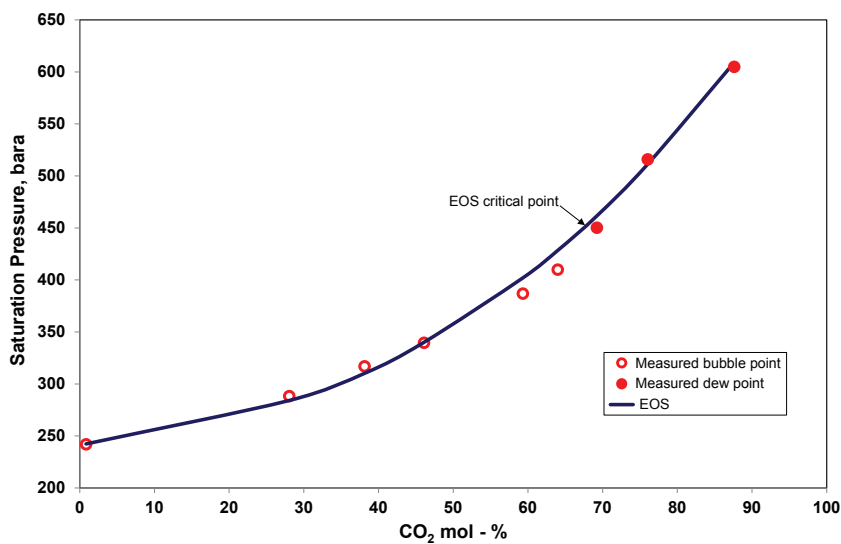


Figure 4.4 – Measured and calculated saturation pressure versus CO₂ mole injected at 130 °C from CO₂ swelling test.

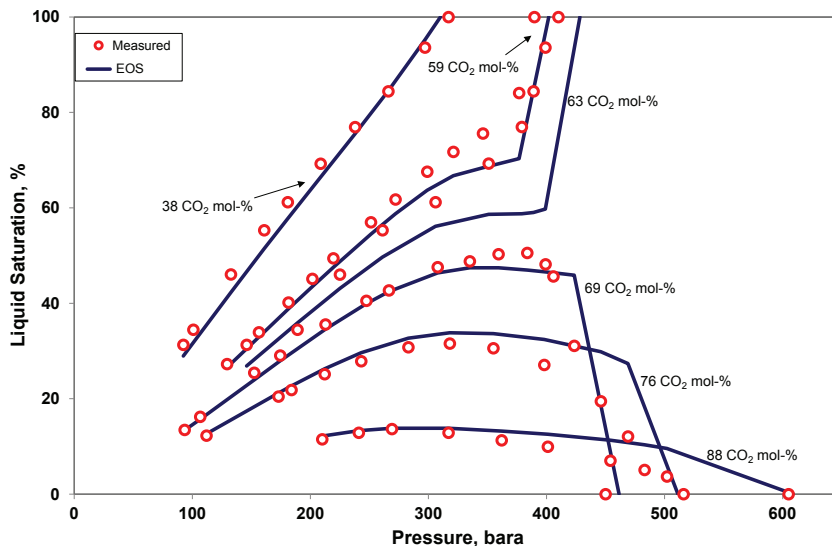


Figure 4.5 – Measured and calculated liquid saturation for different CO₂ mol-% mixtures from CO₂ swelling test.

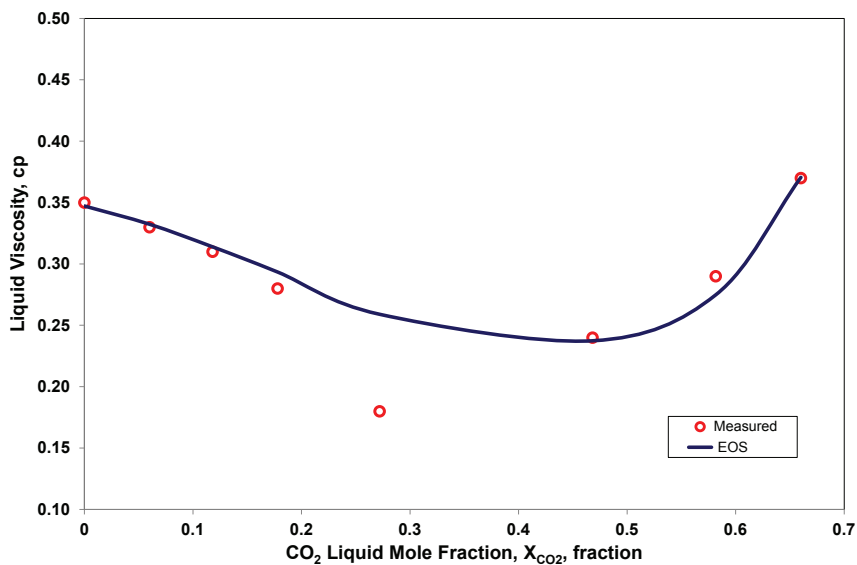


Figure 4.6 – Measured and calculated saturated oil viscosity versus CO₂ liquid mole fraction at 130 °C.

Table 4.3 – Fluid Composition and K-Value at Saturation Pressure (242 bara) an 130 °C

Component	Z _i	X _i	Y _i	K-Value
N2	0.0012	0.0012	0.0034	2.79E+00
CO2	0.0084	0.0084	0.0105	1.24E+00
C1	0.4473	0.4473	0.8026	1.79E+00
C2	0.0766	0.0766	0.0840	1.10E+00
C3	0.0426	0.0426	0.0340	7.98E-01
C4	0.0318	0.0318	0.0197	6.18E-01
C5	0.0220	0.0220	0.0100	4.57E-01
C6	0.0211	0.0211	0.0071	3.34E-01
C7-C9	0.0799	0.0799	0.0176	2.20E-01
C10-C15	0.0988	0.0988	0.0089	8.98E-02
C16-C22	0.0654	0.0654	0.0019	2.93E-02
C23-C34	0.0540	0.0540	0.0004	6.76E-03
C35+	0.0510	0.0510	0.0000	4.50E-06
MW	106.613	106.613	23.940	
Z-Factor	1.15E+00	1.15E+00	9.11E-01	
Density (kg/m ³)	672.16	672.16	189.87	

4.3 Experimental Procedure

This section describes an experiment that was performed to study CO₂ injection in fractured reservoir. The experimental procedure that is described was based on Darvish (2007), Darvish *et al.* (2006) and personal communications with Darvish.

A dried cylindrical chalk core was placed in a steel core holder. The core holder inner diameter was 5.0 cm. The core diameter was 4.6 cm, and the length was 59.6 cm. The fracture was represented by a 2 mm space between the core and the core holder. The core porosity and absolute permeability were reported as 44.4% and 4 md, respectively (Darvish 2007; Darvish *et al.* 2006).

Due to the large permeability contrast between the core and the surrounding space (the artificial fracture), the process of initially saturating the core with live oil was complicated. The oil would flow through the highly-permeable space, leaving the core partially saturated with live oil. Therefore, the space between the core and the core holder wall was initially filled with Wood's metal. The metal's melting point is 70 °C, and the experiment was performed at 130 °C. The metal

was melted and poured into the space between the core and core holder. The fracture sealed with the metal and had zero permeability after the system was cooled.

The core was evacuated and pressurized to 300 bar with 85% toluene and 15 % Exxsol. The Toluene-Exxsol mixture had a higher density than the experimental fluid, and therefore, this mixture was injected from the top of the core with stable gravity displacement. Two pore volumes of live oil were injected at a constant pressure (300 bar) and temperature (40 °C). The system was heated to 130 °C at a constant pressure (300 bar), and the Wood's metal was removed from the annular space by injecting the oil. The oil was injected from the top and the metal drained from the bottom of the core holder. The fracture porosity and permeability were not measured after the metal was removed from the system, but the pressure difference was measured between the top and the bottom of the core holder, which was used in this work to determine the fracture permeability for the model.

The oil in the fracture was replaced by CO₂. The injection rate during the first 30 min of the experiment was 5.6 cm³/min and was then reduced to 0.1 cm³/min. The CO₂ gas injection was continued for 22 days. The fluid that was produced was diverted to a separator at ambient conditions. The mass of the separated oil was measured continually, and the component mass fractions were measured periodically gas chromatography.

4.4 Model Description

The matrix block (core) was initially filled with oil, and the fractures were initially filled with CO₂. The fractures were assumed to have negligible capillary pressure. The matrix and the fracture dimensions were the same as those of the core and the fracture in the experiment. A two-dimensional radial grid was used in which the matrix block was surrounded by two horizontal fractures (at the top and bottom) and one vertical fracture. A fine grid was required to reduce numerical dispersion in the CO₂ gas injection. 10 and 51 grid cells were used in the radial and vertical directions, respectively, to simulate the experiment.

The *ECLIPSE 300* simulator with an implicit solution method was used for all of the simulations. A 13-component PR-EOS was used. The EOS properties of the components are summarized in Table 4.1, and the binary interaction parameters are given in Table 4.2.

Linear and Corey-type relative permeabilities were used to model the experiment. The gas and oil exponents for the Corey-type relative permeabilities were 2.4 and 3.8, respectively, with unit end points. The C₁-n-C₅ capillary pressures that were measured by Christoffersen (1992) at a similar core were used as the core capillary pressures in the model. These capillary pressures were scaled with IFT according to Eq. (2.24), in which the reference interfacial tension (IFT) was 1.5 mN/m. There was no capillary pressure in the fracture.

The *Pipe-it/Streamz* software was used to calculate the cumulative mass of the oil that was produced from the reservoir simulation results. One separator was defined to simulate the produced stream in the experiment. The separator pressure was atmospheric, as it was in the experiment. As mentioned above, the separator temperature was not measured during the experiment.

The oil and gas effective diffusion coefficients are given in Table 4.4. The gas diffusion coefficients were determined from the equilibrium gas at the bubble point pressure. More details of the diffusion coefficients calculation are given in section (2.2).

4.5 Matching The Experimental Data

In this section, we try to match the measured experimental data. As was mentioned above, the cumulative mass of the separator oil was measured and matched. The oil recovery that were reported in Darvish (2007) and Darvish *et al.* (2006) were based on the mass produced and were not mentioned in the above references. In their study, Moortgat, Firoozabadi and Farshi (2009) considered that to be the volumetric oil recovery. A fracture permeability of 80 md was needed to obtain the pressure difference that was measured in the experiment. As shown in **Fig. 4.7**, the measured pressure difference was slightly higher than the calculated pressure difference because we accounted for the pressure drop in the

**Table 4.4 – Gas and Oil Diffusion Coefficients
and Initial Oil Composition**

Component	z_i mole fr.	D_{ig} cm^2/s	D_{io} cm^2/s
N2	0.0012	5.15E-05	2.92E-06
CO2	0.0084	3.20E-04	7.26E-06
C1	0.4473	2.70E-04	7.72E-06
C2	0.0766	2.62E-04	7.09E-06
C3	0.0426	2.46E-04	5.84E-06
C4	0.0318	2.09E-04	4.91E-06
C5	0.0220	1.81E-04	4.25E-06
C6	0.0211	1.64E-04	3.83E-06
C7-C9	0.0799	1.42E-04	3.25E-06
C10-C15	0.0988	1.05E-04	2.55E-06
C16-C22	0.0654	7.66E-05	2.01E-06
C23-C34	0.0540	5.72E-05	1.52E-06
C35+	0.0510	4.30E-05	1.33E-06

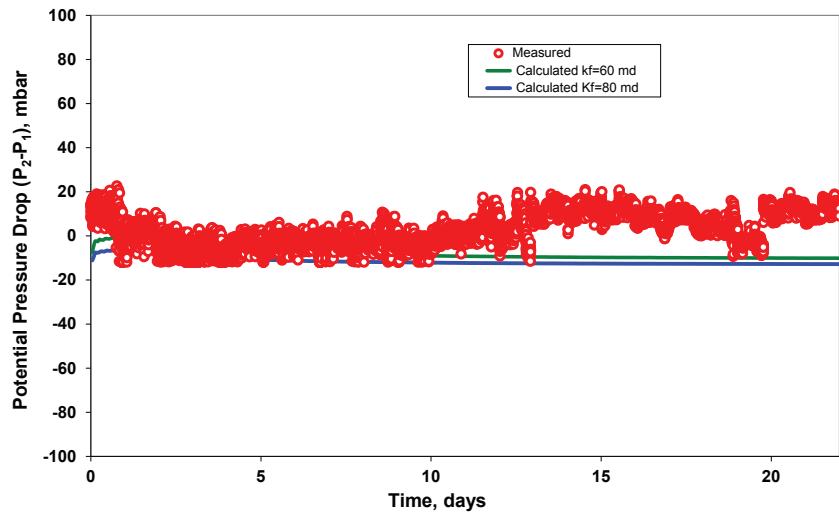


Figure 4.7 – Measured and calculated saturated oil viscosity versus CO₂ liquid mole fraction at 130 °C.

inlet and outlet tubes, which were where the measurement instruments for the experiment were set. No condenser or cooler was present in the outlet stream, and consequently, the separator temperature was set to 30 °C, which was slightly higher than the ambient temperature when accounting for the high temperature (130 °C) of the outlet fluid.

The other parameters in the numerical model were defined as reported values in the experiment. The two models were run with two sets of relative core permeabilities, as described in the previous section. The results of the models were similar, as illustrated in **Fig. 4.8**. The mass transfer mechanism was more pronounced than the viscous displacement in the present experiment, as will be discussed in the next section. We selected the model with linear core relative permeability for use in the remainder of the study.

Reported heavy-component mass fractions in the experiment were compared with the numerical model results. All of the calculated mass fractions from the model followed the same trend as the measured values, as shown in **Fig. 4.9**. If the C₁₀ and heavier components are lumped together, then numerical model

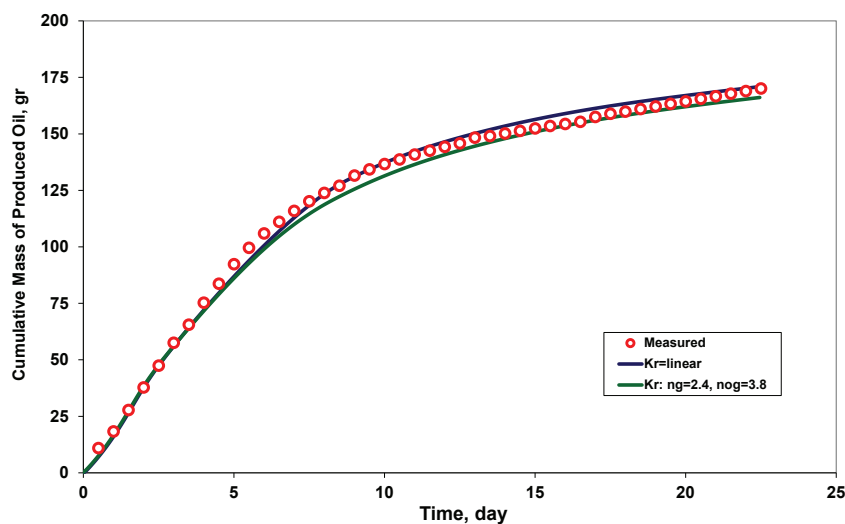


Figure 4.8 – Measured produced oil mass with matched simulation results for two set of core relative permeability with 80 md fracture permeability at 30 °C separator temperature.

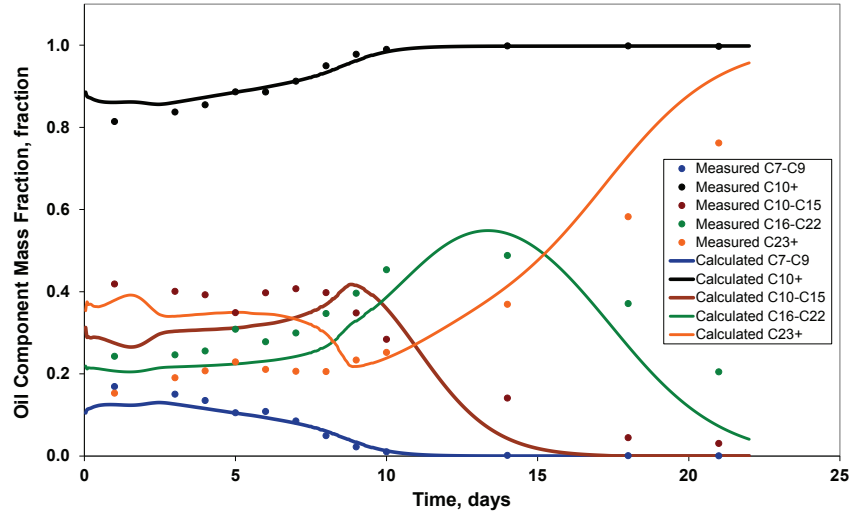


Figure 4.9 – Measured and calculated heavy components mass fraction of produced oil at separator condition.

results and the experimental data are even closer, as shown in Fig. 4.9. This result might indicate that the grouping of the C_{10+} components was performed slightly differently in the laboratory than in the EOS calculations. The calculated molecular weights of the stock tank oil produced in the laboratory have the same trend as the molecular weights in the numerical model (Fig. 4.10).

4.6 Recovery Mechanism

Darvish (2007) converted the initial volume (V_{oi}) in the core to an equivalent mass under laboratory separator conditions ($m_{oi} = V_{oi}\rho_o/B_o$), and the recovery was calculated using:

$$RF_{surf} = \frac{m_{op}}{m_{oi}} = \frac{m_{op}}{V_{oi} \left(\frac{\rho_o}{B_o} \right)} \dots\dots\dots (4.1)$$

The composition of oil that was produced varied during the experiment (Fig. 4.9); as a result, the oil density (ρ_o) values and the oil formation volume factor (B_o) were not constant. Darvish (2007) used a constant oil density and oil

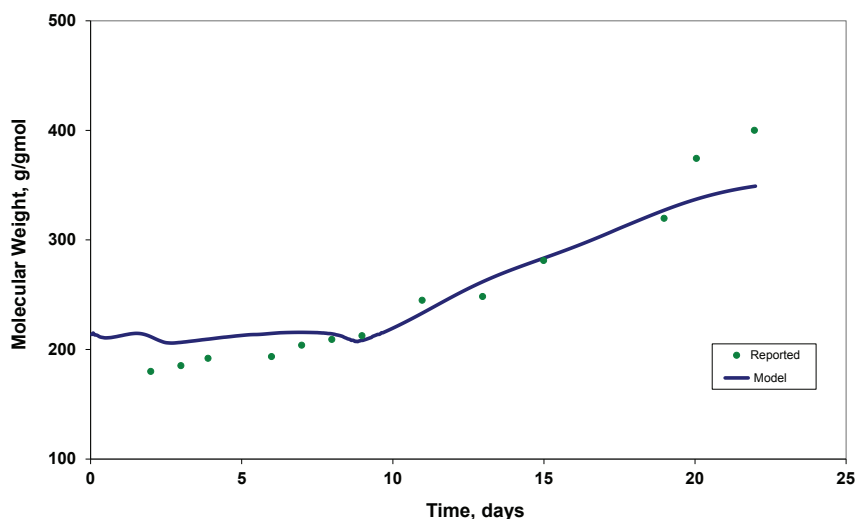


Figure 4.10 – Reported and calculated molecular weight of produced oil at separator condition.

formation volume factor in his calculations. Therefore, in the present study, we did not use the recovery factor calculated by Darvish (2007).

Fig. 4.11 shows CO₂ condensation in the oil phase at the experimental pressure and temperature. Consequently, the oil saturation should be corrected as follows:

$$RF_{so} = 1 - \frac{S_o(1 - x_{CO_2} + x_{CO_2i})}{S_{oi}} \dots\dots\dots(4.2)$$

where S_{oi} and S_o are the initial and current oil saturations in the core, respectively, and x_{CO_2i} and x_{CO_2} are the initial and current CO₂ mole fractions in the liquid phase, respectively. The component and the total molar oil recoveries based on the component moles are given by

$$RF_{comp} = 1 - \frac{n_k}{n_{ki}} \dots\dots\dots(4.3)$$

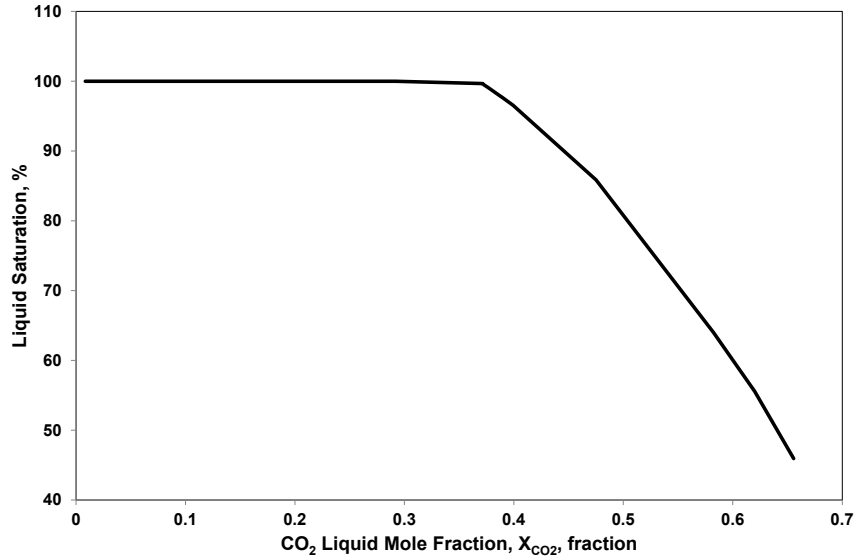


Figure 4.11 – Calculated liquid saturation versus CO₂ liquid mole fraction from constant pressure (300 bara) and temperature (130 °C) swelling test.

$$RF_{mole} = 1 - \frac{\sum_{\substack{k=N2 \\ k \neq CO2}}^{C35+} n_k}{\sum_{\substack{k=N2 \\ k \neq CO2}}^{C35+} n_{ki}} \dots\dots\dots (4.4)$$

where n_{ki} and n_k are the initial and current moles of component k . The total oil recovery was based on the component mass, as calculated by:

$$RF_{mass} = 1 - \frac{\sum_{\substack{k=N2 \\ k \neq CO2}}^{C35+} m_k}{\sum_{\substack{k=N2 \\ k \neq CO2}}^{C35+} m_{ki}} \dots\dots\dots (4.5)$$

where m_{ki} and m_k are the initial and current masses of component k .

The oil recoveries that were calculated using the above equations are shown in Fig. 4.12. The oil saturation and mole-based recoveries were similar and gave similar ultimate recoveries (at 22 days) of approximately 95%. The mass-based recovery led to a lower recovery (76%) because the heavy components were

recovered more slowly than the light and medium components, as shown in **Figs. 4.13** and **4.14**. For consistency, the mole-based oil recovery is considered to be the oil recovery factor from this point forward.

The numerical models were performed using two sets of core relative permeabilities. The mole-based recovery factors for these two models were similar and overlapped each other (**Fig. 4.15**). A model using 5 D fracture permeability was evaluated to understand the effects of actual fracture permeability reduction on the experimental result. As seen in Fig. 4.15, oil recovery was close to the 80 md cases, which indicates that the viscous force had a minor impact on the recovery mechanism. One additional model, in which the diffusion option was turned off, was constructed to observe the effects of diffusion on the experiment. The oil recovery was slower, and the ultimate oil recovery (at 22 days) was reduced to 76 %.

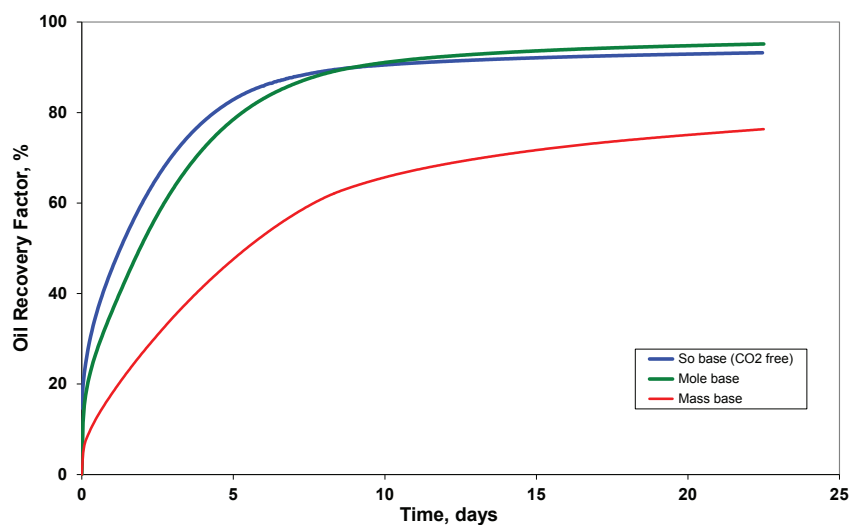


Figure 4.12 – Calculated oil recovery factor based on mole, mass and oil saturation from matched model with linear core relative permeability.

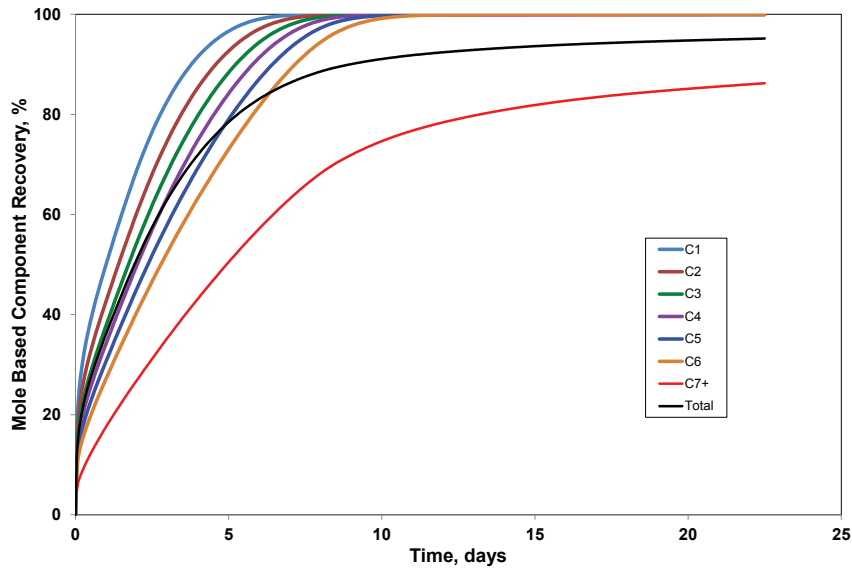


Figure 4.13 – Calculated mole based oil recovery of light and intermediate components from matched model with linear core relative permeability.

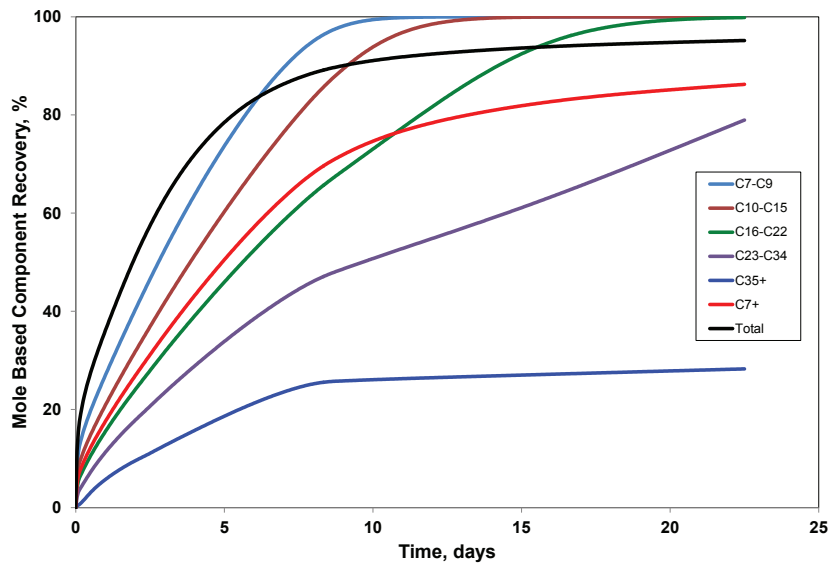


Figure 4.14 – Calculated mole based oil recovery of heavy components from matched model with linear core relative permeability.

Figs. 4.13 and 4.14 show that lighter components were produced first, which indicates that CO₂ preferentially vaporizes the light and intermediate components. These components are transported out of the matrix block by molecular diffusion, as fresh CO₂ enters the fracture (annular space) and the area behind the front of the displacement. During the early production period, a front develops from the fracture inwards caused by CO₂ entry through gravity and mass transfer as shown in Fig. 4.16. After the light components were vaporized (5 days), the gravity-drainage process appeared to be more pronounced, with less lateral displacement compared to the early period of the experiment (Fig. 4.17).

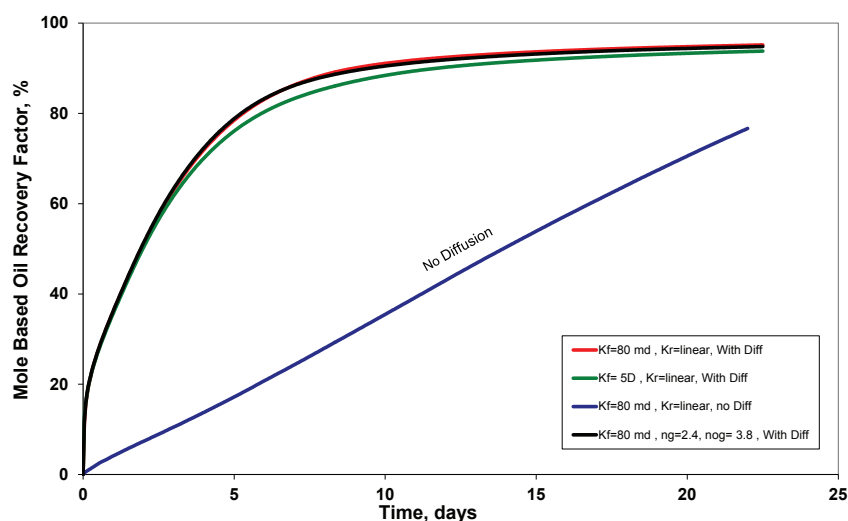


Figure 4.15 – Mole based oil recovery results from numerical sensitivity models at 30 °C separator temperature.

4.7 Conclusions

The following conclusions were determined after analyzing the experiment and the numerical studies.

1. The measured production data from the experiment were matched with a commercial compositional, finite-difference simulator model.
2. Mass transfer (vaporization, condensation and molecular diffusion) was the dominant production mechanism during the early stages of the

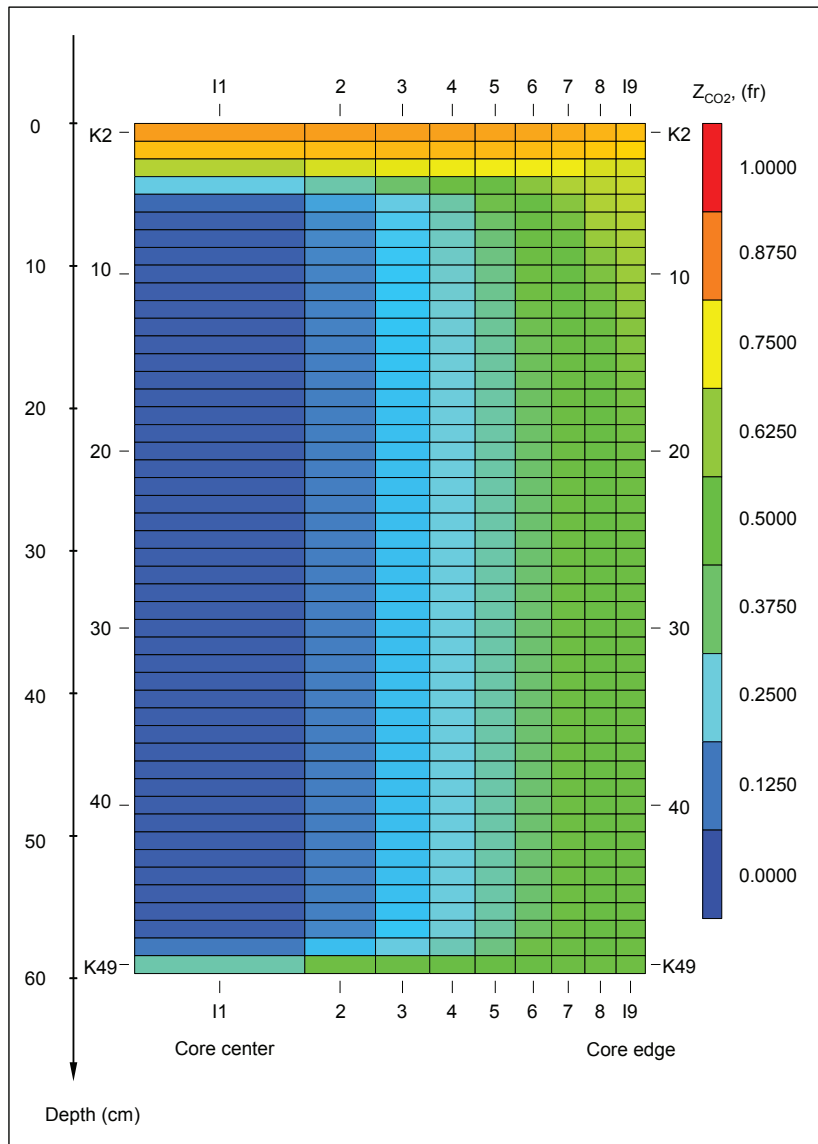


Figure 4.16 – CO₂ mole fraction profile of core after 12 hours for matched model with linear core relative permeability (at about 36% oil recovery).

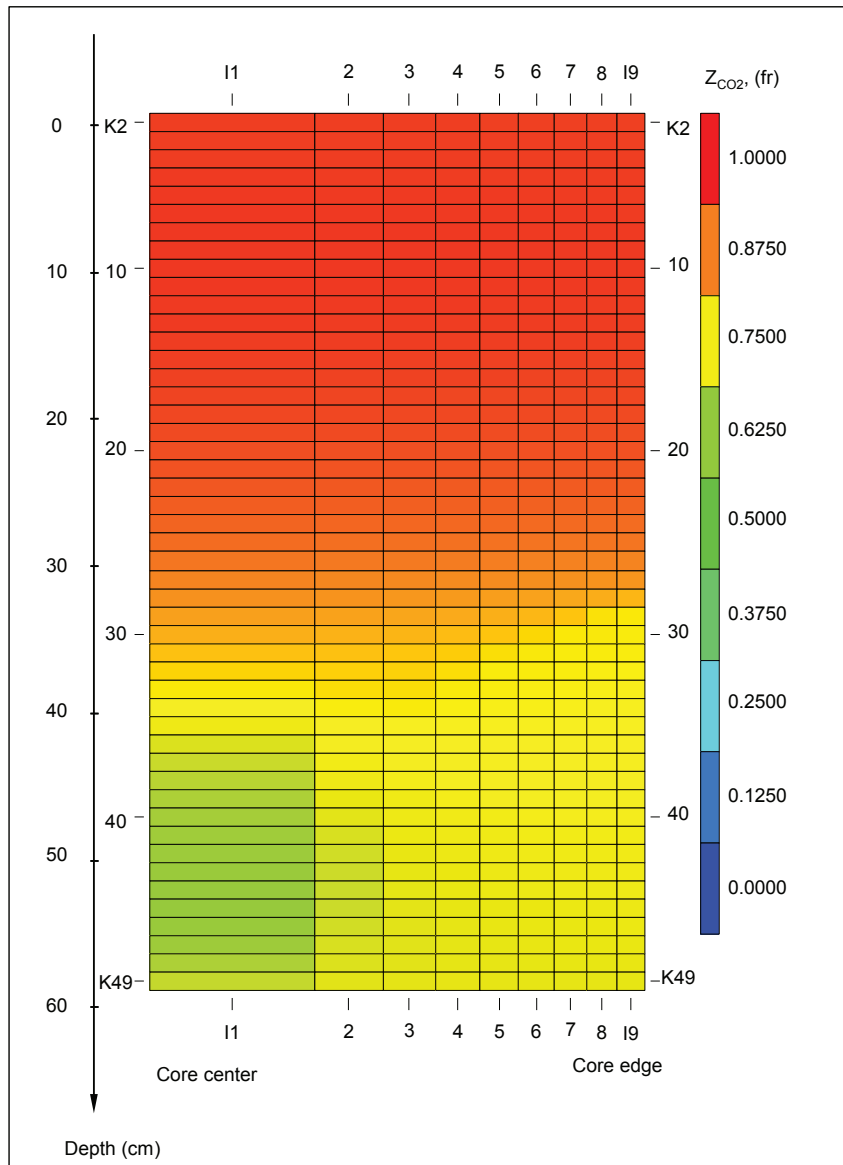


Figure 4.17 – CO₂ mole fraction profile of core after 5 days for matched model with linear core relative permeability (at about 79% oil recovery).

experiment, in which the gravity drainage became more pronounced after the light components were recovered.

3. The fractured permeability level that resulted from the remaining sealing material after core initialization did not affect the experiment results.
4. The high recoveries that were observed did not appear to be related to the pressure exceeding the minimum miscibility pressure.

4.8 Reference

- Christoffersen, K. 1992. High-Pressure Experiments with Application to Naturally Fractured Chalk Reservoirs. PhD Dissertation, NTNU, Trondheim, Norway.
- Darvish, G.R. 2007. Physical Effects Controlling Mass Transfer in Matrix Fracture system During CO₂ Injection in to Chalk Fractured Reservoir. PhD Dissertation, NTNU, Trondheim, Norway.
- Darvish, G.R., Lindeberg, E., Holt, T., Utne, S.A. and Kleppe, J. 2006. Reservoir Conditions Laboratory Experiments of CO₂ Injection into Fractured Cores. Paper SPE 99650 presented at the 2006 SPE Europec/EAEG Annual Technical Conference and Exhibition, Vienna, Austria, 12-15 June.
- Moortgat, J., Firoozabadi, A. and Farshi M.M., 2009. A New Approach to Compositional Modeling of CO₂ Injection in fractured Media Compared to Experimental Data. Paper SPE 124918 presented at the 2009 SPE Annual Technical Conference and Exhibition, New Orleans, Louisiana, U.S.A., 4-7 October.
- Petrostreamz AS: *Pipe-It/Streamz*, www.petrostreamz.com.
- Schlumberger: *ECLIPSE 300* Reservoir Engineering Software. 2009. www.slb.com.
- Zick Technologies: *PhazeComp*. www.zicktech.com.

Chapter 5

Modeling CO₂ Injection in Darvish Fractured Chalk Experiment (Sw=26%)

5.1 Introduction

In this chapter, we modeled an additional Darvish (2007) CO₂ injection experiment, in which there was initial water saturation in the core, and the CO₂ was injected at a higher rate. The experiment consisted of a vertically-oriented, 60-cm-long chalk outcrop core that was initially saturated with live reservoir oil at a temperature of 130 °C and a pressure of 300 bar. After saturating the core with the oil and water by displacement, a small fracture volume surrounding the core was created by heating the solid Wood's metal that originally filled the space between the core and core holder. The CO₂ was then injected for 20 days. Our modeling was conducted using a compositional reservoir simulator. The 2-dimensional r-z model used a fine grid for the core and the surrounding fracture. The CO₂ injection rate and initial water saturation effect were investigated by comparing these experimental results with those of a similar experiment in which the CO₂ was injected at a lower rate with no initial water saturation (Chapter 4).

Pollack *et al.* (1988) experimentally studied the effect of the presence of an aqueous phase on the phase behavior of a CO₂/hydrocarbon system. They found that the presence of water reduces the amount of CO₂ that is available for mixing with the hydrocarbon due to the solubility of CO₂ in water. Chang, Coats and

Nolen (1998) modeled CO₂ floods, including CO₂-water solubility, for an unfractured reservoir. These authors studied secondary and tertiary water alternating gas (WAG) injection. They found that approximately 10% of the CO₂ that was injected dissolved in to the water, and this CO₂ was unavailable for mixing with the oil. The solubility effects were more pronounced for tertiary CO₂ WAG than for the secondary injection and the delayed oil recovery. We studied CO₂ solubility in water, as described in the following sections.

5.2 Rock and Fluid Properties

A chalk core from the Faxe area outcrop in Denmark, which has similar rock properties to North Sea chalk, was used in the present experiment. The core had a cylindrical shape with a length of 59.6 cm and a diameter of 4.6 cm. The core porosity and permeability have been previously reported as 44.4% and 4 md, respectively (Darvish 2007).

Relative permeabilities and capillary pressure were not measured for the core. The C₁-n-C₅ capillary pressure of the Faxe outcrop chalk core, as measured by Christoffersen (1992), was used for the core oil-gas capillary pressure. Corey-type relative permeabilities were used to model the experiment. The gas and oil exponents for the Corey-like relative permeabilities (k_{rg} and k_{rog}) were 2.4 and 3.8, respectively (Eqs. (2.19) and (2.20)). The oil and gas relative permeabilities are shown in **Fig. 5.1**. For the water and oil relative permeabilities, the same type of relative permeabilities (Eqs. (2.17) and (2.18)) were used. The oil exponent for the Corey-like relative permeability (k_{row}) was set to 2.5. The water-oil capillary pressure curve (Eq. (2.21)) and the water permeability were set as variables to match the cumulative volume of water produced. **Fig. 5.2** shows the oil and water relative permeabilities that were used in the present model.

The 13 components PR-EOS/LBC parameters that were used in this chapter are given in Tables 4.1 and 4.2.

5.3 Experimental Procedures

This section describes the experiment that was performed to study a CO₂

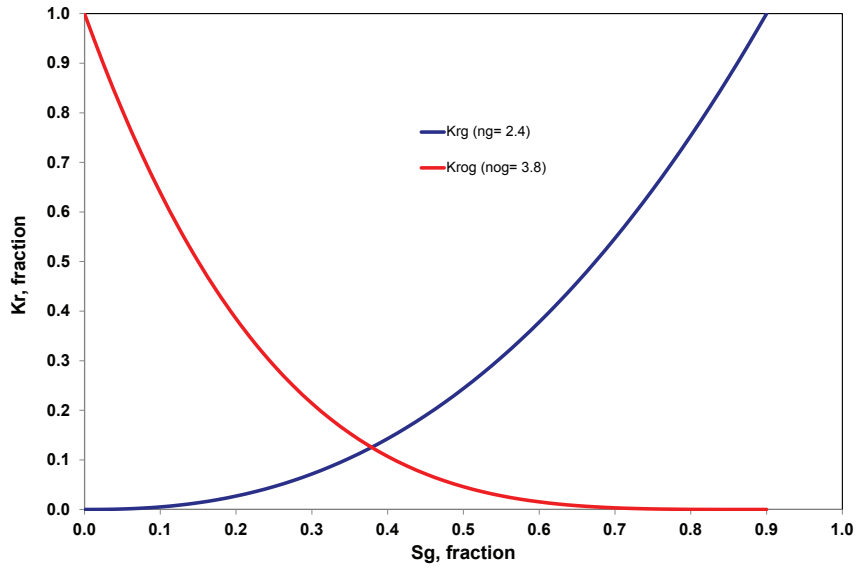


Figure 5.1 – Oil and gas relative permeability used in the matched model.

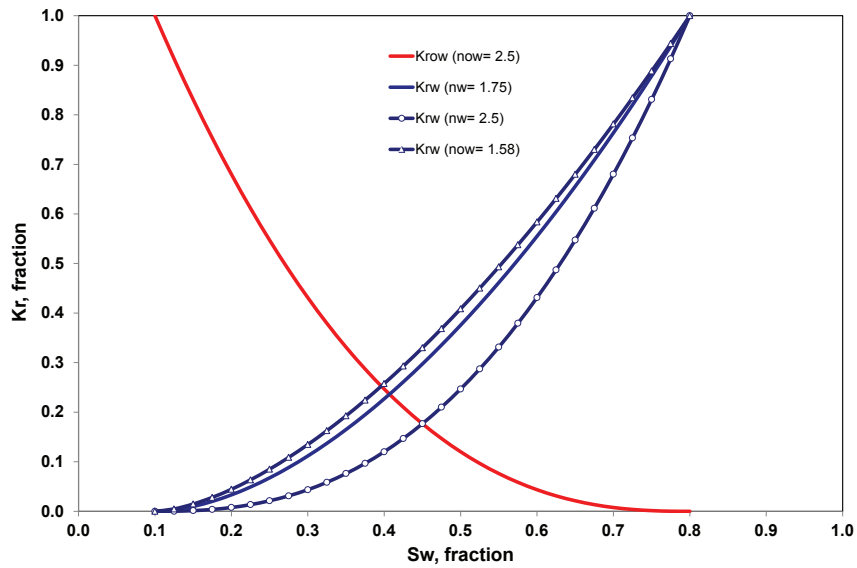


Figure 5.2 – Oil and water relative permeability used in the matched model.

injection in a fractured reservoir. The experimental procedure that is described was based on Darvish (2007) and on personal communications with Darvish.

A dried cylindrical chalk core was placed in a steel core holder. The core holder inner diameter was 5.0 cm. The core diameter was 4.6 cm, and the length was 59.6 cm. The fracture was represented by a 2 mm space between the core and the core holder. The core porosity and absolute permeability have been previously reported as 44.4% and 4 md, respectively (Darvish 2007).

Due to the large permeability contrast between the core and the surrounding space (artificial fracture), the process of initially saturating the core with live oil was complicated. The oil would flow through the high permeable space, leaving the core partially saturated with live oil. Therefore, the space between the core and the core holder wall was initially filled with Wood's metal. The metal melting point was 70 °C, and the experiment was performed at 130 °C. The metal was melted and poured into the space between the core and the core holder. The fracture was sealed with the metal and had zero permeability after the system was cooled.

The core was evacuated and pressurized with brine. Live oil was injected from in the top of the core at a constant pressure (300 bar) and temperature (40 °C), and the amount of water produced was measured. The water saturation of the core after flooding it with a 1.2 pore volume of oil was 26.3 %. The system was heated to 130 °C at a constant pressure (300 bar), and the Wood's metal was removed from the annular space by injecting oil. The oil was injected from the top of the core holder, and the metal was drained from the bottom. The fracture porosity and permeability were not measured after the metal was removed from the system; however, the pressure difference between the top and bottom of core holder was measured, which could be used to determine the fracture permeability in a model.

The oil in the fracture was replaced by CO₂. The experiment continued with a CO₂ gas injection for 20 days. The cumulative volume of CO₂ that was injected during the experiment is illustrated in **Fig. 5.3**. The fluid that was produced was

diverted to a separator under ambient conditions. The mass of the separated oil was measured continually, and the component mass fraction was measured periodically.

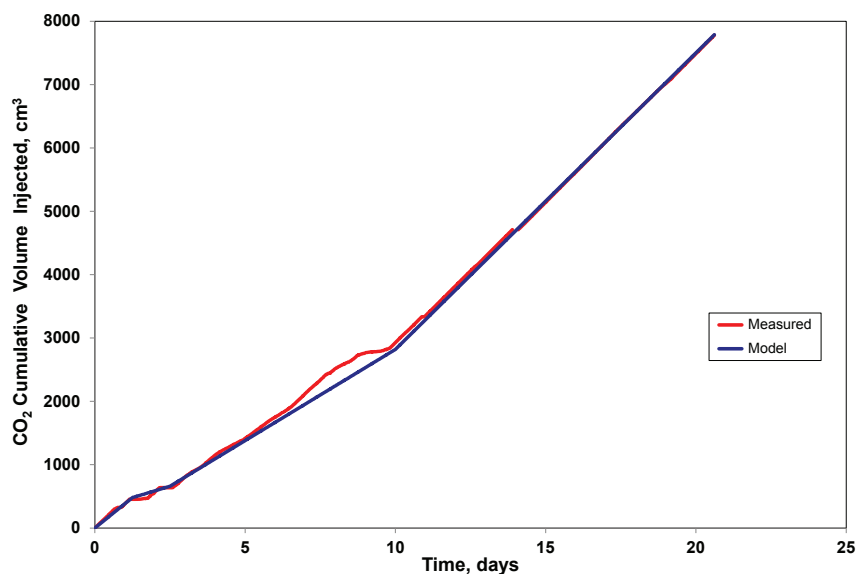


Figure 5.3 – Measured and calculated cumulative volume of CO₂ injected.

5.4 Model Description

The matrix block (core) was initially filled with oil, and the fractures were initially filled with CO₂. The fractures were assumed to have a negligible capillary pressure. The matrix and the fracture dimensions were the same as the core and fracture in the experiment. A two-dimensional, radial grid was used in which the matrix block was surrounded by two horizontal fractures (at the top and bottom) and one vertical fracture. A fine grid was required to reduce the numerical dispersion for the CO₂ gas injection. 10 and 51 grid cells were used in the radial and vertical directions, respectively, to simulate the experiment.

The *ECLIPSE 300* simulator with implicit solution method was used for all of the simulations. A 13-component PR-EOS was used. The EOS properties of the components are summarized in Tables 4.1 and 4.2.

The oil and gas relative permeabilities that were used to model the experiment are shown in Fig. 5.1. As mentioned above, the water-oil capillary pressure curve and water relative permeability were set as variables to match the cumulative volume of water that was produced. Because mobile oil, gas and water were used in the model, three-phase oil relative permeabilities were needed. Eqs. (2.23a) and (2.23b) were used.

The C_1 - n - C_5 capillary pressure that was measured by Christoffersen (1992) for a similar core was used as the core capillary pressure in the model. Following Eq. (2.24), this capillary pressure was scaled using the IFT, for which the reference interfacial tension (IFT) was 1.5 mN/m. No capillary pressure was present in the fracture. The relative permeabilities were not scaled using the IFT.

The *Pipe-it/Streamz* software was used to calculate cumulative mass of produced oil from reservoir simulation result. One separator was defined to simulate the produced stream in the experiment. As in the experiment, the separator pressure was atmospheric. As mentioned above, the separator temperature was not measured during the experiment.

The oil and gas effective diffusion coefficients are given in Table 4.4. The gas diffusion coefficients were determined from the equilibrium gas at the bubble-point pressure. More details of the diffusion coefficient calculations are given in section (2.2).

5.5 Matching The Experimental Data

In this section, we describe the matching process for the measured cumulative mass of the separator oil and the cumulative volume of the water that was produced. In Chapter 4, fractured permeability was set to 80 md to get pressure difference measured during the experiment. Because the same procedure was used to initialize this experiment, we kept the fracture permeability at 80 md. A CO_2 injection experiment (Darvish 2007) using a chalk core without water saturation was matched with the two sets of the oil-gas relative permeabilities (Chapter 4). When water was present in the system, however, we found that the

non-linear oil-gas relative permeabilities for the core provided a better match than the linear gas-oil relative permeabilities.

The model matched the cumulative volume of produced water with and without the water-oil capillary pressure. Because the water-oil capillary pressure was not measured, we used the water-oil imbibition capillary pressure measurements from the other North Sea chalk reservoir (Valhall) as guidelines (Webb, Black and Tjetland 2005). The Valhall water-oil imbibition capillary curve was not used in the model, but the capillary curve that was used in the model had a similar capillary pressure range, as is shown in **Fig. 5.4**. The water exponent (n_w) for the Corey-like water relative permeability (K_{rw}) was set as a variable in both cases (with and without the water-oil capillary pressure). The cumulative volume of the gas that was produced was matched, yielding $n_w = 1.58$ with, and $n_w = 1.75$ without, the water-oil capillary pressure.

No condenser or cooler was present in the outlet stream; consequently, the effective separator temperature was set as a variable during the experiment. The effective surface separator temperature was mainly affected by the producing

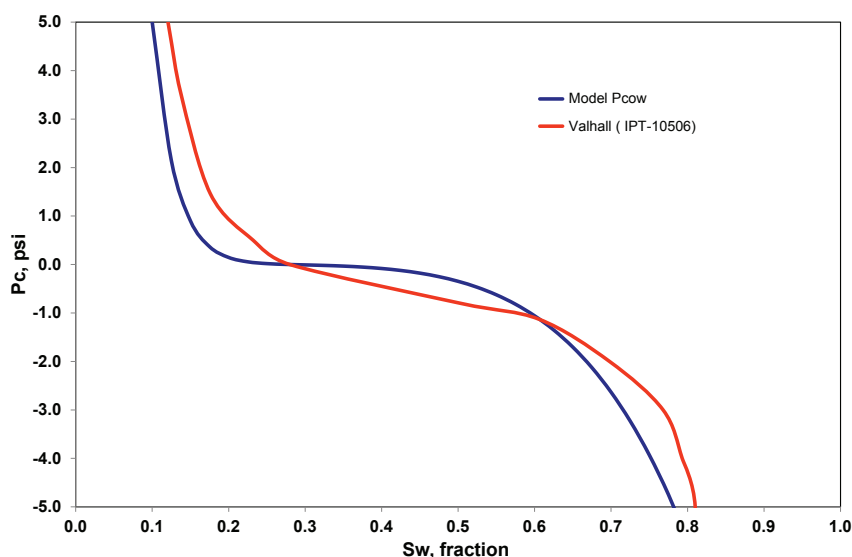


Figure 5.4 – Model and Valhall (after Webb et. al.) capillary pressure curves.

stream rate and the solid precipitation on the pipe wall (Wood's metal and wax). The fluid retention time decreased with an increasing fluid rate in the pipe, and as a result, the amount of heat exchange was smaller. In contrast, the stream rate was directly proportional to the CO₂ injection rate. The profiles of the CO₂ injection rate and the effective surface separator temperature are shown in **Figs. 5.5** and **5.6**, respectively. Except in the early stages (less than 1.3 days) of the experiment, the effective separator temperature was proportional to the injection rate. As mentioned above, the solid precipitation on the pipe wall reduced the heat exchange between the fluid and the pipe. Therefore, the heat exchange at the early stages of the experiment were higher than those in the later stages because of less solid precipitate on the pipe wall.

The other parameters in the numerical model were taken from the reported values in the experiment. The results of the model are shown in **Figs. 5.7** and **5.8**.

The heavy-component mass fractions from the experiment were compared with the numerical model results. All of the calculated mass fractions from the model follow the same trend as the measured values, as shown in **Fig. 5.9**. The

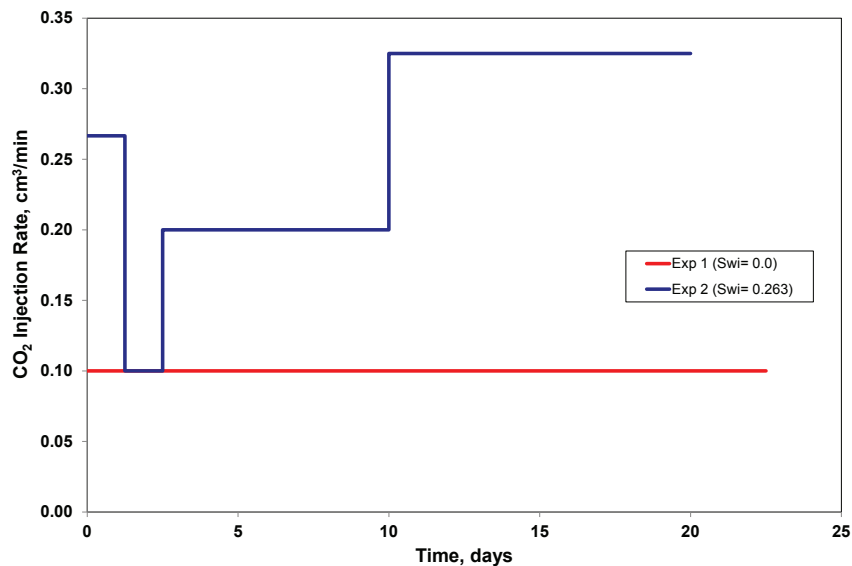


Figure 5.5 – Profile of CO₂ injection rate in experiment-1 ($S_w=0.0$) and experiment-2 ($S_w=0.263$).

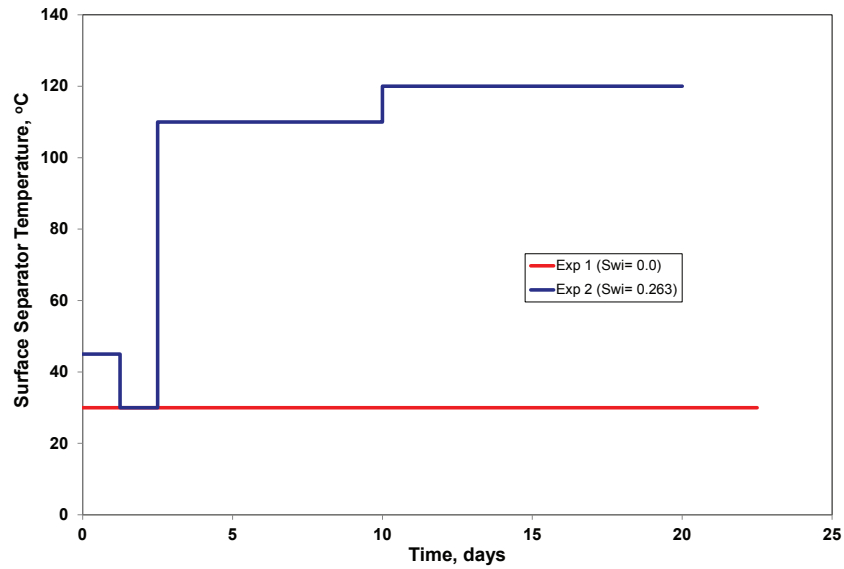


Figure 5.6 – Profile of separator temperature in experiment-1 ($S_w=0.0$) and experiment-2 ($S_w=0.263$).

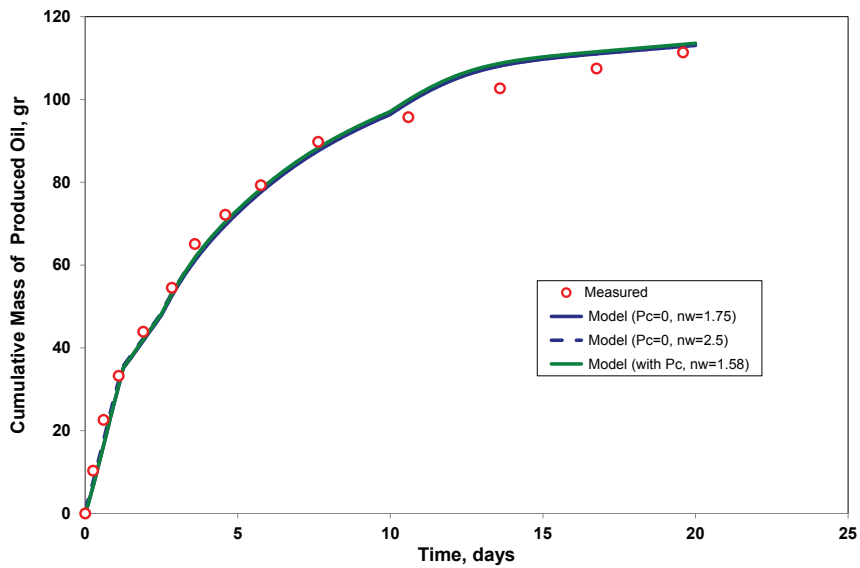


Figure 5.7 – Measured produced oil mass with matched simulation results for three core water relative permeability and with and without water-oil capillary pressure.

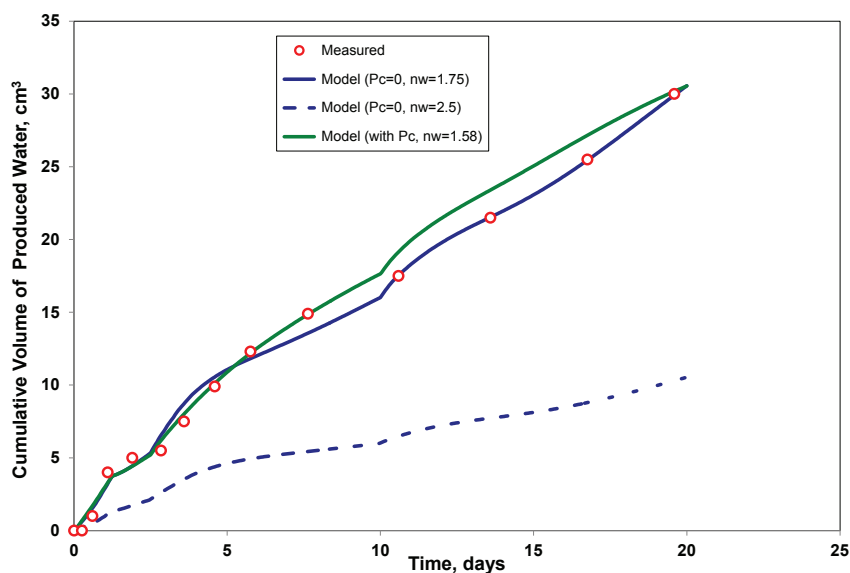


Figure 5.8 – Measured produced water volume with matched simulation results for three core water relative permeability and with and without water-oil capillary pressure.

separator temperature was set to 30 °C for this calculation because the small samples that were taken from the oil stream cooled faster and quickly reached laboratory temperature. When C_{10} and the heavier components were grouped together, the results of the numerical model and the experimental data were closer together than when they were not grouped, as shown in Fig. 5.9. This result likely indicates that the grouping of the C_{10+} components was performed somewhat differently in the laboratory than in the EOS calculation. The calculated molecular weight of the oil produced in the laboratory was compared with the molecular weight from the numerical model (**Fig. 5.10**). The calculated molecular weight was close to that in the laboratory until 8 days had elapsed. After 8 days, the molecular weight of the numerical model was lower than the calculated molecular weight of produced oil in the laboratory, possibly due to the uncertainty of determining the molecular weight of heavy-end components in the laboratory. The oil produced after 8 days mainly consisted of the C_{16+} . C_{23+} mass

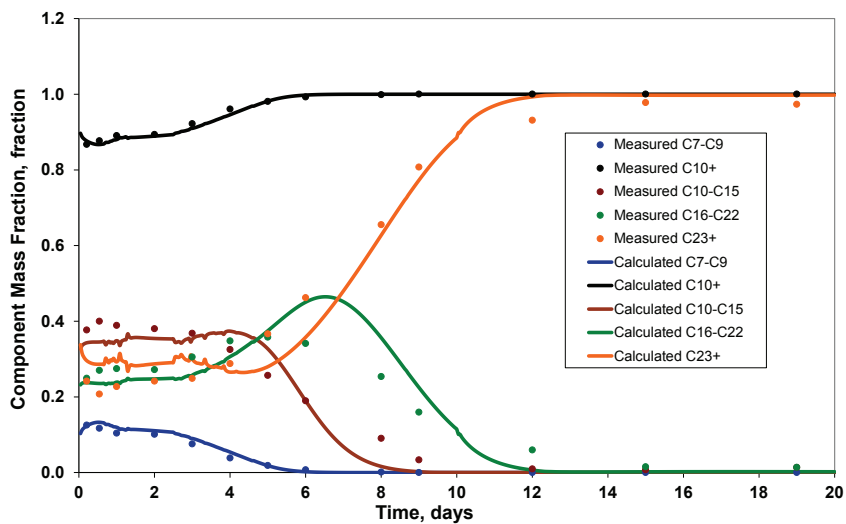


Figure 5.9 – Measured and calculated heavy components mass fraction of produced oil at separator condition.

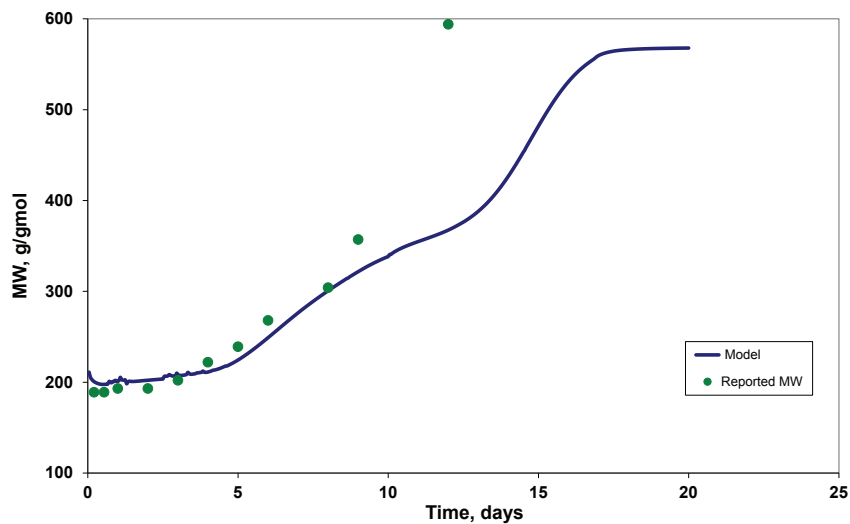


Figure 5.10 – Reported and calculated molecular weight of produced oil at separator condition.

fractions increased with time. As a result, the difference between the two molecular weights also increased with time.

5.6 CO₂ Injection Rate Effect

In this section, we describe the comparison of the modeling results from the present experiment with those of the experiment in Chapter 4. In the experiment in Chapter 4, the CO₂ injection rate (0.1 cm³/min) was lower than that in the present study, and no initial water was present in the system. We will call the experiment that is described in this chapter “Experiment-2”, and we will call the experiment from Chapter 4 “Experiment-1”. Some of the CO₂ was dissolved in the water and was consequently not available to interact with the oil. Based on the results of Duan and Sun (2003), 11.5 cm³ of CO₂ dissolved in the core water in place (116 gr). Therefore, the amount of CO₂ that dissolved into the water was considered to be negligible compared to the 7500 cm³ of CO₂ that was injected over the 20 day period.

5.6.1 Oil Recovery

The components and the total oil recovery that were based on the component moles were calculated using Eqs. (4.3) and (4.4). Plotting the mole-based oil recovery in both of the experiments using the model results (**Fig. 5.11**) revealed that the experiment with the lower CO₂ injection rate had better efficiency per CO₂ hydrocarbon pore volume (HCPV) injected. The oil that was produced in Experiment-1 (the experiment with the lower CO₂ injection rate) was heavier than that in Experiment-2 with respect to the HCPV injected (**Fig. 5.12**). In both of these experiments, furthermore, the lighter components were produced first, as shown in **Fig. 5.13**. Consequently, the mass transfer between the CO₂ and the hydrocarbon was more efficient in Experiment-1 than in Experiment-2. Because greater amounts of CO₂ were available to interact with the oil in the core in Experiment-2, however, the oil recovered faster when the CO₂ injection rate was increased, as shown in **Fig. 5.14**. Although CO₂ and oil had less efficient mass transfer but more oil was recovered during same period of time.

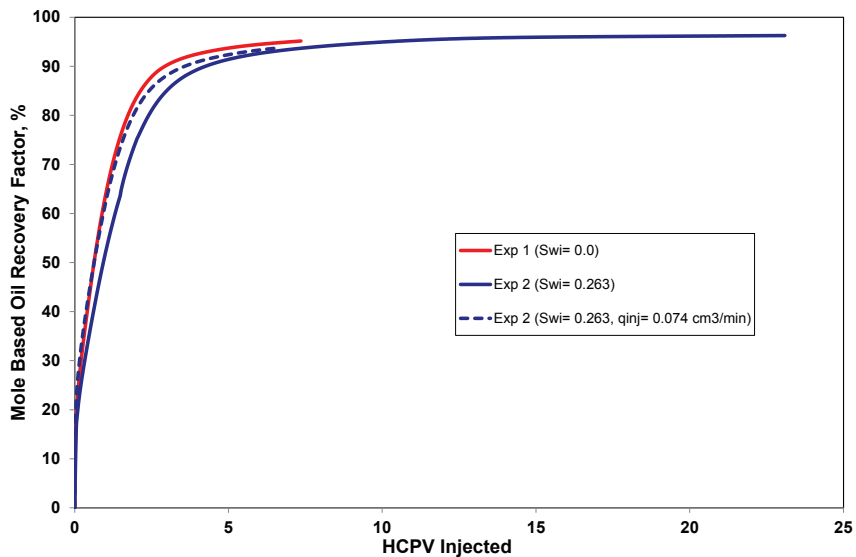


Figure 5.11 – Calculated mole based oil recovery factor of two experiments versus HCPV injected from matched model.

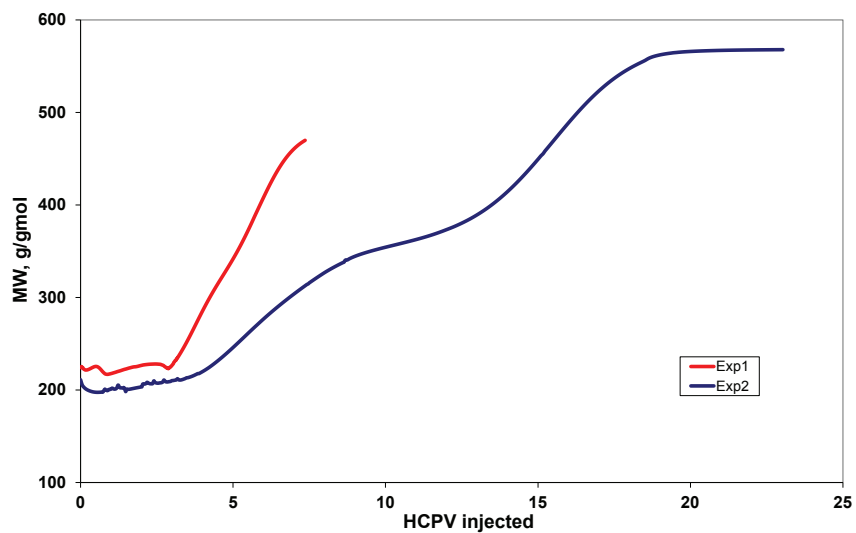


Figure 5.12 – Calculated mole based component recovery of two experiments versus HCPV injected from matched model.

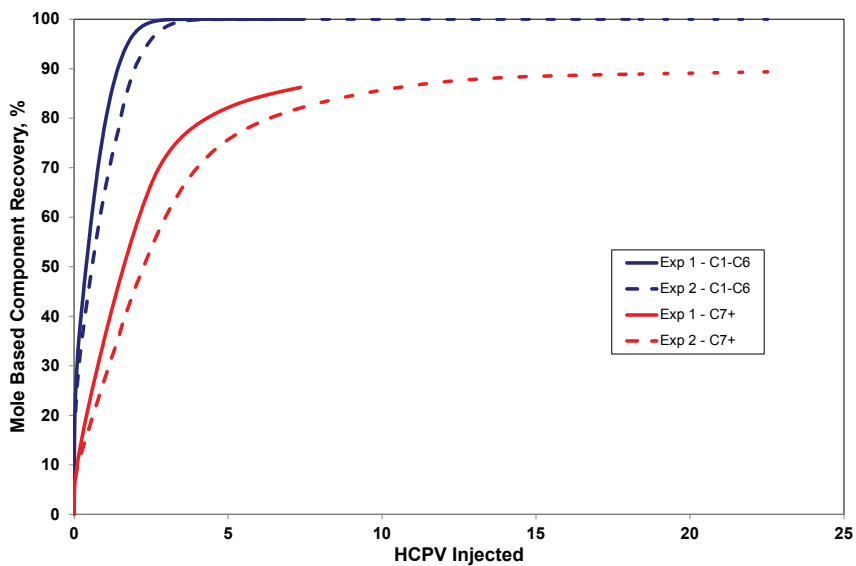


Figure 5.13 – Calculated mole based component recovery of two experiments versus HCPV injected from matched model.

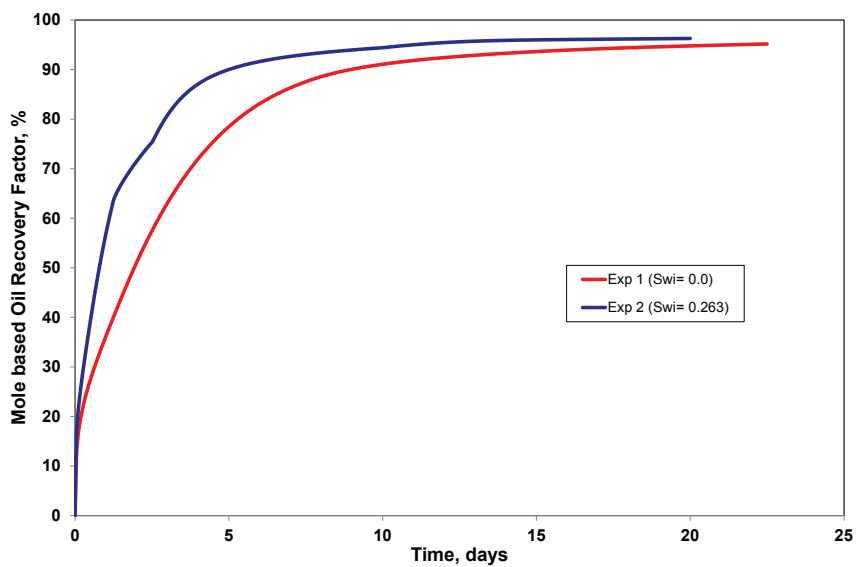


Figure 5.14 – Calculated mole based oil recovery factor of two experiments versus time from matched model.

Injection rate in Experiment-2 model was reduced to 0.074 cm³/min to yield the same HCPV fraction injected as in Experiment-1. Results of this Experiment-2 run shows that recovery with and without water is approximately same at a given HCPV injected, when the CO₂ injection rate, expressed as $\Delta\text{HCPV}/\Delta t$, is approximately same (Fig. 5.11).

5.6.2 CO₂ Map Profile

Comparing the CO₂ map profiles from the two experiments yielded 27.5 and 78.5 % oil recovery. These results correspond to 12 hours and 5 days in Experiment-1, respectively, and to 5 hours and 2.8 days in Experiment-2, respectively. As shown in **Figs. 5.15** and **5.16**, the oil was displaced more laterally in Experiment-2 than in Experiment-1. The amount of CO₂ that flowed in the fracture (the annulus space) was greater in Experiment-2 than in Experiment-1. Therefore, the mass transfer was greater in the core grids that were adjacent to the fracture compared to the central core grids.

5.7 Grid Sensitivity

A numerical grid sensitivity analysis was performed to investigate its effect on oil recovery and water production. The ultimate oil recovery was the same for all of the grids considered, as shown in **Fig. 5.17**. However, the 5x5 (N_xxN_z) grid resulted in a slightly slower oil recovery. The amount of water that was produced decreased as the number of grid cells that were used in the model decreased. The 5x5 grid model does not follow the production trend of the other cases (**Fig. 5.18**).

5.8 Diffusion Coefficients Effect

Diffusion played an important role in the present experiment. The oil and gas diffusion coefficients were the parameters that controlled the diffusion mechanisms in the numerical simulation. Another important parameter was the driving force of the diffusion transport. Two major forces drive diffusion: a) concentration forces and b) chemical forces. The driving potential from the chemical force was used in all of the above models.

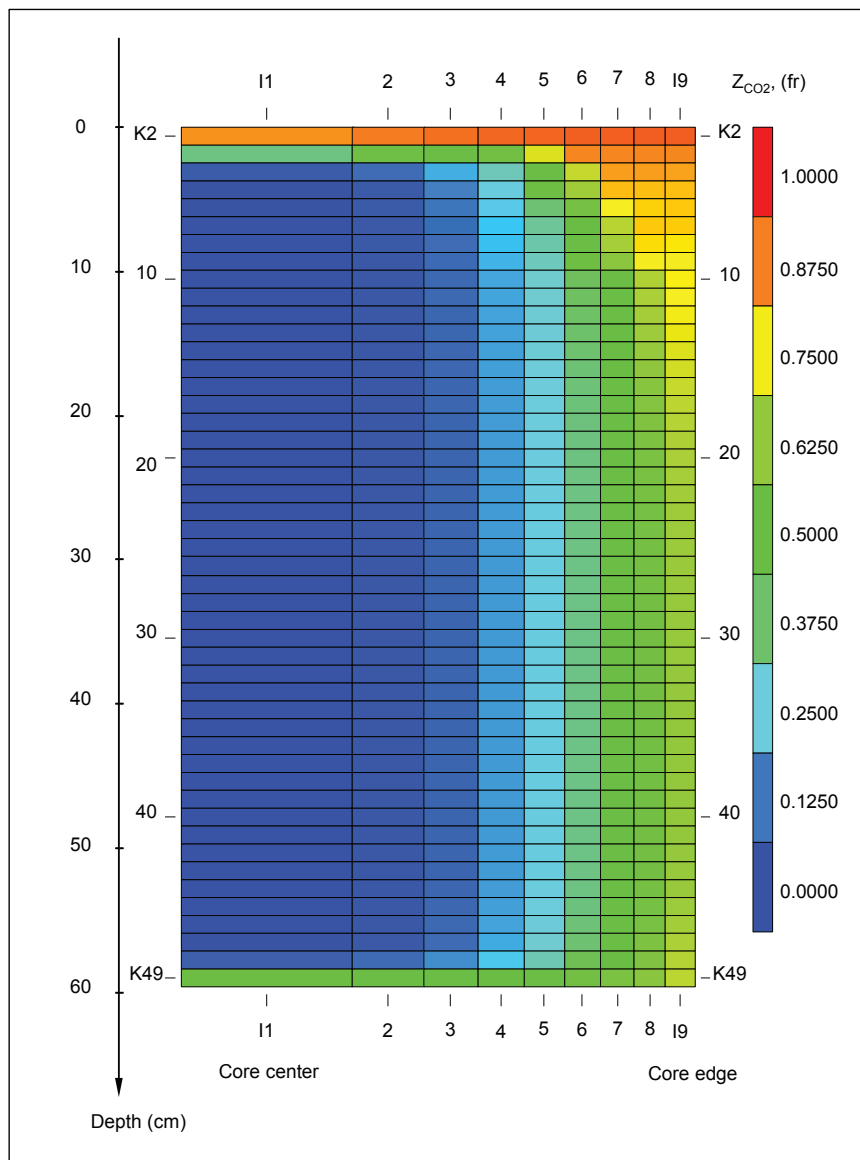


Figure 5.15 – CO₂ mole fraction profile of core after 5 hours for matched model of experiment-2 (at about 36% oil recovery).

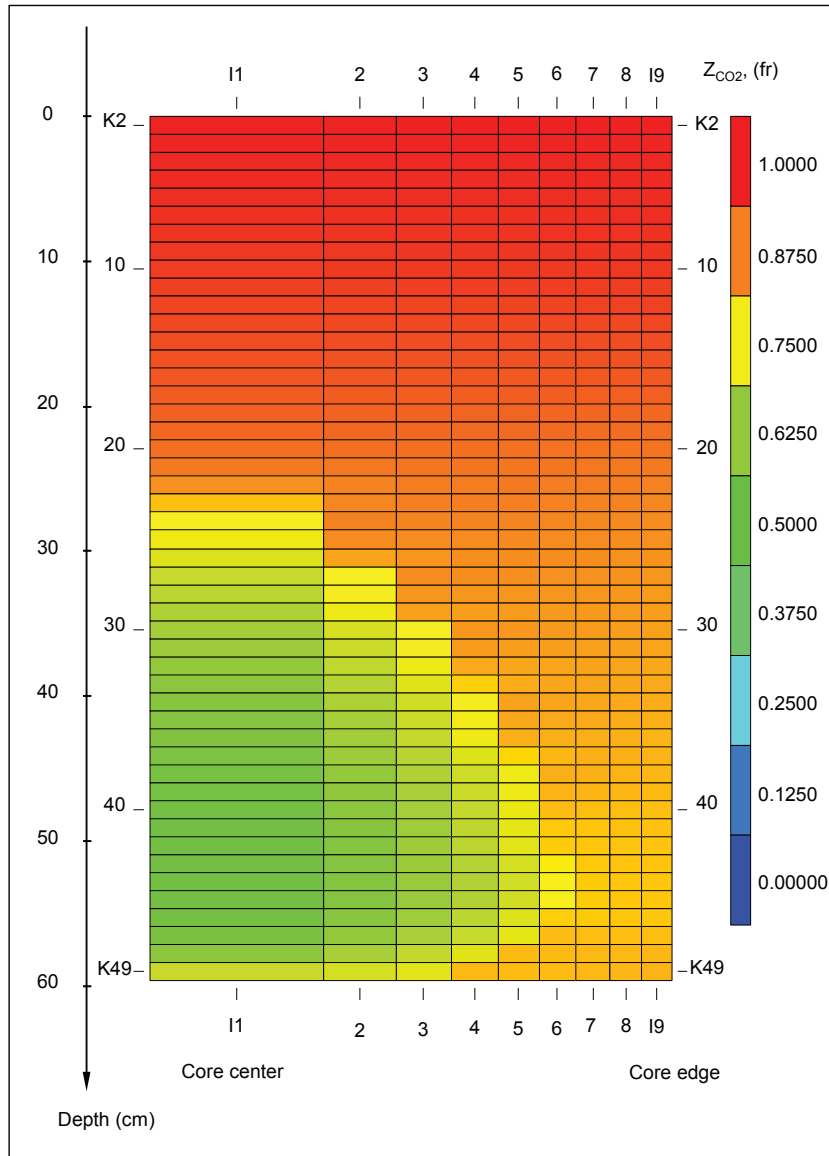


Figure 5.16 – CO₂ mole fraction profile of core after 2.8 days for matched model of experiment-2 (at about 78.5% oil recovery).

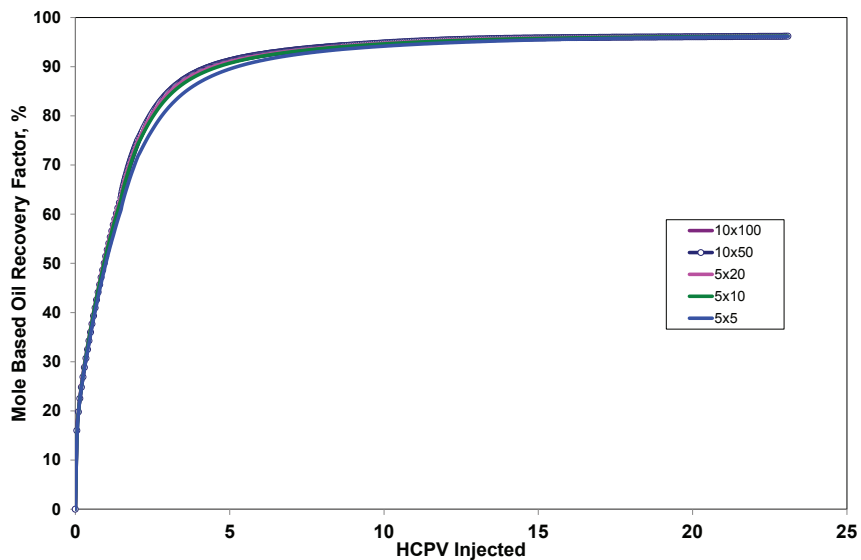


Figure 5.17 – Mole based oil recovery results from grid sensitivity models.

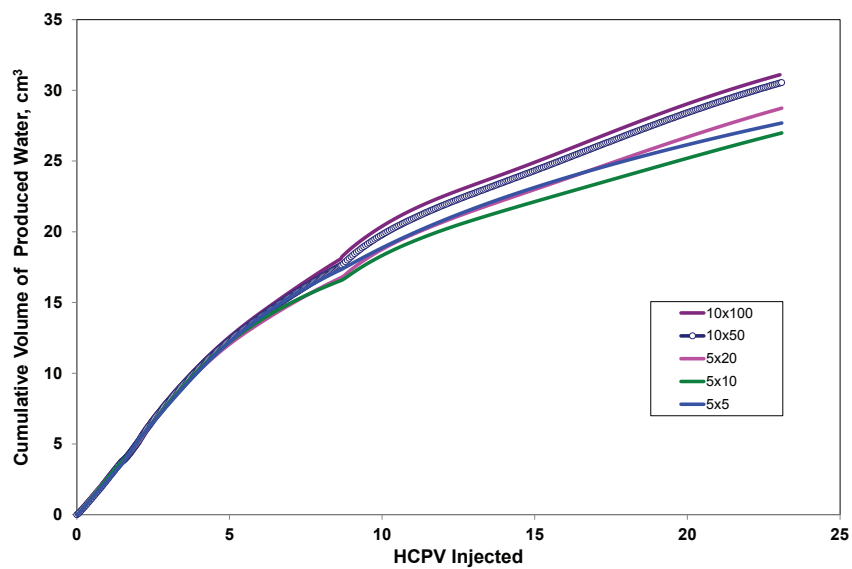


Figure 5.18 – Mole based oil recovery results from numerical sensitivity models.

The oil and gas diffusion coefficients were increased and decreased by one order of magnitude to study the effects of these adjustments on the oil recovery. As expected, increasing the diffusion coefficients increased the oil recovery rate and decreased the diffusion coefficients, which slowed down the oil recovery (Fig. 5.19). One model was constructed using the default oil and gas diffusion coefficients using concentration driven diffusion. The oil recovery was dramatically slower than in the other cases for which chemical potential driven diffusion was used. The ultimate oil recoveries were the same for all of the cases (Fig. 5.19).

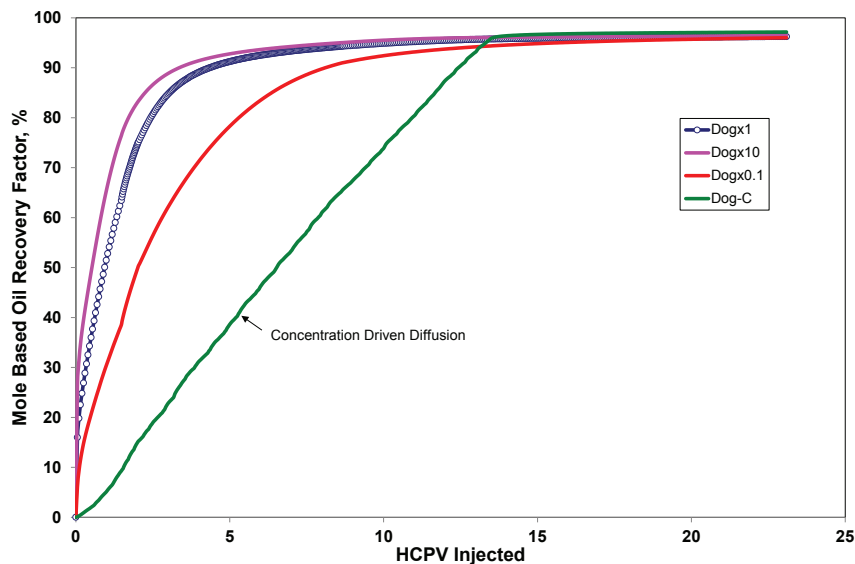


Figure 5.19 – Effect of diffusion coefficient and diffusion drive on mole based oil recovery factor.

5.9 Conclusions

The following conclusions were determined after analyzing the experimental and numerical studies.

1. The measured production data from the experiment were matched with a commercial compositional finite-difference simulator model.

2. The ultimate oil recovery was not significantly affected by the CO₂ injection rate. The rate of oil recovery increased with an increasing CO₂ injection rate in the time domain; however, the mass transfer became less efficient with respect to the CO₂ volume that was injected.
3. The initial water saturation in this experiment did not appear to affect the oil recovery.
4. The oil recovery was sensitive to the diffusion coefficients that were used in the modeling. Traditional concentration-based diffusion severely under-predicts the diffusion compared to the chemical-energy-based diffusion.
5. The oil recovery was less sensitive to numerical gridding than the water production.

5.10 References

- Chang, Y., Coats B.K and Nolen, J.S. 1998. A Compositional Model for CO₂ Floods Including CO₂ Solubility in Water. SPE Reservoir Evaluation and Engineering, 1(2): 155-160. SPE-35164-PA.
- Christoffersen, K. 1992. High-Pressure Experiments with Application to Naturally Fractured Chalk Reservoirs. PhD Dissertation, NTNU, Trondheim, Norway.
- Darvish, G.R. 2007. Physical Effects Controlling Mass Transfer in Matrix Fracture system During CO₂ Injection in to Chalk Fractured Reservoir. PhD Dissertation, NTNU, Trondheim, Norway.
- Duan, Z. and Sun, R., 2003. An Improved Model Calculating CO₂ Solubility in Pure Water and Aqueous NaCl Solution from 273 to 533 K and from 0 to 2000 bar. Chemical Geology Journal 193 (2003) 257– 271.
- Petrostreamz AS: *Pipe-It/Streamz*, www.petrostreamz.com.
- Pollack N.R., Enick R.M., Mangone D.J. and Morsi B.I. 1988. Effect of an Aqueous Phase on CO₂/Tetradecane and CO₂/Maljamar-Crude-Oil Systems. SPE Reservoir Engineering 3(2) : 533-541. SPE-15400-PA.

Schlumberger: *ECLIPSE 300* Reservoir Engineering Software. 2009.
www.slb.com.

Webb, K.J., Black, C.J.J. and Tjetland. G., 2005. A Laboratory Study Investigating Methods for Improving Oil Recovery in Carbonates. International Petroleum Technology Conference, Doha, Qatar, 21-23 November.

Chapter 6

CO₂ Injection in Naturally Fractured Reservoirs – Haft Kel Study without Diffusion

6.1 Introduction

We present results studying the enhanced-oil-recovery (EOR) potential for carbon dioxide (CO₂) injection in the naturally fractured Haft Kel field, Iran, on the basis of detailed compositional simulations of a homogeneous single matrix block surrounded by fractures. The effect of several key parameters will be study in detail—matrix permeability, matrix-block size, matrix/matrix capillary continuity (stacked blocks), and the use of injection gas mixtures of CO₂ and HC gas. However recovery in CO₂ injection cases is slow because molecular diffusion effect is not considered in this chapter.

Haft Kel field is located in the foothills of the Zagros Mountains, some 100 km east of Ahwaz city and on the east side of the Dezful embayment. The first oil well in Haft Kel was completed to a depth of 3363 ft in 1928, with an initial production rate of approximately 5700 STB/D. A field plateau rate of approximately 200,000 STB/D was maintained for several years, before the field was shut down from 1950 to 1954. Subsequently, production dropped to approximately 14000 STB/D in 1976. HC (separator) gas injection was initiated in June 1976, at a rate of 400 MMscf/D, with oil production stopped for

approximately 7 years between 1980 and 1987 to allow the oil column to build from 100 to 300 ft. Since 1987, the oil column and pressure have been held constant by gas injection, with a sustained oil rate of 35000 STB/D adding an additional 100 million STB produced from 1987 through 1995 (Saidi 1996).

6.2 Description of Model

A single matrix block surrounded by fractures was used to study the matrix/fracture fluid exchange in a gravity/capillary recovery mechanism. Significant compositional variations develop within the matrix block, resulting in high recoveries.

The matrix block is initially filled with oil, and the fractures are initialized with injection gas. Zero capillary pressure and high permeability (100 darcies) of the fractures means that the viscous forces are negligible compared with gravity and capillary forces. We define a large pore volume (PV) for the fracture, to eliminate effects of model injection and production wells. The matrix block is always surrounded by injection gas, and produced oil from the matrix block always enters the fracture system. Conceptually, we are looking at a matrix block located at the no-flow boundary between an injector and a producer in which lateral pressure gradients are negligible.¹

Haft Kel petrophysical properties and initial fluid compositions are taken from Saidi (1987). The matrix and the fracture dimensions and parameters are given in **Table 6.1**. Because of the matrix-block symmetry, only half of the matrix block is modeled. A 2D Cartesian grid is used where the matrix block is surrounded by two horizontal fractures at the top and bottom and one vertical fracture on the right side of the matrix block.

The reservoir simulator *SENSOR* is used for all simulations. An 11-component tuned Soave-Redlich-Kwong (SRK) equation of state (EOS) describes phase and volumetric behavior; the Lorenz-Bray-Clark correlation, tuned to viscosity data,

¹ Ringen *et al.* (2005) shows that this type of simulation model accurately represents reservoir-condition laboratory tests of gas gravity drainage for a carbonate core.

Table 6.1 – Matrix and Fracture Fixed Dimensions and Properties

Matrix width (X)	8 ft
Matrix length (Y)	8 ft
Vertical fracture width	0.01ft
Horizontal fracture height	0.01ft
Fracture permeability	100 D
Matrix porosity	10%
Fracture porosity	100%

Table 6.2 – Fluid Properties For The 11-Component SRK Characterization

Component	MW	Tc, °R	Pc, psia	ω	Vshift	Zc	Parachor
N2	28.01	227.16	492.84	0.037	-0.001	0.29178	59.10
CO2	44.01	547.42	1069.51	0.225	0.217	0.27433	80.00
H2S	34.08	672.12	1299.97	0.090	0.102	0.28292	80.10
C1	16.04	343.01	667.03	0.011	-0.002	0.2862	71.00
C2	30.07	549.58	706.62	0.099	0.059	0.27924	111.00
C3	44.10	665.69	616.12	0.152	0.091	0.2763	151.00
C4-C6	70.43	840.66	527.88	0.214	0.098	0.27403	216.05
C7-C14	136.82	1147.73	411.95	0.353	0.099	0.29826	384.35
C15-C21	239.68	1395.61	283.74	0.605	0.131	0.29826	657.60
C22-C29	341.31	1546.43	225.55	0.818	0.130	0.29826	855.51
C30+	487.10	1692.33	184.60	1.06576	0.09103	0.29826	1062.75

is used to calculate viscosities. EOS component properties and binary interaction parameters (BIPs) are given in **Tables 6.2** and **6.3**, respectively.

Pressure/volume/temperature (PVT) simulations needed to generate the EOS model from reported PVT data were made using *PhazeComp*. After tuning the EOS with black-oil properties reported by Saidi (1987), this PVT simulator was also used to generate saturated oil compositions for initializing the matrix block at pressures higher than and lower than the current reservoir pressure. Saturation pressure of the original oil composition was 1400 psia. Constant-composition-expansion (CCE) experiments are simulated to determine oil compositions below

Table 6.3 – BIPs for The 11-Component SRK Characterization

	N2	CO2	H2S	C1	C2	C3	C4-C6	C7-C14	C15-C21	C22-C29	C30+
N2	-										
CO2	0.0000	-									
H2S	0.0000	0.1200	-								
C1	0.0250	0.1050	0.0800	-							
C2	0.0100	0.1300	0.0700	0.0000	-						
C3	0.0900	0.1250	0.0700	0.0000	0.0000	-					
C4-C6	0.1040	0.1154	0.0544	0.0000	0.0000	0.0000	-				
C7-C14	0.1100	0.1150	0.0500	0.0000	0.0000	0.0000	0.0000	-			
C15-C21	0.1100	0.1150	0.0500	0.0000	0.0000	0.0000	0.0000	0.0000	-		
C22-C29	0.1100	0.1150	0.0500	0.0000	0.0000	0.0000	0.0000	0.0000	0.0000	-	
C30+	0.1100	0.1150	0.0500	0.0000	0.0000	0.0000	0.0000	0.0000	0.0000	0.0000	-

1400 psia.² Special “swelling” tests were made to calculate oil composition at higher pressures: Incipient bubblepoint gas from a lower pressure was added to the bubblepoint oil to raise the bubblepoint pressure. This process was started at 1400 psia and was repeated at 2000, 2500, and 3000 psia. The 11-component compositions for the reservoir oils and equilibrium gases at different saturation pressures are given in **Tables 6.4** and **6.5**, respectively. Other details of the simulator models are given below.

Table 6.4 – Oil Composition for The 11-Component EOS at Different Saturation Pressures

Component	1000 psi	1400 psi	2000 psi	2500 psi	3000 psi
N2	0.0004	0.0009	0.0019	0.0026	0.0033
CO2	0.0039	0.0043	0.0046	0.0048	0.0050
H2S	0.0133	0.0130	0.0122	0.0117	0.0113
C1	0.2211	0.2957	0.3873	0.4524	0.5089
C2	0.0494	0.0497	0.0490	0.0485	0.0481
C3	0.0542	0.0506	0.0460	0.0427	0.0399
C4-C6	0.1428	0.1282	0.1105	0.0979	0.0871
C7-C14	0.3761	0.3343	0.2837	0.2478	0.2167
C15-C21	0.0998	0.0887	0.0752	0.0657	0.0574
C22-C29	0.0299	0.0266	0.0225	0.0197	0.0172
C30+	0.0092	0.0082	0.0069	0.0060	0.0053

Tres= 110 °F

² Near-identical oil compositions result from CCE, differential liberation, and constant-volume tests or from depletion, which accounts for changing gas and oil mobilities.

Table 6.5 – Equilibrium-Gas Composition for The 11-Component EOS at Different Saturation Pressures

Component	1000 psi	1400 psi	2000 psi	2500 psi	3000 psi
N2	0.0050	0.0075	0.0106	0.0111	0.0110
CO2	0.0073	0.0064	0.0058	0.0056	0.0055
H2S	0.0098	0.0082	0.0072	0.0068	0.0068
C1	0.8913	0.8999	0.9004	0.8967	0.8907
C2	0.0520	0.0451	0.0409	0.0399	0.0399
C3	0.0225	0.0201	0.0194	0.0198	0.0205
C4-C6	0.0114	0.0117	0.0137	0.0162	0.0190
C7-C14	0.0006	0.0010	0.0020	0.0037	0.0064
C15-C21	0.0000	0.0000	0.0000	0.0000	0.0001
C22-C29	0.0000	0.0000	0.0000	0.0000	0.0000
C30+	0.0000	0.0000	0.0000	0.0000	0.0000

Oil recovery factor (RF) is calculated from total average oil saturation S_o in the matrix block using Eq. (3.2)

Capillary pressure and relative permeability are taken from Saidi (1987) and were fit to the Sensor analytical capillary pressure and relative permeability models (Eq. (2.17)-(2.22)).

This capillary pressure is scaled with IFT according to Eq. (2.24) where reference interfacial tension (IFT) is 10 mN/m. There is no capillary pressure in the fracture.

6.3 Grid Sensitivity

In this section, we discuss grid effect on oil recovery using equilibrium-gas and CO₂-gas injection at 1400-psia system pressure. The only requirement for accurate representation of recovery performance for gravity/capillary equilibrium in a system with constant phase properties (densities and IFTs) is sufficient vertical gridding to provide a good integration of the final equilibrium saturation/height relationship. Therefore, the oil recovery with equilibrium gas is the same for all grids considered, as we see in **Fig. 6.1**.

The recovery performance for CO₂ injection is affected by different gridding because of changing compositional effects, as shown in Fig. 6.1. 10×50 ($N_x \times N_z$)

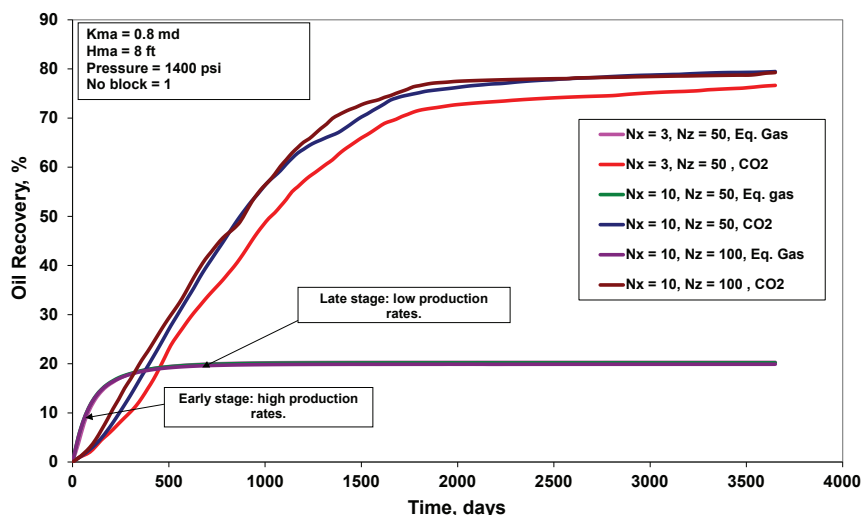


Figure 6.1 – Effect of grid cells on oil recovery vs. time for single matrix block using equilibrium-gas injection at system pressure of 1400 psia.

and 10×100 grids give higher recovery than 3×50 grids. A finer grid is needed for CO₂ injection to capture gravity and near-miscible displacement. Details of the CO₂-injection mechanism will be described in the next sections. Most equilibrium-gas-injection cases were run with a 10×50 ($N_x \times N_z$) grid, and a 10×100 grid for CO₂ injection.

6.4 Prediction of Minimum Miscibility Pressure (MMP)

1D slimtube simulations were used to determine the thermodynamic MMP. The slimtube simulations were performed at system pressures of 1000, 1400, 2000, 2500, and 3000 psia using 200, 500, and 1000 grid cells. The results of recoveries for the different runs vs. system pressure are given in **Fig. 6.2**; final recoveries are defined as 1 minus the fraction of initial oil in place remaining after 1.2 PV of CO₂ injected, divided by the initial oil in place. At each pressure, linear regression was used to fit these recoveries vs. $1/\sqrt{N}$, where N is the number of cells. Recoveries are extrapolated to infinite grid cells. The MMP is 1400 psia according to slimtube simulations interpreted as described above, which

compares favorably with the PhazeComp-calculated multicell algorithm MMP of 1,350 psia for a condensing/vaporizing mechanism.

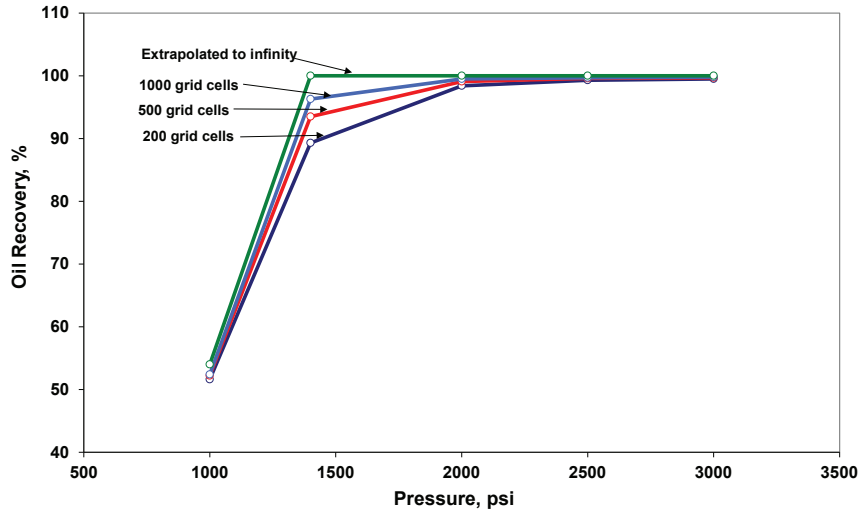


Figure 6.2 – Slimtube simulation using CO₂ injection gas. Oil recovery at 1.2 PVs of gas injected vs. pressure for different number of grid cells.

6.5 Injection-Gas Mechanism

6.5.1 Equilibrium Gas in a Single Matrix Block

If the gravity forces exceed capillary forces, gas enters the top of the matrix block and oil is produced from the bottom of the matrix block. Viscous forces may be present during oil production from a matrix block. Viscous/gravity ($R_{v/g}$), Eq. (3.1), and capillary/gravity ($R_{c/g}$) dimensionless ratios are used to understand the importance of the various recovery mechanisms during production (Wylie and Mohanty 1999; Stalkup 1983; Løvøll *et al.* 2005):

$$R_{c/g} = \frac{\Delta P_{cap}}{\Delta P_{grav}} = \frac{\Delta P_{cap}}{g\Delta\rho_{og}h} \dots\dots\dots (6.1)$$

where $\Delta\rho_{og}$ is oil and gas density difference, g is gravity-acceleration constant, h is grid-cell height, and ΔP_{cap} is capillary pressure gradient at the displacement front.

The recovery process can be divided approximately into two main periods: a quick initial production period characterized by high oil rates when most of the oil is recovered, followed by a final long production period characterized by lower production rates.

Oil primarily flows in the vertical direction, whereas gas enters both from the top and from the sides. After 30 days when only 4% of the oil has been recovered, the gas has entered only the topmost blocks of the core. $R_{v/g}$ and $R_{c/g}$ are equal at 0.005 and 0.15, respectively. These numbers suggest that gravity drainage is the dominant mechanism. After 180 days, approximately 15% of the original oil in place is recovered and the gas front has reached the capillary holdup zone (entry height). The profile is now almost uniform in the vertical direction; however, the gas saturation behind the front is less than the ultimate equilibrium gas saturation, so there is still a significant amount of oil left to be recovered. This is illustrated in Fig. 6.1, showing that it takes only 180 days to recover 15% of the oil, whereas it takes nearly 1,000 days to reach 20% ultimate oil recovery.

The initial period with high production rates ends when the displacement front reaches the capillary holdup zone in the matrix block. At this point, the gas saturation behind the front has not reached the final equilibrium profile and there is still potential for additional oil recovery. However, the recovery of remaining oil during the last stage is slow because of low oil mobility.

The parameters controlling the rate of recovery, but which have limited impact on ultimate recovery, are (a) absolute matrix permeability, (b) shape of the relative permeability curve, and (c) matrix block-to-block flow (re-infiltration). Parameters that control the ultimate recovery are (a) pressure (because of IFT and density dependence), (b) capillary pressure curve, and (c) endpoint saturations S_{org} and S_{wc} .

The following subsections present sensitivity simulations for these parameters. Unless stated otherwise, only a single parameter is changed in each sensitivity, keeping the other properties equal to base-case values.

6.5.2 Mechanism of CO₂ in a Single Matrix Block

In this subsection, we investigate the recovery mechanism of CO₂ in a single matrix block. In general, CO₂ gas has a higher viscosity than HC gas and, therefore, a better mobility ratio. In our study, we focus on the mechanism of gravity/capillary drainage, thereby making mobility ratio a less important parameter. CO₂-gas injection reduces gas/oil IFT significantly, and this has a pronounced impact on recovery by reducing the capillary retaining forces.

As seen in **Fig. 6.3**, CO₂ is lighter than oil at lower pressures, but can be heavier than oil at higher pressures. For Haft Kel, CO₂ has a higher density than reservoir oil at pressures above 2050 psia. This characteristic results in two fundamentally different recovery mechanisms for CO₂, depending on the sign of the CO₂-oil density difference.

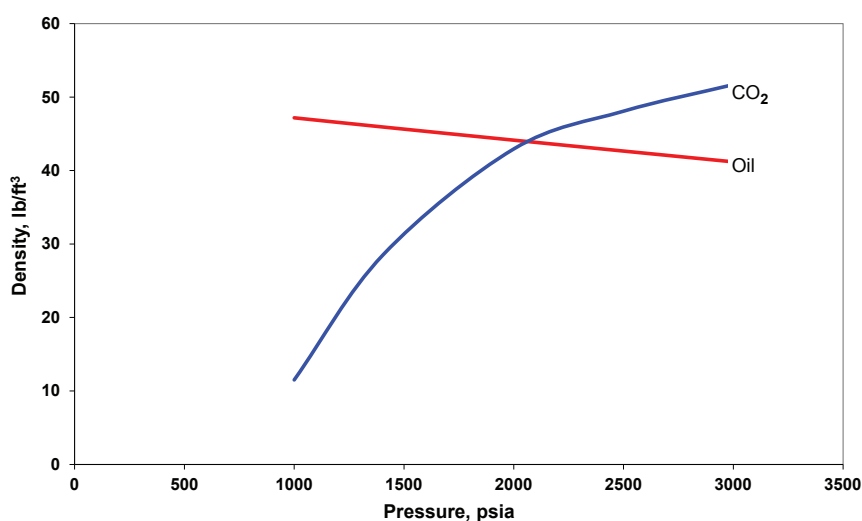


Figure 6.3 – Comparison of CO₂ and Haft Kel oil densities as a function of pressure (at reservoir temperature of 110 °F).

6.5.2.1 CO₂ Lighter Than Oil.

When CO₂ is lighter than oil, CO₂ enters from top of the matrix block as in a traditional gas gravity-drainage mechanism. As shown in **Fig. 6.4**, the recovery behavior of CO₂ injection can be divided into three periods: an initial production period of high oil rates and two longer production periods characterized by lower production rates. The final period results in significant extra oil recovery from a capillary-drive mechanism first described by Uleberg and Høier (2002). **Figs. 6.5 through 6.7** show saturation distributions during the three periods, respectively.

The first two periods are similar in shape to the equilibrium gravity/capillary mechanism, but with a more complicated recovery mechanism. Because IFT decreases more significantly in CO₂ injection, capillary entry height decreases to result in higher ultimate recoveries after the first and second periods. Viscous/gravity ($R_{v/g}=0.004$) and capillary/gravity ($R_{c/g}=0.006$) ratios clarify that gravity drainage is the dominant mechanism during this period of oil production. This is illustrated in Fig. 6.4, which shows that it takes 1,400 days to recover 70% of the oil (end Phase 1), but not before 7400 days does recovery reach 84% (end Phase 2).

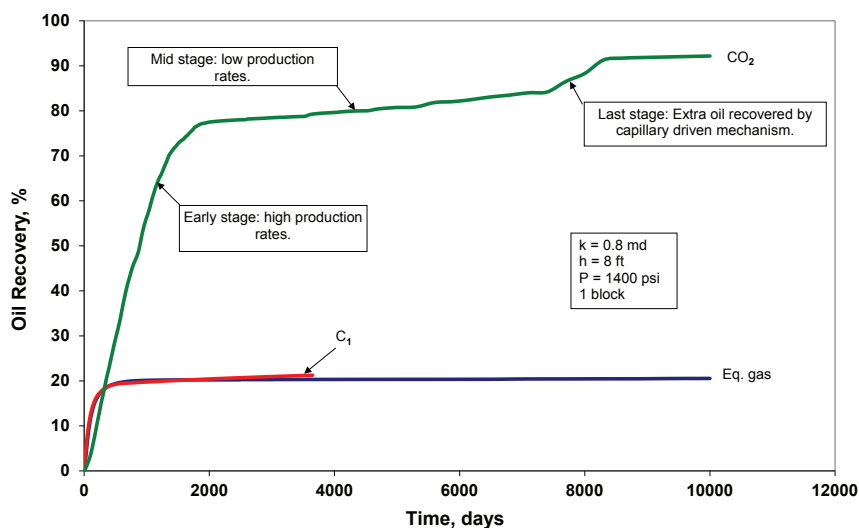


Figure 6.4 – Effect of different injection gas on oil recovery vs. time for single matrix block at system pressure of 1400 psia.

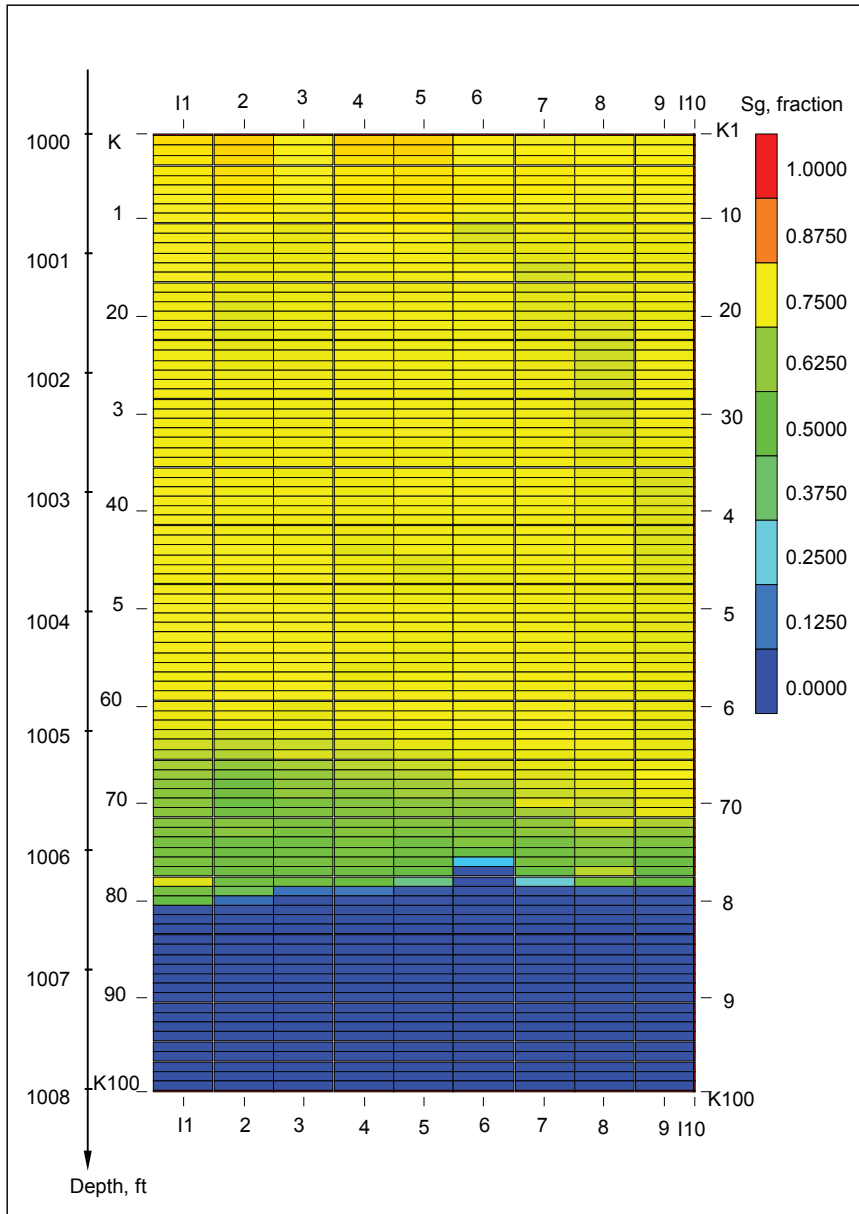


Figure 6.5 – Early stage CO₂ gas displacement, gas saturation profile inside matrix block after 1410 days at system pressure of 1400 psia (at 71% oil recovery).

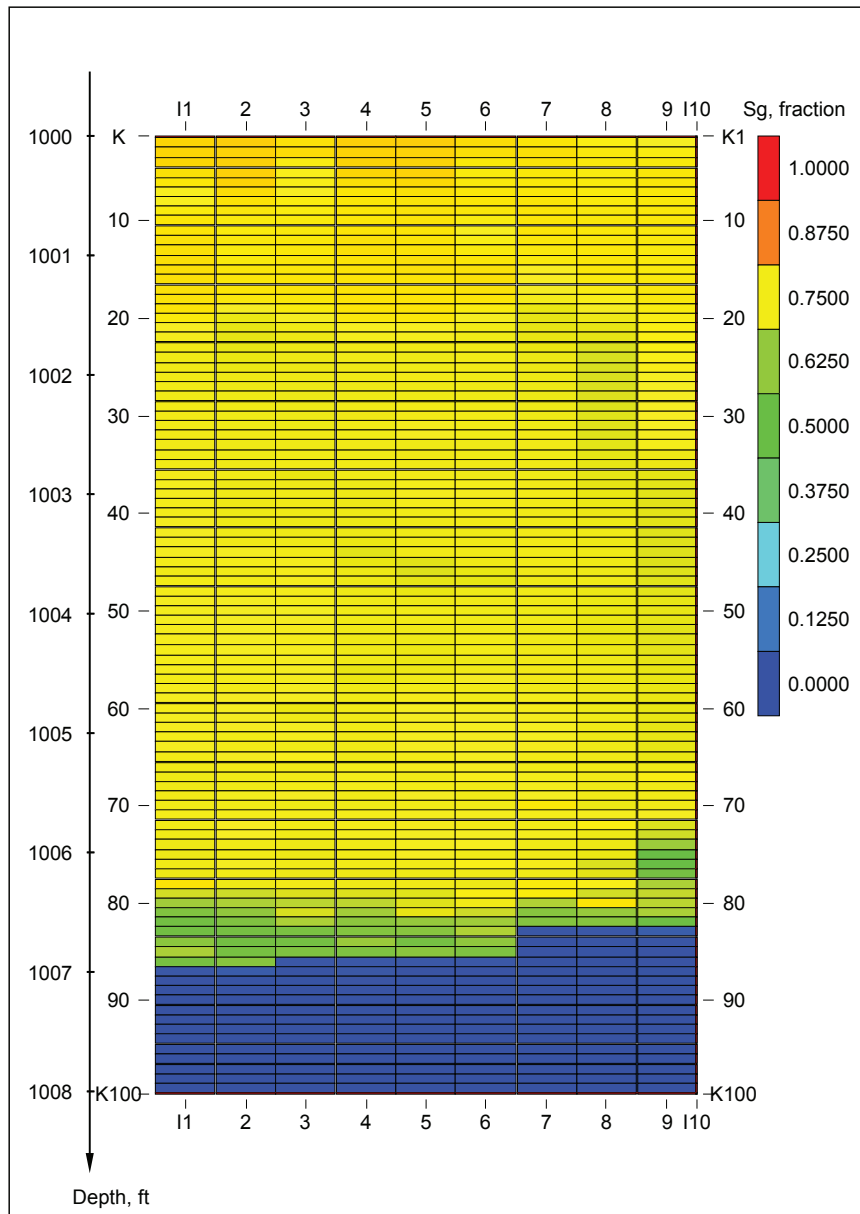


Figure 6.6 – Mid stage CO_2 gas displacement, gas saturation profile inside matrix block after 3600 days at system pressure of 1400 psia (at 79% oil recovery).

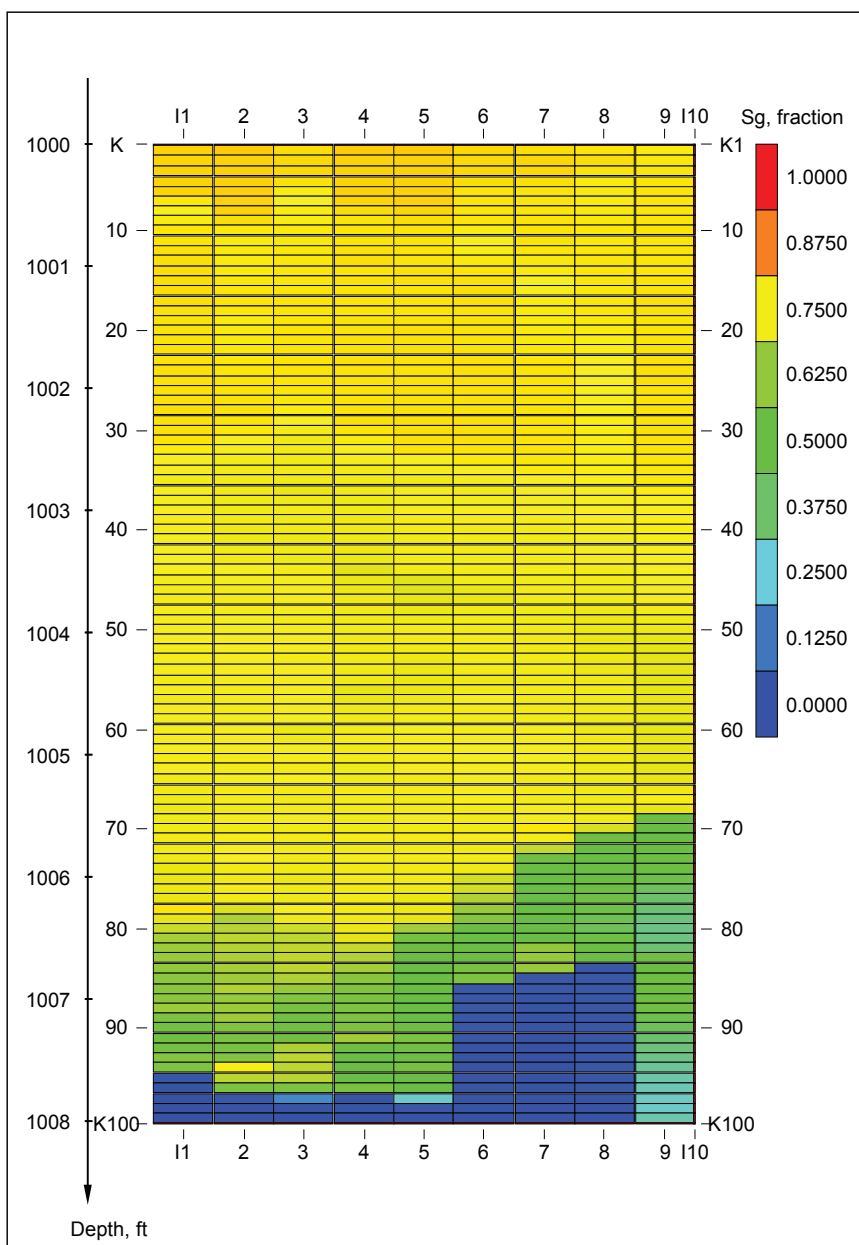


Figure 6.7 – Late stage CO₂ gas displacement, gas saturation profile inside matrix block after 7100 days at system pressure of 1400 psia (at 84% oil recovery).

As shown in **Fig. 6.8**, the extreme decrease in the gas/oil IFT near the displacement front results in a strong IFT and, consequently, capillary pressure gradient. Uleberg and Høier (2002) describe the resulting process, “This, combined with a relative small phase density difference near the miscible front, induces a Darcy flow of oil against gravity. As the oil flows upwards it contacts fresher and leaner gas and the intermediate and heavy components of the oil are more easily vaporized. The oil components that vaporize to the gas phase are then transported to the fracture system by: (1) injectant gas replacing the matrix block gas due to the density difference and (2) molecular diffusion due to the compositional difference between the gas in the fracture system and in the matrix block.”

“Oil is transported upwards by IFT induced Darcy flow even after the gas-oil front has reached the capillary entry height. This results in a shrinking of the oil zone at the bottom of the matrix block, and fracture gas more easily enters below the initial capillary entry height level. Eventually most of the original oil from the matrix block will be produced.”

“Increasing the system pressure makes the displacement process more miscible. The phase density differences are less and the IFT gradient near the miscible front is more pronounced, creating an even greater potential for the oil to flow upwards, and at higher rate.”

The capillary-driven mechanism transpires throughout the displacement (Periods 1, 2, and 3), though it is more pronounced in the late period of displacement, verified by a capillary/gravity ratio $R_{c/g}=22.15$.

In the early stage, displacement preferentially moves along the fracture side (Fig. 6.5) because there is fresh CO₂ available, with more oil vaporized and production to the fracture. The matrix-block grid cells in the vicinity of fracture have higher CO₂ concentrations. The IFT gradient at the displacement front is less toward the fracture (Fig. 6.8). For that reason, displacement is preferentially in the matrix block center during the late stage of recovery (Fig. 6.7).

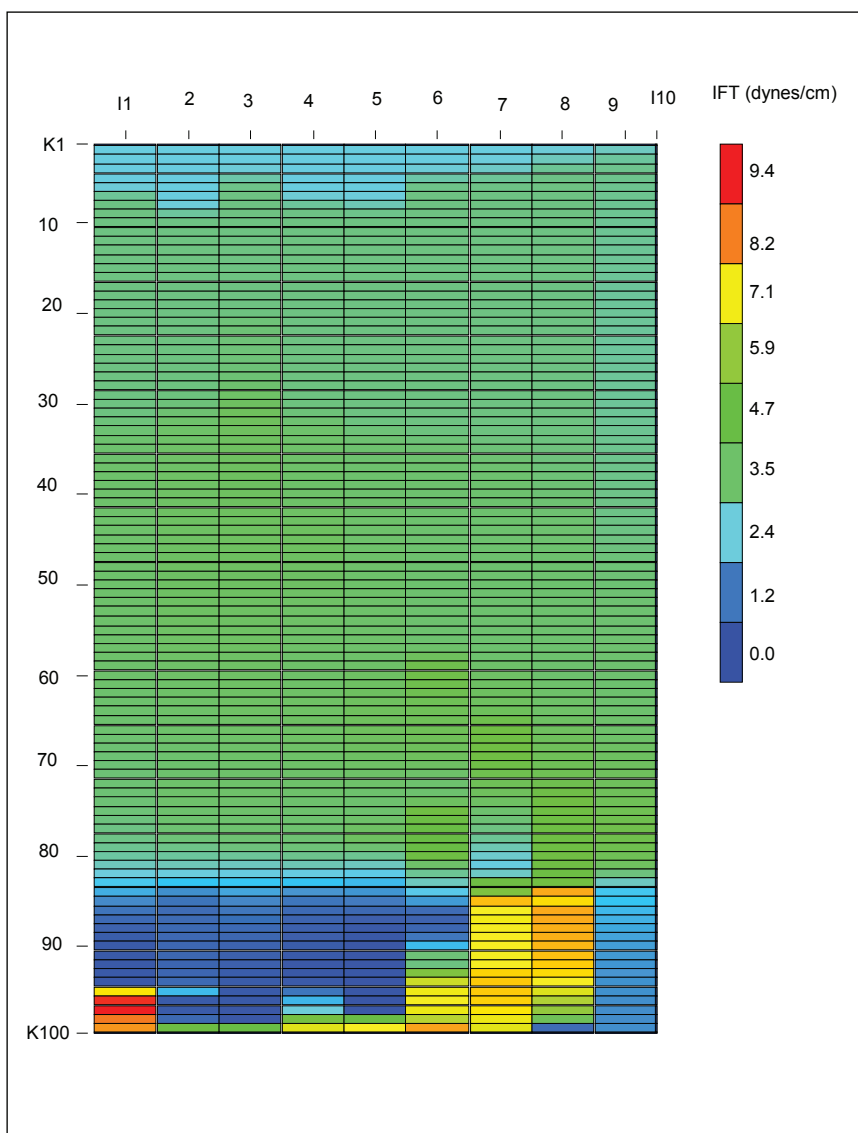


Figure 6.8 – Late stage CO₂ gas displacement, interfacial tension profile inside matrix block after 7100 days at system pressure of 1400 psia (at 84% oil recovery).

6.5.2.2 CO₂ Heavier Than Oil.

At early times, CO₂ dissolves into the oil phase and some lighter oil components vaporize into the CO₂-rich gas phase. This results in increasing oil and gas densities in the matrix block, with very-low density differences near the upward-moving front. As shown in **Fig. 6.9**, IFT decreases dramatically at the displacement front, from 3.8 to 0.06 mN/m implying that the process is near miscible (system pressure of 2500 psia is far above the thermodynamic MMP of 1350 psia³).

Before the upward-moving front reaches the top of the matrix block, three characteristic phases coexist in the matrix block. The original oil phase exists in the upper section of the matrix block, ahead of the front. Behind the front, a gas phase and an equilibrium oil phase exist, though the phase compositions vary significantly from the matrix bottom to the front.

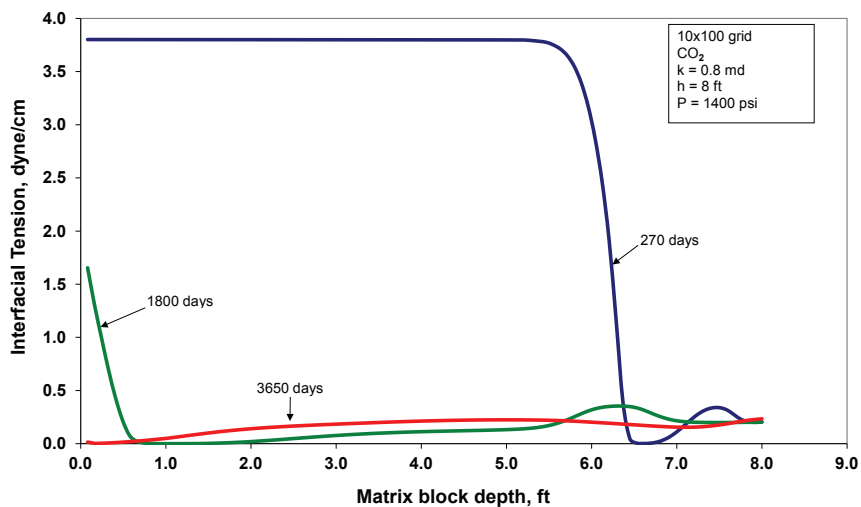


Figure 6.9 – IFT profile for single matrix block using CO₂ injection gas at system pressure of 2500 psia.

³ We did not study the front's approach to miscibility as grid refinement is increased to large numbers and dispersivity is reduced toward zero (an assumption in the thermodynamic MMP).

The front moves upward as the frontal gas pushes original oil from the top of the matrix block, as seen in **Fig. 6.10**. Behind the front we find a complex flow mechanism where remaining oil eventually becomes heavier as it is vaporized by the gas. This oil starts flowing downward out the bottom of the matrix block, but at a low rate because of low mobility.

When the gas front reaches the top of the matrix block, CO₂ starts to enter from the top and the remaining oil is produced slowly from the bottom of the matrix block by gravity drainage; the remaining oil is denser than CO₂ but has low mobility.

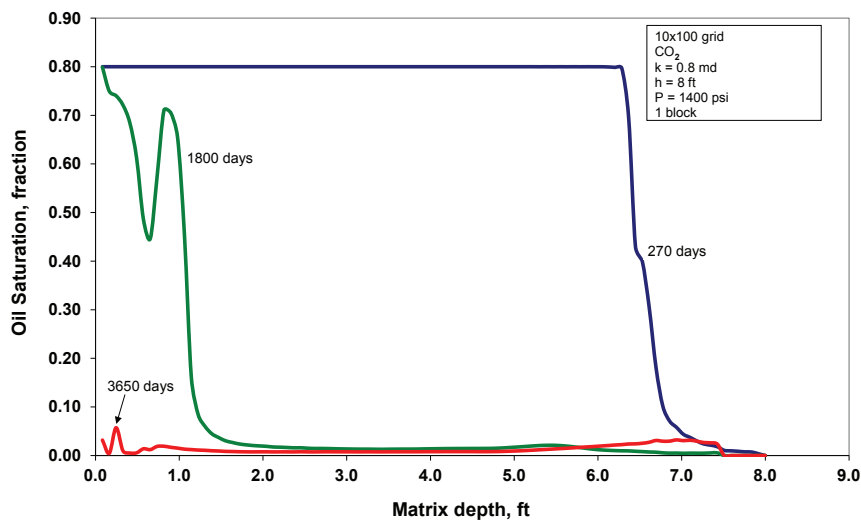


Figure 6.10 – Oil saturation profile for single matrix block using CO₂ injection gas at system pressure of 2500 psia.

6.6 Injection-Gas Effect

In this section, we study different injection gases for a single matrix block. We examine equilibrium-gas, dry-gas (C₁), and CO₂ injection at a system pressure of 1400 psia. Results are shown in Fig. 6.4. The CO₂ injection case has highest ultimate oil recovery (recovery at 10000 days), approximately 92%, while the equilibrium gas and dry gas have the same oil recovery of approximately 20%.

As mentioned earlier, 1,400 psia is the thermodynamic MMP for CO₂ with Haft Kel oil.

6.6.1 CO₂-Dilution Effect

Because the Haft Kel field has a large gas cap, injected gas may dilute with gas-cap equilibrium gas because of convective and diffusive flow in the fracture system. CO₂ concentration at a given fracture location in the reservoir will depend on many effects, including gravity segregation, gas/gas diffusion, gas-injection rate, matrix-block permeability, gas-cap size, and location of injector perforations. Fracture gas compositions surrounding matrix blocks may vary substantially, with associated impact on oil recovery.⁴

We studied several CO₂ mixtures—i.e., 50, 80, and 90 mol% CO₂ mixed with equilibrium gas at 1400 psia. As shown in **Fig. 6.11**, the ultimate oil recoveries for these three gases were 24.5, 34.5, and 52%, respectively. Reduced oil recoveries are related to increased gas/oil IFT and less-efficient condensing/vaporizing behavior near the displacement front (i.e., an increase in MMP) as CO₂ concentration decreased in the injection gas.

6.6.2 Tertiary Recovery by CO₂ Injection

Haft Kel dry-gas injection started in 1976. Dry-gas injection behaves very similar to equilibrium-gas injection, with similar recovery performance. Basically, the injected dry gas changes composition when it contacts reservoir oil, with a resulting gas composition that is very close to the incipient gas composition of the original oil. In this section, we present results from our study of recovery performance when CO₂ is injected following dry-gas injection.

Different concentrations of CO₂ were mixed with HC (equilibrium or dry) injection gas, the resulting mixture being injected into the fracture system following an initial period of HC-only gas injection. Two wells were used in

⁴ We suspect that gravity segregation in the fracture system may segregate the injected CO₂ into a “blanket” of high-CO₂ gas on the top of the fracture oil column, with a HC gas floating on the CO₂ blanket.

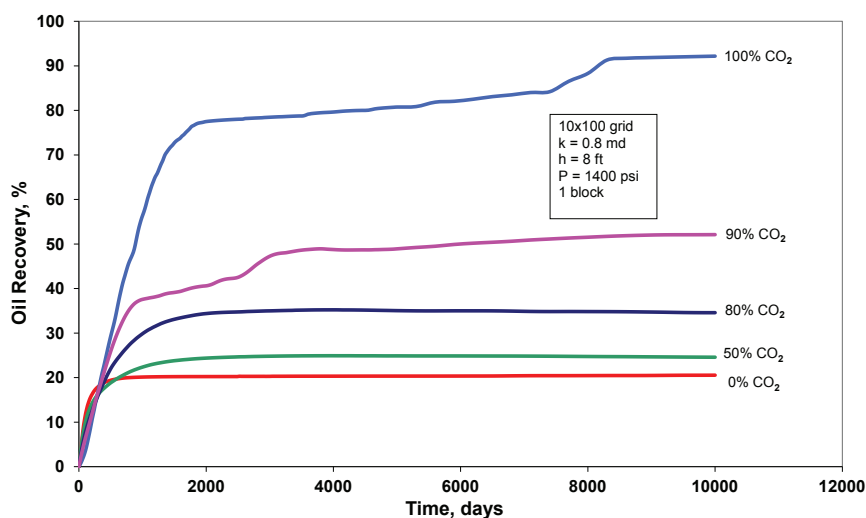


Figure 6.11 – Effect of CO₂ dilution on oil recovery vs. time for single matrix block at system pressure of 1400 psia.

these simulations, allowing injection-gas composition to change with time. The injection well was perforated in the top fracture, and the producer was perforated in the bottom fracture. The injection well was controlled by a constant bottomhole pressure, and the producer was controlled by constant gas-production rate of 0.353 Mscf/D.

Injection gases with 100, 90, 80, and 50 mol% CO₂ mixed with equilibrium gas at reservoir pressure of 1400 psia were injected after first injecting equilibrium gas only into the matrix block. Equilibrium gas was injected for 1500 days to ensure that the equilibrium-gas displacement was complete. This was followed by injection with a CO₂-rich gas. Results are given in **Fig. 6.12**. The ultimate oil recoveries for 100 (pure), 90, 80, and 50 mol% CO₂ mixtures were 93, 51, 36, and 26%, respectively.

These ultimate oil recoveries are close to those found where CO₂-rich gases were injected without first injecting equilibrium HC gas. However, the recovery mechanism is slightly different. First, oil recovery drops as a result of CO₂

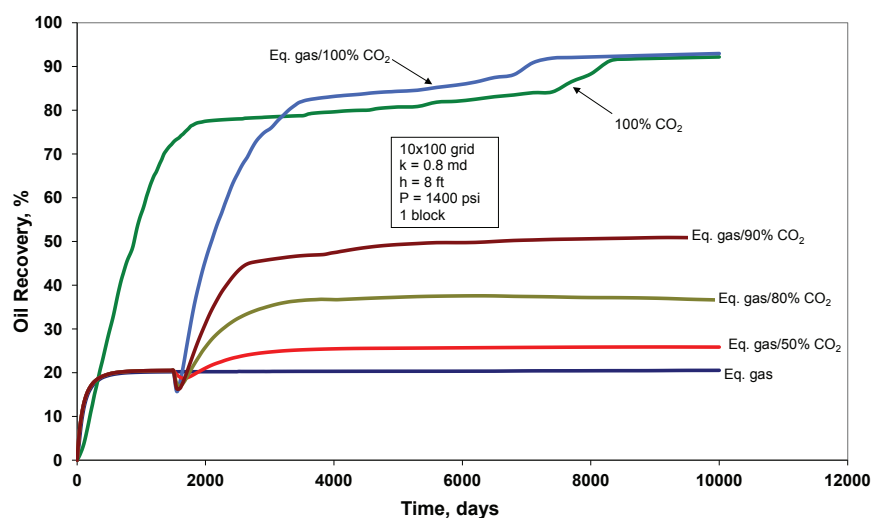


Figure 6.12 – Effect of injection gas, inject different concentration of CO₂ after equilibrium and Methane injection on oil recovery vs. time for single matrix block at system pressure of 1400 psia.

swelling in the matrix block with associated oil-saturation increase, leading to lower oil recovery, based on Eq. (3.2). Second, the injected CO₂ gas at 1400 psia is lighter than oil but heavier than the initial HC gas in the matrix block. Consequently the CO₂-rich gas cannot enter from the top or from the bottom of matrix block. Instead, it enters from the side of the matrix block by exchanging composition with gas in the matrix. The front for CO₂ mixed with matrix-block gas moves in both horizontal and vertical directions. After CO₂ enters into the matrix block, gravity/capillary drainage becomes strong and oil produces from the bottom of the matrix block.

6.6.3 Reservoir-Pressure Effect

The effect of reservoir pressure on oil recovery for equilibrium gas, CO₂, and different mixtures of CO₂ and equilibrium injection gas is studied in this section. Different models are used, with the system pressure of 1000, 1400, 2000, 2500, and 3000 psia. The equilibrium-gas models use 10×50 ($N_x \times N_z$) grid cells; for

each pressure, the matrix block is initialized with saturated oil and the fracture is initialized with equilibrium gas. CO₂-injection models contain 10×100 grid cells, and for each pressure case, the matrix block is initialized with saturated oil and the fracture is initialized with CO₂.

For the equilibrium-gas cases, gas/oil IFT decreases with increasing reservoir pressure. As a result, the capillary entry height is lowered and ultimate oil recovery increases. As shown in **Fig. 6.13**, oil recovery increases from 14% at 1000 psia to 50% at 3,000 psia, corresponding to a change in gas/oil IFT from 13.55 to 2.24 mN/m.

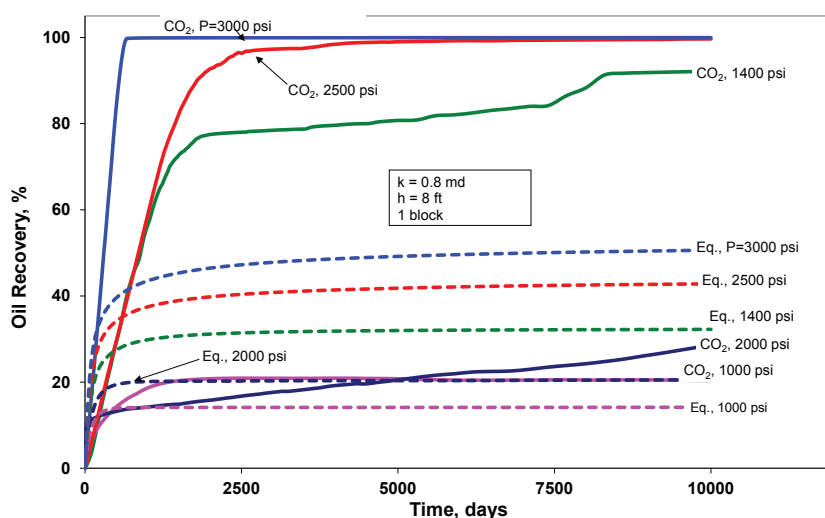


Figure 6.13 – Effect of reservoir pressure on oil recovery vs. time for single matrix block system using equilibrium gas (dash line) and CO₂ (solid line) injection.

For CO₂ injection, we find that oil recovery generally increases with reservoir pressure, reaching nearly 100% near the thermodynamic MMP of 1400 psia. A significant anomaly is seen at 2000 psia, where recovery is less than 30% after 10000 days (when all other runs had essentially reached ultimate recovery), as seen in Fig. 6.13. CO₂ and oil densities are approximately equal at 2000 psia, as shown in Fig. 6.3, and consequently gravity drainage is slowed radically.

Mixtures of CO₂ and equilibrium gas at 2000 psia show higher oil recovery than pure CO₂ (**Fig. 6.14**) because gas/oil density differences are higher than for pure CO₂. Fig. 6.14 shows that oil recovery rises toward 100% as the thermodynamic MMP is approached. MMP increases with decreasing CO₂ content in the injection gas, and the RF-pressure trend toward near-100% recovery becomes less steep.

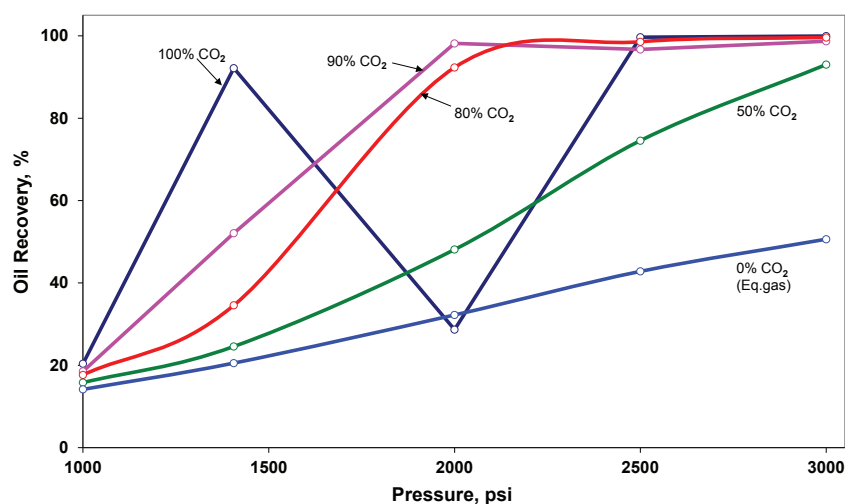


Figure 6.14 – Comparison of CO₂ injection gas with equilibrium gas oil recovery at 10000 days vs. reservoir pressure for Single matrix block system.

6.7 Matrix-Block Height Effect

The matrix-block height is a critical parameter for gas injection in fractured reservoirs. If the matrix-block height is smaller than the initial capillary entry height, no gas can enter (unless by diffusion).

Haft Kel block size varies from 6 to 14 ft, as reported by Saidi (1996). We considered four matrix-block heights—6, 8, 10, and 14 ft—to study the effect of matrix-block height on oil-recovery performance for equilibrium gas (dashed line) and CO₂ (solid line), as shown in **Fig. 6.15**.

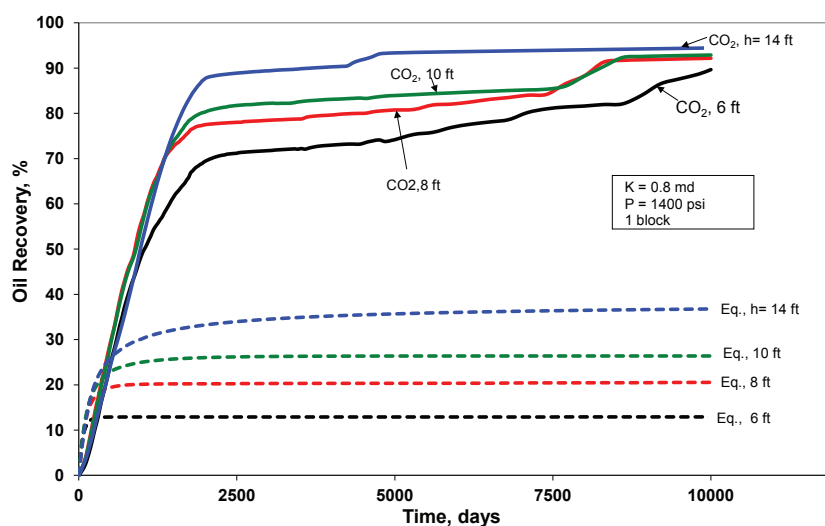


Figure 6.15 – Effect of matrix block height on oil recovery vs. time for single matrix block using equilibrium (dash line) and CO₂ (solid line) injection gas at system pressure of 1400 psia.

When equilibrium gas is injected, the ultimate oil recovery increases significantly with increasing stack height for small matrix blocks close to the capillary entry height. The ultimate recovery approaches an asymptotic value given by the saturation endpoints, S_{org} and S_{wc} , and the effect of matrix-block height on the final recovery is not significant for very tall matrix stack heights. The stack height does not have a strong effect on the oil-production rate, meaning that the time to reach a given recovery increases with stack height (because of changes of amount of fluids in place). Previous studies (Saidi 1996; Behbahani *et al.* 1996) on Haft Kel field pointed out that the oil recovery by immiscible HC gas varies between 15 and 32%. As seen in Fig. 6.15, the lowest and highest oil recoveries are 12.9 and 36.7% for 6- and 14-ft matrix blocks, respectively.

For CO₂ injection, the ultimate oil recovery is approximately the same for all stack heights. First, the capillary entry height in CO₂ injection is lower than the capillary entry height of equilibrium-gas injection, caused by low IFT in a developed condensing/vaporizing near-miscible process. Furthermore, the oil

below capillary entry height is produced by the dynamic gravity/capillary-drive mechanism, as described by Uleberg and Hoier (2002). Ultimate recovery from this mechanism is not greatly affected by matrix-block height, as shown in Fig. 6.15.

6.8 Matrix-Block-Permeability Effect

The matrix permeability controls the rate of recovery from a matrix block, and the ratio between the matrix and fracture permeability determines if viscous displacement (Darcy flow by pressure gradients) is important or not. If injection fluid mainly flows in the fracture, then viscous force is negligible in low-permeability matrix block. Matthai and Belayneh (2004) studied the effects of matrix/fracture permeability ratio on fracture/matrix flow partitioning, and their results indicate that at a ratio of fracture permeability to matrix permeability of 10^4 and lower, viscous force becomes important. Porosity and capillary pressure are assumed to be constant in all cases.

In Haft Kel, matrix-block permeability varies from 1 to 0.05 md. For equilibrium-gas injection, the rate of oil recovery increases with increasing matrix-block permeability, but ultimate oil recovery is the same, as shown in **Fig. 6.16**. As shown in Fig. 6.16, CO_2 has the same effect but it is more pronounced because the rate of oil recovery in CO_2 injection is slower than the rate of oil recovery for equilibrium-gas injection.

Interestingly, there is a linear relationship between the time to reach a given oil recovery and the matrix permeability, when plotted on log-log paper. This is seen in **Fig. 6.17**, where the times to reach specific recoveries of 10, 15, and 20% are considered. The lines have the same slope for both equilibrium gas and CO_2 . Fig. 6.17 is useful to find the time to reach a given oil recovery for a wide range of matrix-block permeabilities.

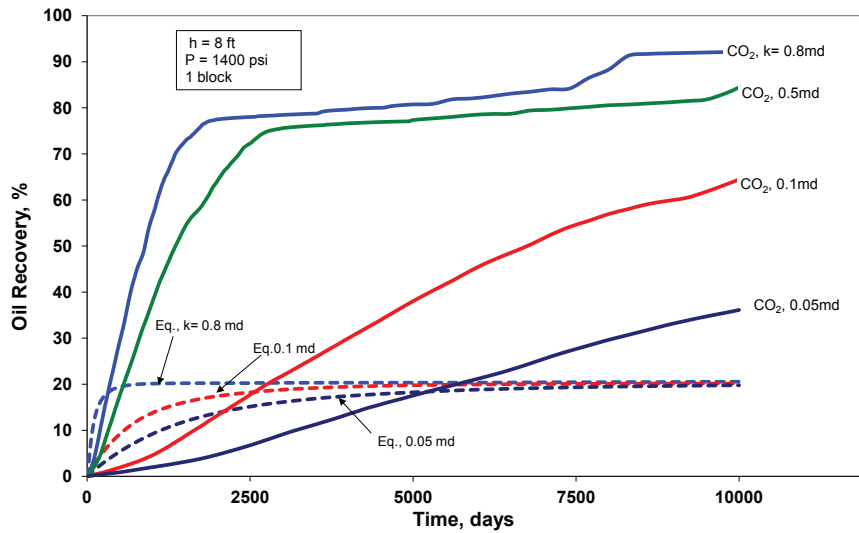


Figure 6.16 – Effect of matrix block permeability on oil recovery vs. time for single matrix block using equilibrium (dash line) and CO₂ (solid line) injection gas at system pressure of 1400 psia.

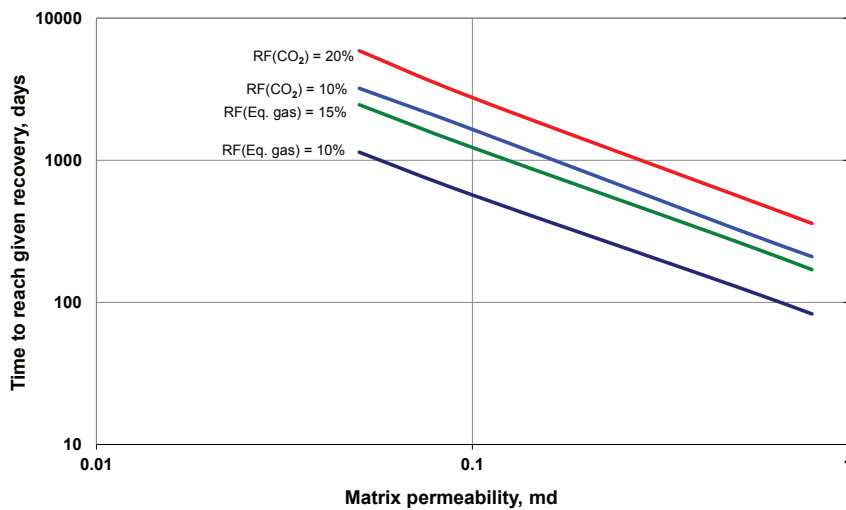


Figure 6.17 – Time of reaching certain oil recovery vs. Matrix block permeability for single matrix block using equilibrium and CO₂ injection gas at system pressure of 1400 psia.

6.9 Block-to-Block Interaction

Oil produced from one matrix block may flow into an underlying matrix block. Oil reinfiltration may result from physical contact between the blocks (permeable contact points) or by oil produced from one block entering another block because of gravity/capillary interaction, liquid bridges, or film flow. We studied the effect of vertical block-to-block interaction using taller effective matrix-block heights.

In our model, the matrix blocks are 8 ft in height, and are separated by horizontal fractures. The top, bottom, and side fractures are defined with a large PV to provide the gas needed to inject and to eliminate injection and production wells. Thin horizontal fractures were gridded to represent the connection of one matrix block with another.

For equilibrium gas we studied 1, 5, 10, 20, and 40 stacked matrix blocks using $3 \times 1 \times 25$ grid cells for each matrix block. **Fig. 6.18** illustrates the total oil recoveries for different stacked matrix blocks. Total oil recovery is the arithmetic average of oil recovery for all matrix blocks. This figure shows significant delay of oil production because of oil reinfiltration.

Another series of stacked matrix blocks were studied to compare CO₂ injection with equilibrium gas. The CO₂-injection cases have higher total oil recoveries than equilibrium-gas cases, as shown in **Fig. 6.19**. Fig. 6.19 shows that the shape of oil recovery for stacked blocks does not include the final stage of single-block oil recovery in which the extra oil is recovered exclusively by the dynamic gravity/capillary mechanism.

The cases shown here represent 100% reinfiltration. It is likely that the degree of reinfiltration is less in the field. Many factors can reduce block-to-block flow significantly, such as interbedded layers of nonfractured impermeable rock (shales and mineral-filled fractures), sloped fractures, and viscous forces.

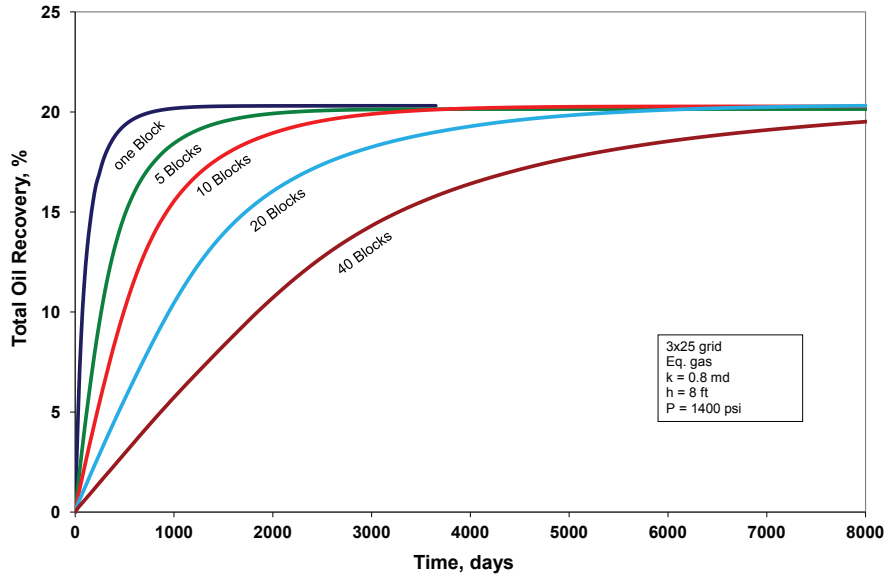


Figure 6.18 – Total oil recovery vs. time for different number of stacked matrix blocks using equilibrium gas injection at system pressure of 1400 psia.

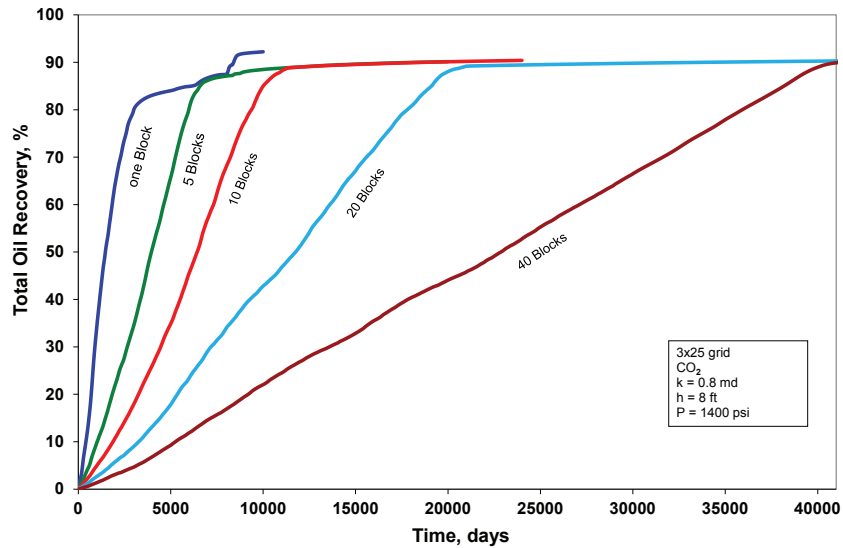


Figure 6.19 – Total oil recovery vs. time for different number of stacked matrix blocks using CO₂ gas injection at system pressure of 1400 psia.

6.10 Conclusions

Oil-recovery performance was quantified for the Haft Kel oil system using compositional modeling of a matrix block surrounded by a gas-filled fracture. Simulations were performed for a wide range of petrophysical properties, matrix-block sizes, injection gas, varying initial conditions of pressure, and saturation pressure.

Some of the most interesting observations and conclusions concerned CO₂ injection include:

1. Grid refinement is needed for accurate modeling of nonequilibrium gas injection because of a complex gravity/capillary recovery mechanism with significant IFT and capillary pressure gradients.
2. CO₂ is heavier than the Haft Kel oil at pressures greater than 2,050 psia. When CO₂ gas is lighter than oil, CO₂ gas enters from the top of the matrix block and drains oil downward, as found with all other injection gases.
3. When pure CO₂ is heavier than the reservoir oil, CO₂ gas initially enters from the bottom of the matrix block. Unusual saturation gradients develop, with near-initial oil saturation at the top of the matrix block remaining until the upward-moving gas front reaches the top. Gradually, the oil at the bottom of the matrix becomes heavier than its equilibrium HC/CO₂ matrix gas mixture, resulting in “normal” gravity segregation.
4. Despite high ultimate oil recovery with CO₂, the process is slow (compared with nonequilibrium HC gases) and particularly when the CO₂-gas and reservoir-oil densities are similar.
5. Ultimate oil recovery increases with increasing reservoir pressure and CO₂ concentration in injection gas.
6. CO₂ injection in Haft Kel field can lead to significant additional oil production, even after dry-gas injection.

6.11 References

- Behbahani, H.S.-Z., Kharrat, R., and Vossoughi S. 1996. Case History of a Unique Gas Injection Scheme and its Simulation Using Material Balance Based Simulator. Paper SPE 35631 presented at the SPE Gas Technology Conference, Calgary, 28 April–1 May. doi: 10.2118/35631-MS.
- Coats Engineering: *SENSOR*, www.coatsengineering.com.
- Løvoll, G., Meheust, Y., Måløy, K. L., Aker, E., and Schmittbuhl, J. 2005. Competition of gravity, capillary and viscous forces during drainage in a two-dimensional porous medium, a pore scale study. *Energy* **30** (6): 861–872. doi:10.1016/j.energy.2004.03.100.
- Matthai, S.K. and Belayneh, M. 2004. Fluid flow partitioning between fractures and a permeable rock matrix. *Geophys. Res. Lett.* **31**: L07602. doi:10.1029/2003GL019027.
- Ringen, J.K., Haugse, V., Høier, L., Berge, L.I., and Reed, J. 2005. Experimental and Numerical Studies of Gas Injection in Fractured Carbonates: Pressure and Compositional Effects. Paper presented at the 2005 International Symposium of Society of Core Analysts, Toronto, Canada, 21–25 August.
- Saidi, A.M. 1987. *Reservoir Engineering of Fractured Reservoirs: Fundamental and Practical Aspects*, 764–770. Paris: TOTAL Edition Press.
- Saidi, A.M. 1996. Twenty Years of Gas Injection History into Well-Fractured Haft Kel Field (Iran). Paper SPE 35309 presented at the International Petroleum Conference and Exhibition of Mexico, Villahermosa, Mexico, 5–7 March. doi: 10.2118/35309-MS.
- Stalkup, F.I. Jr. 1983. *Miscible Displacement*. Henry L. Doherty Monograph Series, SPE, Richardson, Texas, USA **8**.
- Uleberg, K. and Høier, L. 2002. Miscible Gas Injection in Fractured Reservoirs. Paper SPE 75136 presented at the SPE/DOE Improved Oil Recovery Symposium, Tulsa, 13–17 April. doi: 10.2118/75136-MS.

Wylie, P.L. and Mohanty, K.K. 1999. Effect of Wettability on Oil Recovery by Near-Miscible Gas Injection. SPE Res Eval & Eng **2** (6): 558–564. SPE-59476-PA. doi: 10.2118/59476-PA.

Zick Technologies: *PhazeComp*. www.zicktech.com.

Chapter 7

CO₂ Injection in Naturally Fractured Reservoirs – Lab and Field Modeling Studies with Diffusion

7.1 Introduction

Based on detailed compositional simulations of matrix/fracture systems, we study the effect of molecular diffusion on oil recovery by CO₂ injection for small-scale laboratory experiments and field-scale systems. We consider reservoir conditions that lead to a range of recovery mechanisms from immiscible to near-miscible.

Laboratory experimentation is a useful approach to understand the recovery mechanism of CO₂ injection in fractured oil reservoirs because an unusual combination of complex physical phenomena exists. A fundamental problem with this approach is scaling the results to field conditions, and particularly matrix block size which is often many (5-100) times larger than laboratory cores. Diffusion is clearly affected by matrix block dimensions, and any effect of diffusion on the recovery mechanism will be scale dependent. In this chapter we provide guidelines and computational examples of laboratory tests to study CO₂ recovery processes, including diffusion. We also study the change in recovery processes as matrix/fracture dimensions approach field scale.

We recommend using reservoir core or outcrop samples similar to reservoir rock, with dimensions (5-25 in² horizontal area and 10-30 in high). A synthetic model oil can be constructed to mimic PVT properties of the actual reservoir oil, and in particular the minimum miscibility pressure (MMP) as defined by a traditional 1D multi-contact displacement process – MMP_{1D} , reduced gas-oil interfacial tensions (IFT) and oil-gas density differences. The core should be placed in a container with annular space representing the fracture. CO₂ is injected at various rates into the annular space at relevant reservoir pressures, both above and below the MMP_{1D} .

In this work, the effect of several key parameters will be studied – matrix permeability, matrix block size, CO₂ injection rate and reservoir pressure. One of the key results is the effect of diffusion on oil recovery, and how it varies with matrix block size and CO₂ injection rate.

7.2 Description of Matrix/Fracture Models

7.2.1 Haft Kel Field-Scale Model

For the Haft Kel field-scale matrix/fracture system, a single matrix block surrounded by fractures was used to study compositional mass exchange and recovery mechanisms. Significant compositional variations develop within the matrix block, resulting in high recoveries (chapter 6).

Haft Kel petrophysical properties and initial fluid compositions are taken from Saidi (1987). The matrix is represented by an 8-ft cube with 0.8 md isotropic permeability and default fracture width of 0.01 ft (0.30 cm) having 100 D permeability. Due to the matrix block symmetry, only half of the matrix block is modeled. A 2D Cartesian grid is used where the matrix block is surrounded by two horizontal fractures on the top and bottom and one vertical fracture on the right side of the matrix block.

The matrix block is initially filled with oil and the fractures are initialized with injection gas. Zero capillary pressure and high permeability of the fractures means that viscous forces are negligible compared to gravity and capillary forces

in the matrix. Injection rate was investigated using production and gas injection wells at the bottom and top fracture, respectively. The production well is pressure controlled and the injection well is rate controlled. Conceptually we are looking at a matrix block located at the no-flow boundary between an injector and a producer where lateral pressure gradients are negligible. All models use an 11x1x102 ($N_x N_y N_z$) grid where the I=1-10 and K=2-101 grid cells represent a half matrix block.

Eclipse 300 is used for all simulations. An 11-component tuned SRK (Soave-Redlich-Kwong) equation of state (EOS) describes phase and volumetric behavior; the Lorenz-Bray-Clark correlation, tuned to viscosity data, is used to calculate viscosities. EOS component properties and binary interaction parameters (BIPs) are given in Tables 6.2 and 6.3 Unfortunately, CO₂-oil PVT data were not available to tune the EOS model, thereby making CO₂-oil phase behavior predictions somewhat uncertain.

7.2.2 Laboratory Model.

For the laboratory test simulations, a 2D Cartesian grid is used, where the core is surrounded by horizontal fractures on the top and bottom, and one vertical fracture on the right side of the core. Fine gridding is needed for CO₂ injection (chapter 6). The core has a square 0.2x0.2-ft top and bottom surface shape with a total core height of 2 ft (60.96 cm). Core permeability was 0.8 md and porosity was 10%.

A simple, synthetic oil consisting of methane (C₁) and normal pentane (n-C₅) was used, this synthetic oil having similar MMP_{1D} as the Haft Kel reservoir oil, about 1400 psia. EOS component properties and BIPs of the synthetic oil are given in **Tables 7.1** and **7.2**.

**Table 7.1 – Fluid Properties for The 3 Component SRK
Characterization**

Component	MW	Tc, °R	Pc, psia	ω	Vshift	Zc	Parachor
CO2	44.01	547.42	1069.51	0.225	0.217	0.27433	80.00
C1	16.04	343.01	667.03	0.011	-0.002	0.2862	71.00
n-C5	70.91	846.25	503.20	0.229	0.119	0.27119	205.17

**Table 7.2 – Binary Interaction Coefficients for The 3 Component SRK
Characterization**

	CO2	C1	n-C5
CO2	-		
C1	0.1200	-	
n-C5	0.1500	0.0000	-

Capillary pressure and relative permeability of the Haft Kel and lab models are similar, taken from Saidi (1987). Laboratory capillary pressures were scaled with gas-oil IFT by Eq. (2.24) where the gas-oil laboratory IFT, equal to 10 mN/m. Relative permeabilities were not scaled with IFT.

Oil and gas effective diffusion coefficients are given in **Table 7.3** and **7.4**. Gas diffusion coefficients were determined from equilibrium gas at bubble point pressure. More details of diffusion coefficient calculation are given in section (2.2). Liquid density of C₁-n-C₅ mixture was 427.91 kg/m³ at 1500 psia which led to the liquid diffusion coefficients in Table 7.3. Pressure and composition dependency of diffusion coefficients was not considered.

**Table 7.3 – Oil Composition for The 3 Component EOS at Different
Saturation Pressures and Diffusion Coefficients**

Component	1000 psia			1250 psia			1500 psia		
	X _i mole fr.	D _{io} cm ² /s	D _{ig} cm ² /s	X _i mole fr.	D _{io} cm ² /s	D _{ig} cm ² /s	X _i mole fr.	D _{io} cm ² /s	D _{ig} cm ² /s
CO2	0.0000	1.54E-05	2.25E-04	0.0000	1.65E-05	1.75E-04	0.0000	1.81E-05	1.39E-04
C1	0.2735	1.99E-05	2.92E-04	0.3419	2.01E-05	1.13E-04	0.4099	2.07E-05	9.03E-05
n-C5	0.7265	1.99E-05	2.92E-04	0.6581	2.01E-05	1.13E-04	0.5901	2.07E-05	9.03E-05

T_{exp} = 185 °F

Table 7.4 – Oil Composition for The 11 Component EOS at Different Saturation Pressures and Diffusion Coefficients

Component	1000 psia			1250 psia			1500 psia		
	X _i mole fr.	D _{ig} cm ² /s	D _{io} cm ² /s	X _i mole fr.	D _{ig} cm ² /s	D _{io} cm ² /s	X _i mole fr.	D _{ig} cm ² /s	D _{io} cm ² /s
N2	0.0004	2.34E-03	3.63E-05	0.0009	1.84E-03	3.42E-05	0.0011	1.49E-03	3.26E-05
CO2	0.0039	1.72E-03	2.44E-05	0.0043	1.35E-03	2.31E-05	0.0043	1.09E-03	2.20E-05
H2S	0.0133	1.70E-03	2.49E-05	0.0130	1.33E-03	2.36E-05	0.0128	1.08E-03	2.25E-05
C1	0.2211	1.57E-03	3.42E-05	0.2957	1.22E-03	3.10E-05	0.3113	9.90E-04	2.83E-05
C2	0.0494	1.62E-03	2.46E-05	0.0497	1.27E-03	2.32E-05	0.0496	1.03E-03	2.21E-05
C3	0.0542	1.28E-03	1.87E-05	0.0506	1.00E-03	1.77E-05	0.0499	8.14E-04	1.69E-05
C4-C6	0.1428	9.77E-04	1.34E-05	0.1282	7.65E-04	1.28E-05	0.1251	6.23E-04	1.23E-05
C7-C14	0.3761	6.57E-04	1.07E-05	0.3343	5.15E-04	1.04E-05	0.3257	4.20E-04	1.01E-05
C15-C21	0.0998	4.60E-04	6.82E-06	0.0887	3.60E-04	6.48E-06	0.0864	2.93E-04	6.20E-06
C22-C29	0.0299	3.69E-04	5.17E-06	0.0266	2.89E-04	4.90E-06	0.0259	2.35E-04	4.68E-06
C30+	0.0092	3.00E-04	4.13E-06	0.0082	2.35E-04	3.91E-06	0.0079	1.92E-04	3.74E-06

Tres= 110 °F

Oil recovery factor (RF) is calculated from total average oil saturation S_o in the matrix block using Eq. (3.2).

7.3 CO₂ Displacement Mechanism

In this section we discuss the recovery performance for the laboratory system and for the Haft Kel single matrix block.

7.3.1 Lab Test Recovery Performance

System pressure was 1000 psia (68.95 bara) and CO₂ injection rate was 0.5 cm³/hr. Models were run with and without diffusion. **Fig. 7.1** shows that 100% of the synthetic oil is recovered after 3 days when diffusion is included. Neglecting diffusion reduces recovery to only 12.2 % after 10 days, and leads to a laterally-uniform displacement with final recovery controlled by the vertical balance of capillary and gravity forces. **Fig. 7.2** shows an oil saturation map at 1 day (60% recovery) for the 1000 psia model run with synthetic oil using diffusion. The oil saturation is spatially non-uniform, caused by CO₂ entry into the matrix through a complex process controlled by capillary-gravity drainage and diffusion.

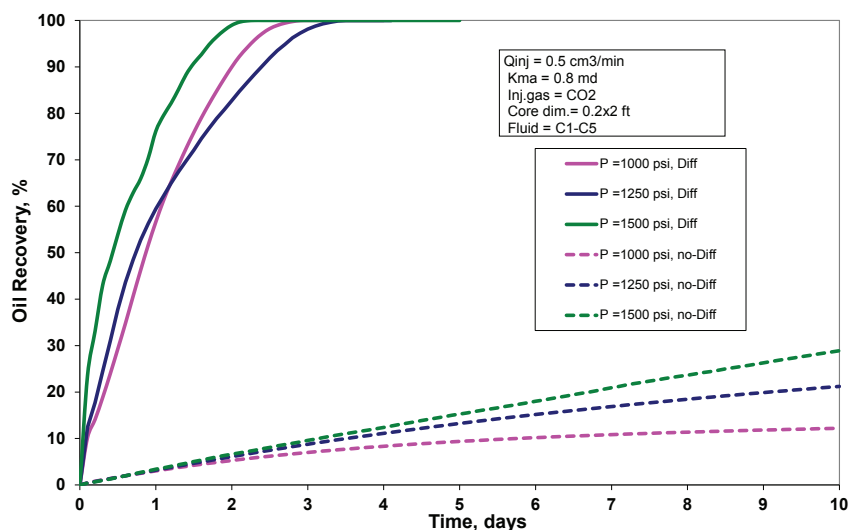


Figure 7.1 – Effect of reservoir pressure on oil recovery vs. time for C₁-C₅ lab system using CO₂ injection with (solid lines) and without diffusion (dash lines).

Fig. 7.3 shows oil recovery performance including diffusion for a lab core saturated with Haft Kel oil¹. The oil recovery and rate of recovery are significantly lower than the synthetic-oil core test. Because of relatively small core dimensions, an important component of oil recovery in laboratory tests will be the *vaporizing-diffusion mechanism (VDM)*. Where gas saturation has been established in the core, CO₂ vaporizes the oil components which are then transported out of the core by diffusion, as fresh CO₂ enters the fracture. The VDM is dominant for synthetic oil systems, but less efficient for real oils which have a large range of heavier components that (a) vaporize less (with lower equilibrium K-values) and (b) diffuse slower in the gas phase, with decreasing efficiency as a function of molecular weight.

The oil saturation profile in Fig. 7.4 shows a saturation map at 16 days (17% recovery) for the 1000 psia lab test model with Haft Kel oil. The *capillary-*

¹ All Haft Kel fluid in lab-test models were run with diffusion, because in the models without diffusion capillary threshold height is larger than the core height and CO₂ will not enter into the core.

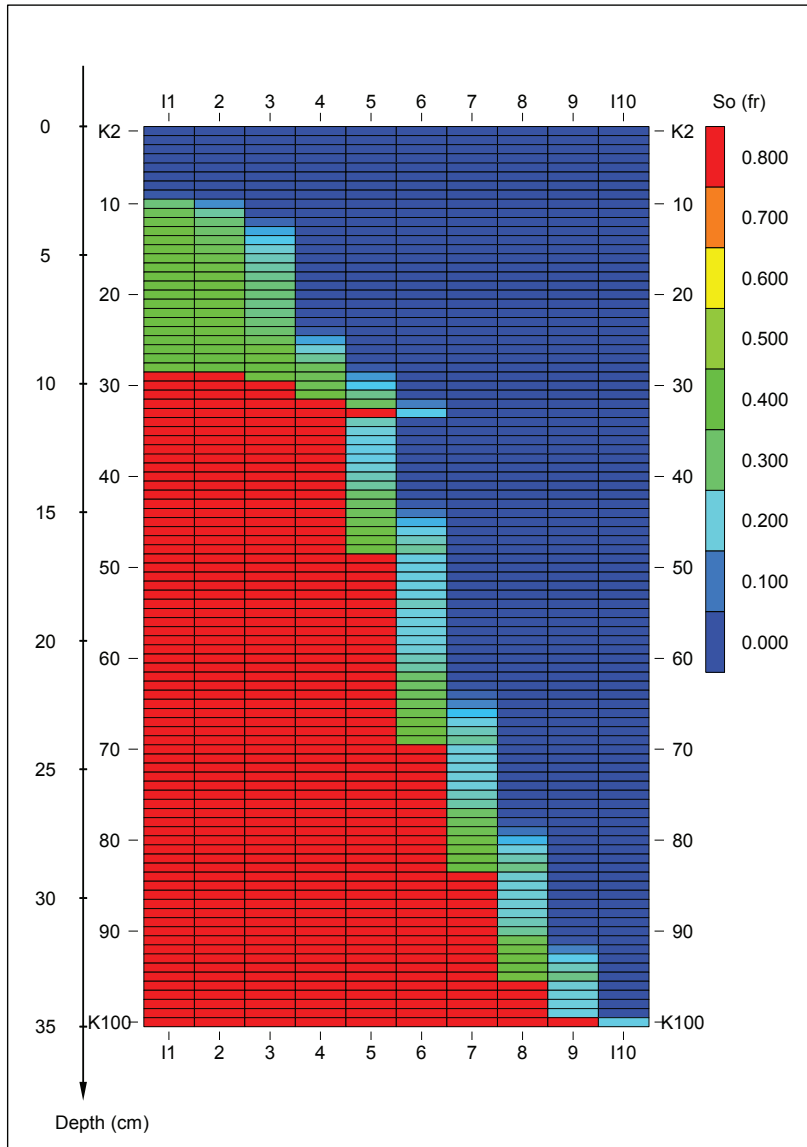


Figure 7.2 – CO₂ gas displacement with diffusion, core oil saturation profile after 1 day for C₁-C₅ lab system at 1000 psia (at about 60% oil recovery).

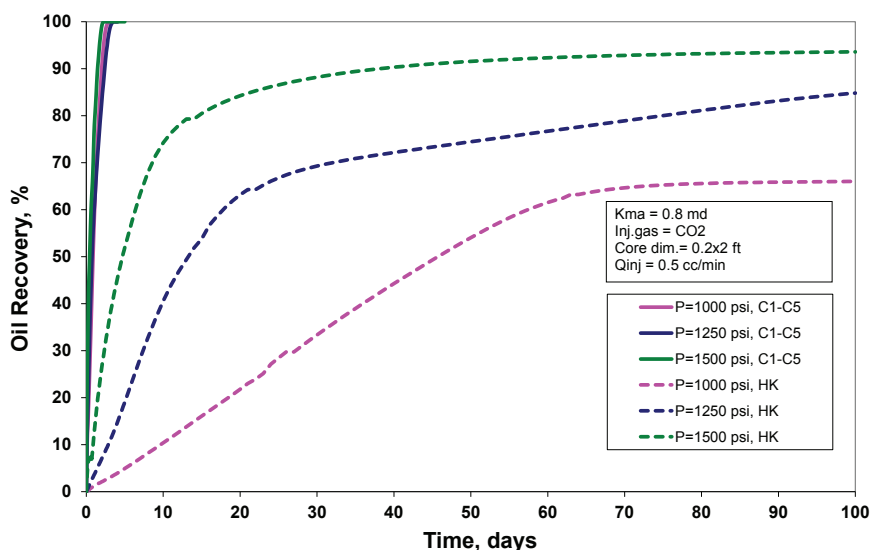


Figure 7.3 – Comparison of reservoir pressure effect on oil recovery vs. time for C₁-C₅ (solid lines) and Haft Kel (dash lines) lab system using CO₂ injection with diffusion.

gravity drive mechanism (CGDM) is more pronounced, with less lateral variations and more-gradual saturation changes than seen with the synthetic oil system. Fig. 7.3 clearly suggests a strong effect of pressure on oil recovery for the Haft Kel oil system, this being linked to strong IFT variations that result from near-critical phase behavior with strong influence of composition and pressure on heavier-component K-values.

7.3.2 Field-Scale (Haft Kel) Recovery Performance

With the reservoir pressure set to 1000 psia (68.95 bara) and CO₂ injection rate of 3 Mscf/D, model runs (with Haft Kel oil) were made with and without diffusion. For the model run without diffusion, near-ultimate recovery of ~22% was achieved after 5 years, as shown with red lines in **Fig. 7.5**. Oil recovery with molecular diffusion was ~72% (near-ultimate recovery) after 10 years. The oil saturation profile shown in **Fig. 7.6**, for the run with diffusion, shows that the

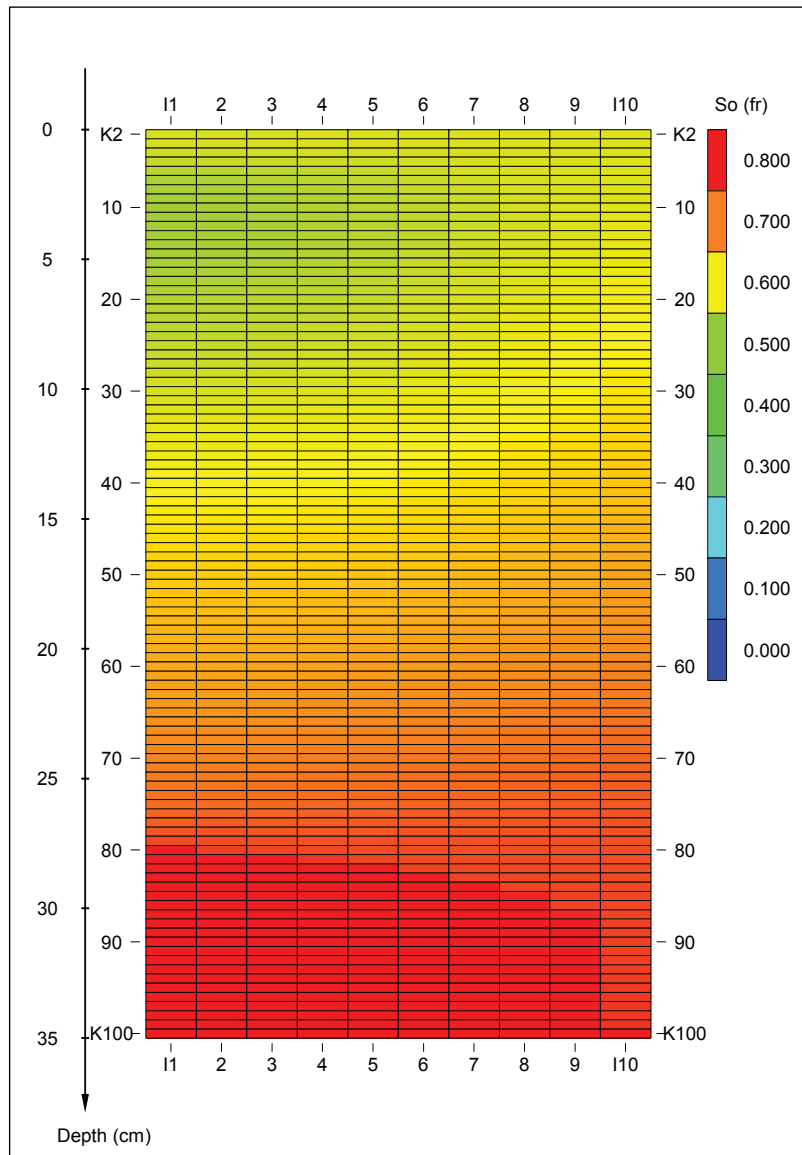


Figure 7.4 – CO₂ gas displacement, oil saturation profile inside core after 16 days for Haft Kel lab system at 1000 psia (at about 17% oil recovery).

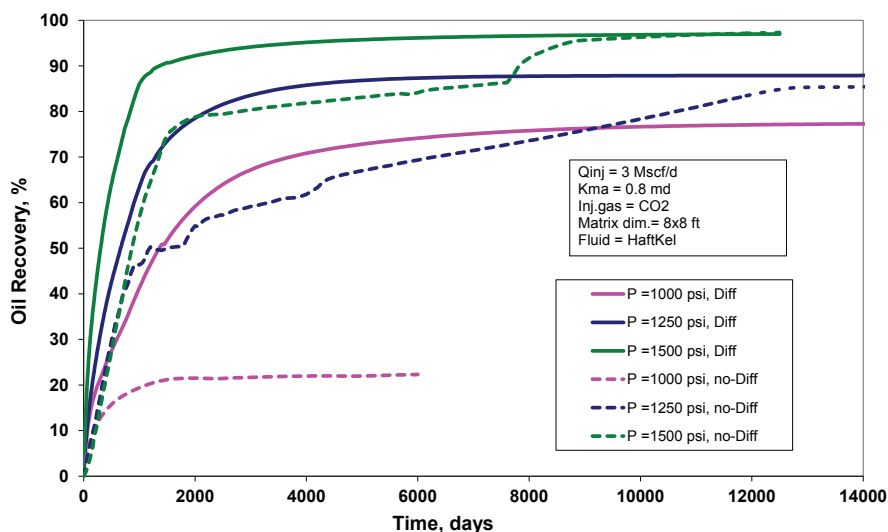


Figure 7.5 – Effect of reservoir pressure on oil recovery vs. time for 8-ft cube Haft Kel single matrix block system using CO₂ injection with (solid lines) and without diffusion (dash lines).

displacement front is laterally non-uniform (somewhat similar to the lab test with Haft Kel oil seen in Fig. 7.4).

7.4 Reservoir Pressure Sensitivity

In this section we study the effect of reservoir pressure on lab- and field-scale systems – at 1000, 1250 and 1500 psia. For each pressure the matrix block/core is initialized with saturated oil and the fracture is initialized with CO₂. Matrix properties, injection rate, and gridding are the same as described above model for the lab- and field-scale models, respectively.

7.4.1 Core Model

The simple C₁-C₅ oil recoveries are 100% after short time (2-3 days) for all pressures (Fig. 7.1). The vaporizing-diffusion mechanism is very effective for this system. For Haft Kel reservoir oil however, the ultimate recovery and the rate of recovery increase significantly with pressure in the lab-test model with

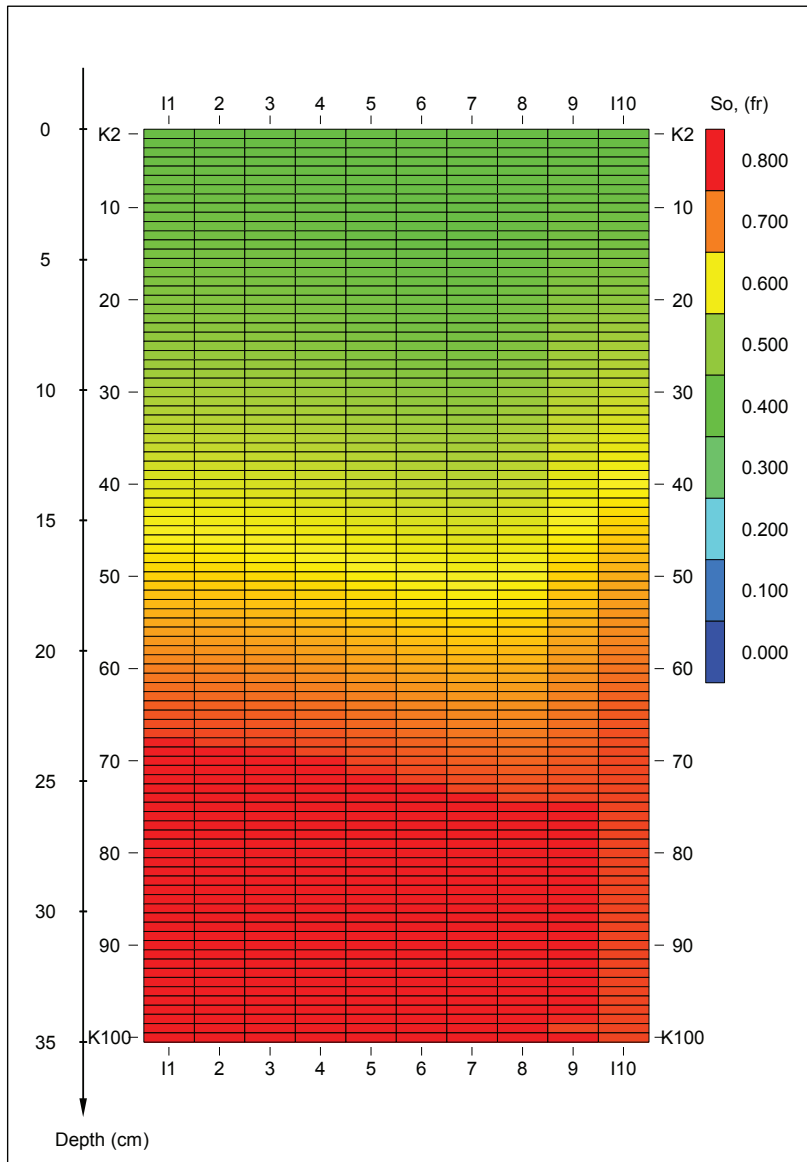


Figure 7.6 – CO₂ gas displacement, matrix block oil saturation profile after 300 days for 8-ft cube Haft Kel single matrix block system at 1000 psia (at about 21.5 % oil recovery).

reservoir oil, as shown in Fig. 7.3. The same conclusion was reported by Er, Babadagli and Zhenghe (2010).

7.4.2 Field-Scale Matrix

For the Haft Kel field-scale single matrix block model, a similar ultimate recovery was found with and without diffusion, for 1250 and 1500 psia, though rate of recovery is much higher with diffusion. For 1000 psia reservoir pressure, the ultimate recovery with diffusion is 78% vs. 22% without diffusion – mainly because CO₂ is able to penetrate the matrix below the threshold capillary height. For all simulations including diffusion, the total recovery and the rate of recovery increase with increasing pressure (Fig. 7.5).

Cases with diffusion show that CO₂ recovers oil below the capillary threshold height, and that unrecovered oil saturation decreases with increasing reservoir pressure (Fig. 7.7). Higher pressures result in more vaporization, with vaporized oil components being transported by gas diffusion from the matrix block. Detailed displacement mechanisms of models with no diffusion (capillary-gravity drive) are previously in chapter 6. Thus mechanism would only be dominant in field with very large matrix blocks where diffusion is insufficient.

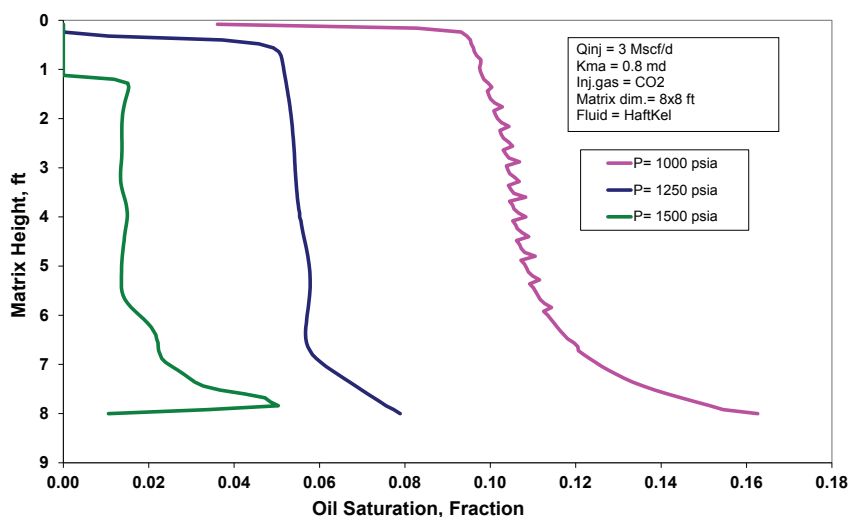


Figure 7.7 – Oil saturation profile for 8-ft cube Haft Kel single matrix block using CO₂ injection gas at 10000 days.

7.5 Matrix Block Permeability Sensitivity

We studied the effect of matrix block permeability for the field-scale Haft Kel system at pressures of 1000, 1250 and 1500 psia, including diffusion. Two matrix block permeabilities were used, 0.8 and 5 md. For each pressure the matrix block is initialized with saturated oil and the fracture is initialized with CO₂. All models are run with an 11x1x102 grid. Injection rate is 3 Mscf/D.

The rate of oil recovery increases with increasing matrix block permeability for all reservoir pressures, but ultimate oil recovery is not affected significantly, as shown in **Fig. 7.8**. Similar results were obtained for models with no diffusion (Section 6.8).

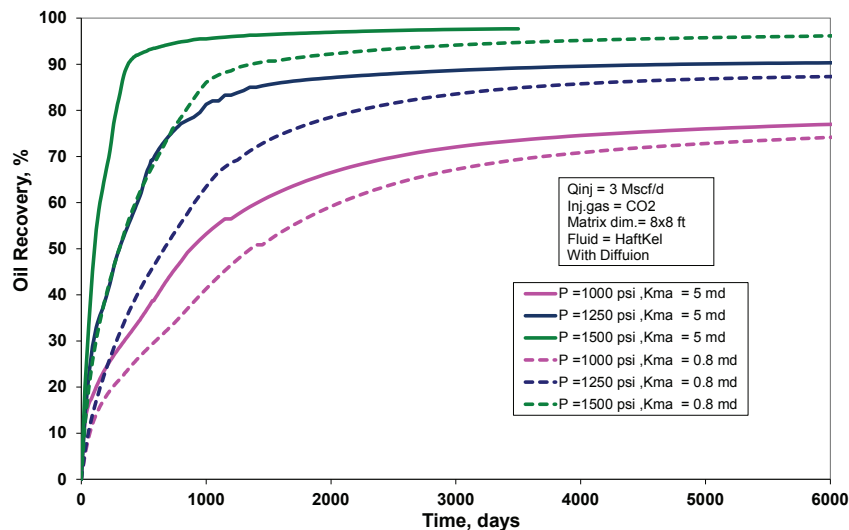


Figure 7.8 – Effect of matrix block permeability on oil recovery vs. time for 8-ft cube Haft Kel single matrix block using CO₂ injection gas at various system pressure.

7.6 Matrix Block Size Sensitivity

We consider cubic matrix blocks with dimensions of 8-, 16- and 35 ft. Models were run with system pressure of 1000 and 1500 psia using 0.8 md matrix block permeability. For each case the matrix block is initialized with saturated oil at system pressure, and the fracture is initialized with CO₂. All models use the

11x1x102 grid. Injection rate is 3 Mscf/D. Cases are run with and without diffusion.

Fig. 7.9 shows recovery performance at 1000 psia, comparing behavior with and without diffusion for different matrix blocks sizes. Higher recoveries (>50%) result mainly from the vaporizing-diffusion mechanism. For the larger matrix block size of 35 ft we see that VDM is a slower, less-effective recovery process, with similar recovery performance with and without diffusion. For the smaller matrix block size of 8 ft we see that VDM is a fast and efficient recovery process; without diffusion, much lower ultimate oil recovery results because remaining oil trapped by capillary-gravity equilibrium cannot be recovered.

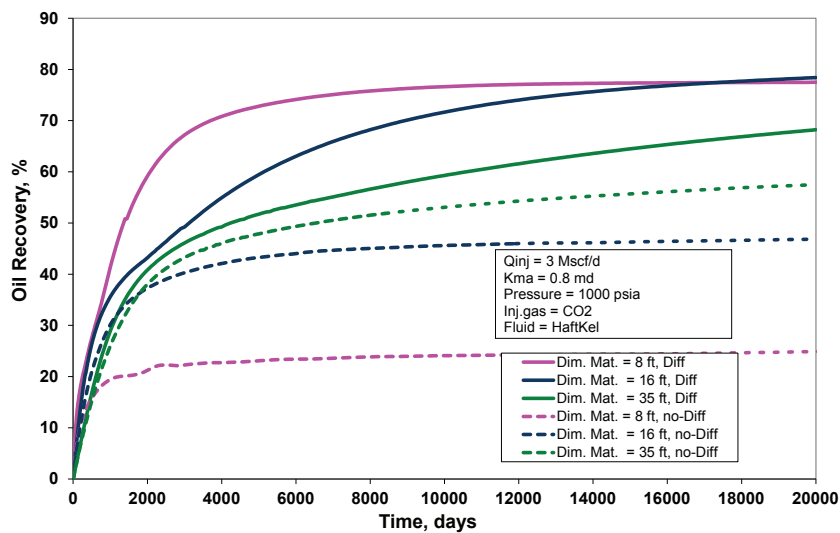


Figure 7.9 – Effect of matrix block dimension on oil recovery vs. time for Haft Kel single matrix block using CO₂ injection gas at system pressure of 1000 psia.

Fig. 7.10 shows recovery performance at 1500 psia, comparing behavior with and without diffusion for different matrix blocks sizes. We see that capillary-gravity drive is more significant for all cases, with smaller and larger matrix block sizes. The impact of diffusion is much less, yielding only a slight acceleration in recoveries. IFTs become very low at 1500 psia through CO₂-oil

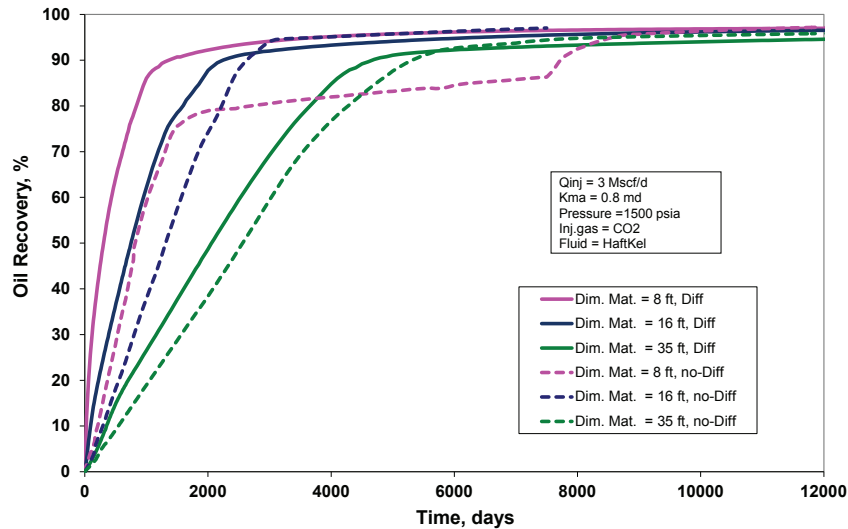


Figure 7.10 – Effect of matrix block dimension on oil recovery vs. time for Haft Kel single matrix block using CO₂ injection gas at system pressure of 1500 psia.

interaction and near-critical phase behavior, reducing capillary retaining forces significantly.

Figs. 7.9 and 7.10 clearly show that the relative importance of vaporizing-diffusion recovery and capillary-gravity drainage recovery can vary significantly, according to pressure (phase behavior effects) and matrix block size.

7.7 Injection Rate Sensitivity

Availability of fresh CO₂ in fractures surrounding the matrix block has a large impact on total fracture/matrix mass transfer, and consequently the rate of oil recovery. CO₂ injection rate is investigated for both lab-scale and field-scale systems.

For the lab scale model, 0.8 and 5 md core are considered. System pressure is 1000 psia. CO₂ injection rates of 0.5, 0.1 and 0.03 cm³/min injection rates are used. Cases with and without diffusion are studied.

For the field-scale simulations, we consider an 8-ft cubic matrix block with system pressure of 1000 and 1500 psia. Matrix block permeability is 0.8 md. For

each pressure the matrix block is initialized with saturated oil, and the fracture is initialized with CO₂. For the case with 1000 psia reservoir pressure, three injection rates are used: 3, 0.3 and 0.03 Mscf/D, while for 1500 psia reservoir pressure, two injection rates are used: 3 and 0.3 Mscf/D.

As seen in **Figs. 7.11, 7.12 and 7.13** diffusion has a huge effect on rate of recovery for lab-scale simulations. Oil recoveries are delayed dramatically by decreasing injection rate. The lack of fresh CO₂ slows down the vaporizing-diffusion mass transfer mechanism.

The strong dependence of recovery on diffusion in lab core test leads to an important lab-design potential. Using lab oil systems with 3-5 pure components representing oil can provide component production data that is useful to verify the model's capability to describe the VDM accurately. As the synthetic oil composition is changed, the overall recovery mechanism can also be altered to move from VDM to a mixed VDM/CGDM mechanism.

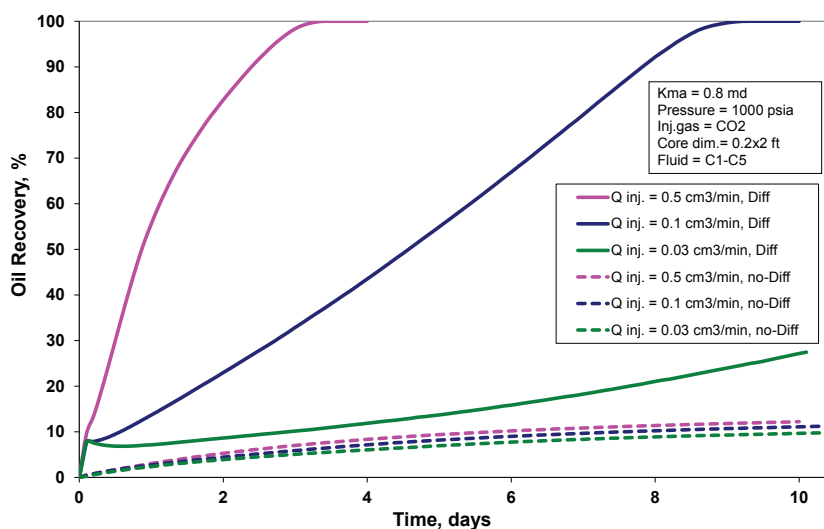


Figure 7.11 – Effect of injection rate on 0.8 md core during CO₂ gas injection for C₁-C₅ lab system at 1000 psia.

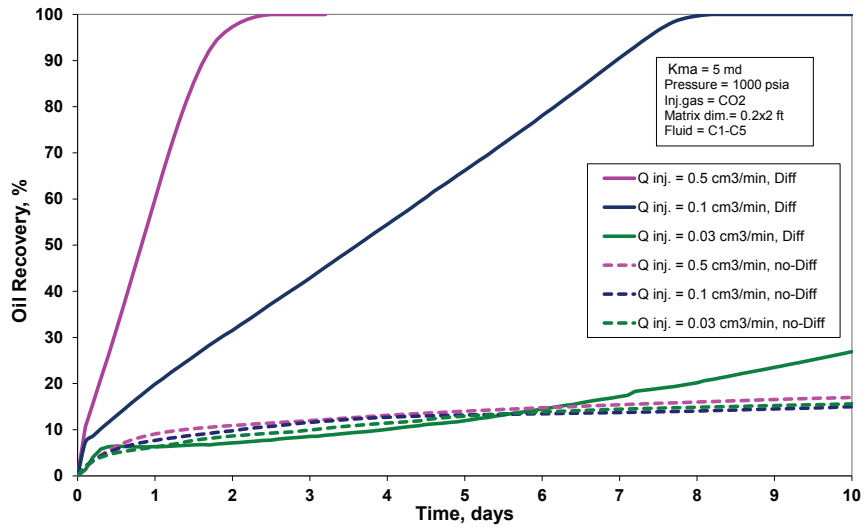


Figure 7.12 – Effect of injection rate on 5 md core during CO₂ gas injection for C₁-C₅ lab system at 1000 psia.

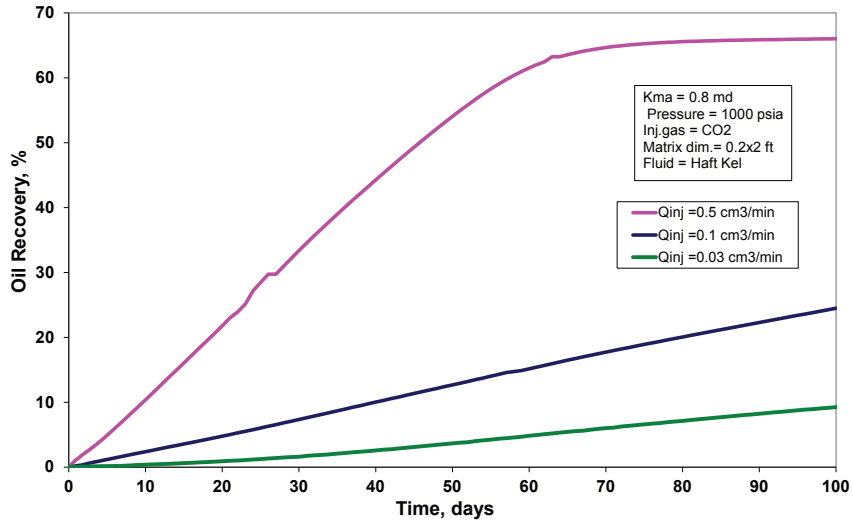


Figure 7.13 – Effect of injection rate on 0.8 md core during CO₂ gas injection for Haft Kel lab system at 1000 psia.

For a single matrix block in the field-scale simulations, CO₂ injection rate of 3 and 0.3 Mscf/D give similar results, though the rate of recovery is somewhat slower for 0.3 Mscf/D. A dramatic decrease in the rate of recovery is seen for 0.03 Mscf/D at 1000 psia.² Results are shown in Figs. 7.14 and 7.15. It is clear that the actual distribution, movement, and composition of gas in the fractures of a naturally-fractured reservoir will not be as simple as modeled in this study.

We have only considered the potential adverse effect of low CO₂ “injection rate” – i.e. conditions whereby the fracture is not replenished continuously with fresh CO₂. The modeling of CO₂ concentration in the fracture system needs to be studied further, as reduced CO₂ concentrations will reduce the effectiveness of both vaporizing-diffusion and capillary-gravity drainage processes.

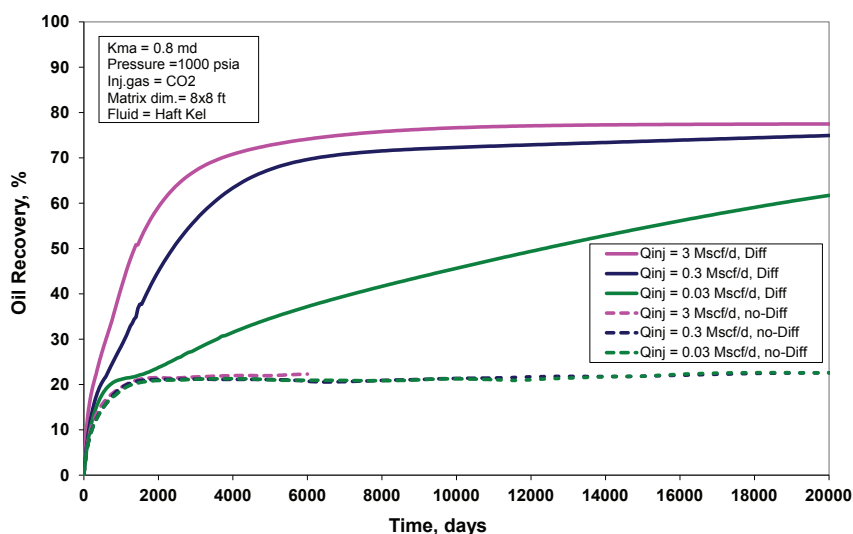


Figure 7.14 – Effect of injection rate on 0.8 md single matrix block during CO₂ gas injection for 8-ft cube Haft Kel system at 1000 psia.

² Gas injection rate of 0.03 Mscf/D at 1500 psia resulted in unstable simulation results, and are therefore not presented here.

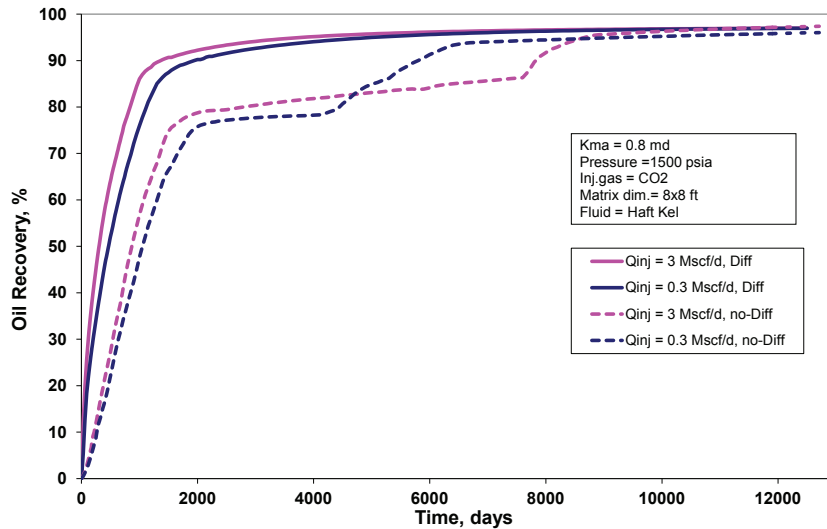


Figure 7.15 – Effect of injection rate on 0.8 md single matrix block during CO₂ gas injection for 8-ft cube Haft Kel system at 1500 psia.

7.8 Conclusions

Conclusions from our numerical model studies include:

1. Diffusion has a significant acceleration effect on oil recovery for all cases studied. The impact is related to (a) vaporized heavier components extracted from the oil and transported from matrix to fracture by diffusion, and (b) CO₂ movement into the matrix block, with subsequent effect on IFT and, thereby, capillary-gravity, and capillary-induced displacement.
2. Ultimate oil recovery increases by CO₂ injection with increasing reservoir pressure in a single matrix block fractured system.
3. Ultimate oil recovery is independent of pressure for the synthetic C₁-C₅ oil studied for lab-scale systems in the range of 1000-1500 psia (with thermodynamic MMP ~1400 psia).

4. Oil recovery rate is affected by CO₂ injection (replenishment) rate, mainly because the vaporizing-diffusion process is slowed, but also because IFT changes are lessened.

7.9 References

- Er, V., Babadagli, T and Zhenghe X. 2010. Pore-Scale Investigation of the Matrix-Fracture Interaction during CO₂ Injection in Naturally Fractured Oil Reservoir. *Energy Fuels* 2010, 24: 1421-1430.
- Saidi, A.M.1987. *Reservoir Engineering of Fractured Reservoirs*. TOTAL Edition Press, Paris, P 764-770.
- Schlumberger: *ECLIPSE 300* Reservoir Engineering Software. 2009. www.slb.com.

Appendix A

Simulator Input Data Sets

Input Data Set Used to Model Karimaie Experiment in
Chapter 3
SENSOR input data set

Note:

Compositional production of well streams were processed using *Pipe-it/Steamz* with separator varying with time (section 3.6.4 and Table 3.5).


```

TITLE
  Simulating Chalk core done by Hassan
  Experiment 4 in page 128
  Full radial block model
  4 Component EOS
  Base:
    Nx = 10
    Nz = 50
    Kma = 5.0 md
    Hma = 19.6 cm= 0.643 ft
    Porosity= 0.44-0.48
    Matrix diameter = 3.8 cm =0.12467154 ft
    Pinit = 220 bara=3190.83 psia
    Inj gas = Eq gas
    No blocks = 1
    Displacement=2D
ENDTITLE

C -----
C Dimension and Solution Options
C -----

GRID  10 1 51

CPU

  IMPLICIT

MAPSX 1 1 2 3
MAPSY 1 1 2 3
MAPSPRINT 1 X Y P SO SG GG GO TENS TX TZ PV PCGO VISO ! Initialization output

C -----
C Grid Block Properties
C -----
RADIAL
  5 ! equal volume block option
  0.006233577 0.06889743 ! Nx-1 equal vol blocks to 0.060695 ft + 1 annulus block
  360
DEPTH CON
  1000
THICKNESS ZVAR
  0.00328083 48*0.013396723 0.001640415 0.001640415
KX CON
  100000
MOD
  1 10 1 1 1 51 = 26.25560264 ! 16.71049
  1 9 1 1 2 49 = 5

KY EQUALS KX
KZ EQUALS KX

POROS CON
  1.00
MOD
  1 10 1 1 1 51 = 0.936092035
  1 9 1 1 2 49 = 0.44468662
C -----
C Regions: Region 1 = Matrix, Region 2 = Fracture
C -----

ROCKTYPE CON ! Rock (saturation table) regions
  2
MOD
  1 9 1 1 2 49 = 1

REGION CON ! Fluid in place regions
  2
MOD
  1 9 1 1 2 49 = 1

INITREG CON ! Initialization regions
  2
MOD
  1 9 1 1 2 49 = 1
C -----

```

```

C Rel-perm and capillary pressure data
C -----

! Rock type 1 (Matrix-Chalk)
KRANALYTICAL 1
0.0 0.0 0.050799489 0.0 ! Swc Sorw Sorg Sgc 0.10557
1.0 1.0 1 ! krw(Sorw) krg(Swc) kro(Swc)
1.0 1.0 1.0 1.0 ! nw now ng nog
0.087 2.088 3.337 PCGO ! c1 c2 c3 gas-oil (C1-nC5 Pc) , ref=1.5

! Rock type 2 (Fracture, Pc = 0)
KRANALYTICAL 2
0.0 0.0 0.0 0.0 ! Swc Sorw Sorg Sgc
1.0 1.0 1.0 ! krw(Sorw) krg(Swc) kro(Swc)
1.0 1.0 1.0 1.0 ! nw now ng nog
! Interfacial tension scaling
TENSION 1.5 300 ! ref_tension, max_tension

C -----
C Fluid PVT data
C -----

PVTEOS SRK
185 ! Reservoir temperature (deg F)

CPT MW TC PC ZCRIT SHIFT AC PCHOR OMEGA OMEGB
C1 16.043 343.01 667.03 0.2862 -0.00247 0.011 64.23 0.42748 0.08664
n-C7 100.2 972.36 397.4 0.2611 0.14347 0.35 281.33 0.42748 0.08664
CO2 44.01 547.42 1069.5 0.27433 0.21749 0.225 80 0.42748 0.08664
N2 28.014 227.16 492.84 0.29178 -0.0009 0.037 59.1 0.42748 0.08664

BIN
0.01574 0.12 0.02
0.15 0.08
0

C -----
C Initialization
C -----

INITIAL 1
! depth psat C1 n-C7 CO2 N2
DEPTH
1000 3190.83 0.684404 0.315596 0.0000 0.0000
PINIT 3190.83
ZINIT 1000

INITIAL 2
! depth psat C1 n-C7 CO2 N2
DEPTH
1000 3190.83 0.684404 0.315596 0.0000 0.0000
PINIT 3190.83
ZINIT 1000
ENDINIT

C we can define well under one keyword or separate them to each well
WELL
I J K PI
PROD
1 1 51 1 !name of oil produce well
2 1 51 1 ! perforated location
3 1 51 1
4 1 51 1
5 1 51 1
6 1 51 1
7 1 51 1
8 1 51 1
9 1 51 1

GINJ
1 1 1 1 !name of gas injection well
2 1 1 1 ! perforated location
3 1 1 1
4 1 1 1
5 1 1 1
6 1 1 1
7 1 1 1
8 1 1 1
9 1 1 1

```



```

INJGAS                                !Equilibrium gas
GINJ
0.92857147  0.07142853  0.0000  0.0000
WELLTYPE
  PROD      STBOIL                    !define well type and unit for that
  GINJ      -2                        !Oil producer STB/day
  GINJ      -2                        ! Gas injection well RB/day
RATE
  PROD      200                       !rate of the Gas produce well
  GINJ      0.00905733                !injection rate 1 cm3/min (5 cm3/min=0.045286631 )
  BHP
  PROD      3190.83
  GINJ      319000.83                !BHP of the gas injection well

C -----
C Output specifications
C -----
PSM
MAPSFREQ 1

MAPSFILE SAT SG SO TENS GO GG
MAPSFILEFREQ 1 ! maps written to fort.71
SUMFREQ 1
WELLFREQ 1
WELLSUM
C - Time step control
C   days   freq
TIME     0.0150
RATE
GINJ     0.0035

C   days   freq
TIME     0.080

RATE
GINJ     0.000905733                !injection rate 0.1 cm3/min

TIME     0.1
TIME     4.2     0.1

INJGAS                                !CO2 gas
GINJ
  0.0000  0.0000  1.0000  0.0000
RATE
  GINJ    0.000905733 ! 0.0033                !injection rate 0.364 cm3/min 0.0033

TIME     4.5     0.1

RATE
  GINJ    0.000905733 ! 0.000634013                !injection rate 0.07 cm3/min 0.000634013

DTSTART 0.001
DTMAX 0.001
TIME     6.4     0.1

END

```


Input Data Set Used to Model Darvish Experiment in
Chapter 4
ECLIPSE 300 input data set


```

--RUNSPEC section-----
NOECHO
RUNSPEC
--TITLE
--IMPES
FULLIMP

DIMENS
  10  1  51 /
RADIAL
-- Phases present
OIL
GAS
OPTIONS3
--switch 19  21  26  46  68  74  146
18*  0  1* 200 4*  2  19* 200 21* 1  5*  1  71* 5  11*  1* / 14*  1

--Enables molecular diffusion
DIFFUSE
-- Units
LAB
-- Define Component in EOS
COMPS
13 /
REGDIMS
-- Max.FIPREG  FIPREG
  2  2  0  2/
TABDIMS
--No.sat.tab  No.pvt.tab  max.sat.nods  max.sat.nods  Max.FIPREG
  2  1  50  50  2/
EQLDIMS
----Eqrqn  Deptab
  2  50 /
WELLDIMS
5 10 20 20 20 20/
MISCIBLE
/
-- To unified output files
UNIFOUT
MULTSAVE
0 /
UNIFIN
--Grid section-----
GRID
--Requests output of an INIT file (Need for FloViz)
INIT
RPTGRID
DR DZ PERMR PERMZ PORO PORV TRANR  TRANZ NNC /
MINPORV
0.000000001/
INRAD
0.1E-03/
-- SPECIFY GRID BLOCK DIMENSIONS IN THE R DIRECTION
DRV
0.7666634  0.3175650  0.2436724  0.2054291  0.1809841
0.1636227  0.1504676  0.1400495  0.1315395  0.1999991/ cm
DTHETAV
360.0/
DZV
0.099999698 48*1.2427 2*0.049999849 / cm
EQUALS
  TOPS  1  1 10 1 1 1 1 /
  PORO  0.94  1 10 1 1 1 51 / Fracture porosity0.94
  PORO  0.438  1 9 1 1 2 49 / Martix porosity 0.438  0.444
  PERMR 80  1 10 1 1 1 51 / Fracture permeability 16.2
  PERMR 4  1 9 1 1 2 49 / Martix permeability
/
COPY
  'PERMR'  'PERMTH' / 1 10 1 1 1 51
  'PERMR'  'PERMZ' /
/
GRIDFILE
2 /

PROPS =====
EOS
PR79 /

```

```

-- Reservoir temperatures Deg C
RTEMP
130 /
CNAMEs
N2 CO2 C1 C2 C3 C4 C5 C6 C7-C9 C10-C15 C16-C22 C23-C34 C35+ /

-- Molecular Weights
MW
28.014 44.010 16.043 30.070 44.097 58.123 72.150 84.135 110.403 167.317 244.898 347.728
578.832 /

-- Critical temperatures Deg K
TCRIT
126.20 304.12 190.56 305.32 369.83 416.49 465.10 511.14 577.75 682.95 782.17 874.10 1024.78
/

-- Critical pressures atm
PCRIT
33.5357 72.7757 45.3886 48.0829 41.9245 36.6942 33.3165 31.7778 27.5412 20.4465 15.0670
11.4071 10.0720 /

-- Acentric factors
ACF
0.03700 0.22500 0.01100 0.09900 0.15200 0.19299 0.24053 0.25984 0.32623 0.49183 0.70817
0.97132 1.40544/

-- Critical Z-factors
ZCRIT
0.29178 0.27433 0.28620 0.27924 0.27630 0.27792 0.27032 0.26759 0.25962 0.24406 0.22710
0.20735 0.17549 /

-- Parachors (Dynes/cm)
PARACHOR
59.10 80.00 71.00 111.00 151.00 189.90 229.20 236.92 299.97 436.56 622.75 869.55 1424.20 /

-- Critical Viscosity Z-factors
ZCRITVIS
0.29178 0.29278 0.28620 0.27924 0.27630 0.27792 0.27032 0.29954 0.27966 0.25667 0.24019
0.23267 0.22163 /

-- Parameter EoS Shift Coefficients
SSHIFT
-0.16758 -0.00573 -0.14996 -0.06280 -0.06381 -0.05795 -0.04271 -0.00273 0.02683 0.09061
0.14892 0.18839 0.0726 /

-- Binary Interaction Coefficients
BIC
0.00000
0.02500 0.21000
0.01000 0.26000 0.00000
0.09000 0.25000 0.00000 0.0000
0.09500 0.23492 0.00000 0.0000 0.0000
0.10508 0.23000 0.00000 0.0000 0.0000 0.0000
0.11000 0.23000 0.00000 0.0000 0.0000 0.0000 0.0000
0.11000 0.10425 -0.04464 0.0000 0.0000 0.0000 0.0000 0.0000
0.11000 0.09498 -0.06761 0.0000 0.0000 0.0000 0.0000 0.0000 0.0000
0.11000 0.08535 -0.08963 0.0000 0.0000 0.0000 0.0000 0.0000 0.0000 0.0000
0.11000 0.07660 -0.10795 0.0000 0.0000 0.0000 0.0000 0.0000 0.0000 0.0000 0.0000
0.11000 0.06659 0.19401 0.0000 0.0000 0.0000 0.0000 0.0000 0.0000 0.0000 0.0000 0.0000 /

--Interfacial tension scaling
MISCSTR
--ref_tension, max_tension
1.5 300 10/
-- (IFT.ref/IFT)^n; n=1
MISCEXP
0/

SGOF
--Sg Krg Krog Pcog (atm)
0.0000 0.0000 1.0000 0.0000
1.0000 1.0000 0.0000 0.0000
/ --table 1 (fracture)
0.0000 0.0000 1.0000 0.0000
0.0500 0.0500 0.9500 0.0059
0.1000 0.1000 0.9000 0.0060
0.1500 0.1500 0.8500 0.0062

```

```

0.2000 0.2000 0.8000 0.0066
0.2500 0.2500 0.7500 0.0073
0.3000 0.3000 0.7000 0.0085
0.3500 0.3500 0.6500 0.0102
0.4000 0.4000 0.6000 0.0126
0.4500 0.4500 0.5500 0.0158
0.5000 0.5000 0.5000 0.0200
0.5500 0.5500 0.4500 0.0252
0.6000 0.6000 0.4000 0.0318
0.6500 0.6500 0.3500 0.0397
0.7000 0.7000 0.3000 0.0491
0.7500 0.7500 0.2500 0.0603
0.8000 0.8000 0.2000 0.0734
0.8500 0.8500 0.1500 0.0885
0.9000 0.9000 0.1000 0.1059
0.9500 0.9500 0.0500 0.1253
1.0000 1.0000 0.0000 0.1480
/ --table 2 (Matrix)

DIFFAGAS
-- N2 CO2 C1 C2 C3 C4 C5 C6 C7-C9
C10-C15 C16-C22 C23-C34 C35+ (cm2/hr)
0.186 1.151 0.971 0.943 0.884 0.753 0.651 0.590 0.511 0.377 0.276 0.206 0.155 /-new
EOS

DIFFAOIL
-- N2 CO2 C1 C2 C3 C4 C5 C6 C7-C9
C10-C15 C16-C22 C23-C34 C35+ (cm2/hr)
0.011 0.027 0.029 0.027 0.022 0.018 0.016 0.014 0.012 0.010 0.008 0.006 0.005 / New
EOS

REGIONS =====
-- Regoin 2= Matrix
-- Regoin 1= Fracture
EQUALS
FIPNUM 1 / Fluid In Place reg. no.
FIPNUM 2 1 9 1 1 2 49 / Fluid In Place reg. no.
SATNUM 1 / Saturation reg. no.
SATNUM 2 1 9 1 1 2 49 / Saturation reg. no.
EQLNUM 1 /
EQLNUM 2 1 9 1 1 2 49 /
/

SOLUTION =====
DATUMR
1.0 1.01 /
PRESSURE
510*296.077 / atma
EQUALS
SWAT 0/
SOIL 0.0/
SOIL 1.0 1 9 1 1 2 49/
/
NEI
0.00 1.00 0.00 0.00 0.00 0.00 0.00 0.00 0.00 0.00 0.00 0.00 0.00 /
0.0012 0.0085 0.4480 0.0767 0.0426 0.0318 0.0220 0.0211 0.0797 0.0986 0.0652 0.0538 0.0509 /

RPTSOL
PRESSURE SOIL SGAS PCOG PSAT XMF YMF /

RPTRST
BASIC=2 SOIL PCOG /

SUMMARY =====
--data be written to the Summary file only at report time
RPTONLY
-- *****
-- * PSM SUMMARY include file *
-- *****
--INCLUDE
--'REZA_PSM.SUMMARY' /
RUNSUM
--ALL
FOPR

```

```

FOPT
FGPT
FOMT
FOMR
FGMT
FGMR
--FONPT
--FGNPT
--/
FOE
ROE
/
/
ROSAT
/
/
ROIP
/
/
ROIPL
/
/
RUNSUM
EXCEL

SCHEDULE =====
----- THE SCHEDULE SECTION DEFINES THE OPERATIONS TO BE SIMULATED
-----
--Define Separator condition
SEPCOND
LABSEP      ' '          1   130  296.077 /
/
WELSPEDS
PROD Field 1 1 1* GAS /
GINJ Field 1 1 1* GAS /
/
WSEPCOND
PROD LABSEP /
/

WCONPROD
--Wellname  status  control  oil-s.rate  wat-s.rate  gas-s.rate  liq-s.rate  res.rate  BHP
--Unit      stb/d      stb/d      stb/d      stb/d      rcm3/hr    atma
PROD        OPEN    BHP        4*
/

WCONINJE
--Wellname  type  status  control  Surf.rate  res.rate  BHP
--Unit      GAS  OPEN    RESV     cm3/hr    rcm3/hr   atma
GINJ        GAS  OPEN    RESV     1*        6.00     2900/
/

-- defining gas injection composition
WELLSTRE
--well St.name  Z-C1      Z-nC7      Z-CO2      Z-N2
CO2-gas         0.000    1.00    0.00    0.00    0.000    0.000    0.00    0.00    0.000    0.000
0.00    0.000    0.00 / 0.00
/

WINJGAS
-- Well name  Stream  Stream name
GINJ         STREAM  CO2-gas/
/

WELLCOMP
--Well name  I  J  K1  K2  SatTable
PROD         1  1  51  51  1*  0.00010 /
PROD         2  1  51  51  1*  0.1999985 /
PROD         3  1  51  51  1*  0.1999985 /
PROD         4  1  51  51  1*  0.1999985 /
PROD         5  1  51  51  1*  0.1999985 /
PROD         6  1  51  51  1*  0.1999985 /
PROD         7  1  51  51  1*  0.1999985 /
PROD         8  1  51  51  1*  0.1999985 /
PROD         9  1  51  51  1*  0.1999985 /
GINJ         1  1  1  1  1*  0.00010 /
GINJ         2  1  1  1  1*  0.1999985 /
GINJ         3  1  1  1  1*  0.1999985 /
GINJ         4  1  1  1  1*  0.1999985 /
GINJ         5  1  1  1  1*  0.1999985 /

```



```
GINJ      6  1  1  1  1*  0.1999985  /
GINJ      7  1  1  1  1*  0.1999985  /
GINJ      8  1  1  1  1*  0.1999985  /
GINJ      9  1  1  1  1*  0.1999985  /
/
-- Creat Restart file
RPTRST
  BASIC=2  SOIL/
RPTPRINT
8*/
RPTSCHED
'CPU=1'  'FIP=3'  'SOIL' XFW FUGG  FUGO  'ZMF'  XMF YMF PRES  PCOG  KRO KRG /

--TUNING
--8* /
--4* /
--20 1* /20  1*  2*20
-- Uint= Hr

TSTEP
1.0 /
WCONINJE
--Wellname  type  status  control  Surf.rate  res.rate  BHP
--Unit
GINJ      GAS  OPEN    RESV    1*        6.00     2900/
/
--TSCRIT
--0.001 0.001  0.1 /
-- Uint= Hr
TSTEP
539*1 /
--1/
END
```


Input Data Set Used to Tune EOS of Darvish Experiment
in Chapter 4
Phase Comp input data set


```

=====
* PhazeComp file generated by PhzGUI 9/3/2009
=====

TEST1 ALL ; Automatic stability test of all single-phase solutions
TEST2 ALL ; Automatic stability test of all two-phase solutions
STAB ON

VARIABLE DUMMY 1.0 0.9999 1.001 ; Ensures that a REG file is generated by post-processor

-----
; Initial Definition of Aliases
-----
Define satp 0.000E+0
Define rvol 0.000E+0
Define lrvol 0.000E+0
Define lden 0.000E+0
Define gden 0.000E+0
Define gz 0.000E+0
Define lvis 0.000E+0
Define gvis 0.000E+0
Define mr 0.000E+0
Define gsg 0.000E+0
Define comp 0.000E+0
Define K30 0.000E+0
Define gor 0.000E+0
Define lden_vis 0.000E+0
Define com-vis 0.000E+0
-----
; Char Lab-C10+
-----
CHAR Lab-C10+
EOS PR
Comp Mw
N2
CO2
C1
C2
C3
I-C4
N-C4
I-C5
N-C5
C6 85.48
C7 93.03
C8 106.27
C9 120.99
C10p 1.000

END

-----
; Char SCN-C35+
-----
; Soreide parameters
SOREIDE
Factor 2.570E-1
Sg0 2.900E-1
Mw0 66.000
Exponent 1.570E-1

; Gamma Distribution
GAMMA
Split C10p C10
Shape 9.100E-1
Bound 128.0 ;128.500
Average 293.500
Origin 5.33E-1
END

VARIABLE Cf 2.52194e-01 ; 0.2 0.3 ; 2.570E-1 2.52194e-01
REPLACE SOREIDE Factor BY Cf

; Twu MW damping factor
REPLACE TWUMW by 1.000

CHAR SCN-C35+

```



```

-----
; Char C35+
-----
CHAR      EOS-C35+
Basis     SCN-C35+
EOS       PR
Comp      Mw      Tc      Pc      AF      VS      A      B      Tb
SG        Zc      ZcVisc  Pchor  LMw
          K      K      bar
N2
CO2
C1
C2
C3
C4
C5
C6
C7-C9
C10-C15
C16-C22
C23-C34
C35+

BIPS      N2      CO2      C1      C2      C3      C4      C5      C6
C7-C9     C10-C15  C16-C22  C23-C34  C35+
N2
CO2
C1
C2
C3
C4
C5
C6
C7-C9
C10-C15
C16-C22
C23-C34
C35+
; Lump C5- C1 C2 C3 C4 C5

Variable  VSC7  7.48906e-01  ; -2  2
Variable  VSCO2 -3.00000e+00 ; 1  -3  3

Multiply  VS  of  C7-C9  to  C35+  BY  VSC7
Multiply  VS  of  CO2  BY  VSCO2

END
-----
; FEED Lab-C10+
-----
Restore   Lab-C10+

;      Name      Type      N2      CO2      C1      C2      C3      I-C4
;N-C4   I-C5     N-C5     C6      C7      C8      C9      C10p ; MW+
Mix  SEPG  Moles  2.000E-1  1.370  72.620  12.320  6.480  1.250  2.790
7.700E-1 9.800E-1 7.600E-1 3.400E-1 1.000E-1 1.000E-2 0.000E+0 ; 293.500

Mix  SEPO  Moles  0.000E+0  0.000E+0  3.000E-2  1.800E-1  6.800E-1  3.800E-1  1.380
1.030  1.820  4.100  5.360  8.330  6.560  70.150  ; 293.500

Mix  Recm-oil  Moles  1.200E-1  8.300E-1  44.150  7.560  4.210  9.100E-1
2.240  8.700E-1  1.310  2.070  2.310  3.330  2.580  27.510 ; 293.500  99.170
-----
; CNV Lab-C10+
-----
; Gamma Distribution
GAMMA
Split      C10p      C10
Shape      9.100E-1
Bound      128 ;128.500
Average    293.500
Origin     5.33E-1
END

CONSERVE   Mass

```



```

RESTORE Lab-C10+
MULTIPLY Mass of C10p in SEPG by 293.500
RESTORE SCN-C35+
REPLACE Gamma Average by 293.500
MIX SEPG 1 Mole SEPG

RESTORE Lab-C10+
MULTIPLY Mass of C10p in SEPO by 293.500
RESTORE SCN-C35+
REPLACE Gamma Average by 293.500
MIX SEPO 1 Mole SEPO

RESTORE Lab-C10+
MULTIPLY Mass of C10p in Recm-oil by 293.500
RESTORE SCN-C35+
REPLACE Gamma Average by 293.500
MIX Recm-oil 1 Mole Recm-oil
    
```

; Global weight factors used in regression

```

Define satp 0.000E+0
Define lrvol 0.000E+0
Define lden 0.000E+0
Define gden 0.000E+0
Define gz 0.000E+0
Define lvis 0.000E+0
Define lvis-1 0.000E+0
Define gvis 0.000E+0
Define mr 0.000E+0
Define gsg 0.000E+0
Define comp 0.000E+0
Define K30 0.000E+0
Define gor 0.000E+0
Define lden_vis 0.000E+0
Define com-vis 0.000E+0
Define x-co2 0 ; 1.000E+0
    
```

; EXP GOR correction

```

Restore EOS-C35+

Variable fg 6.15723e-01 ; 6.15171e-01 0.61515 0.61518 ; 6.17242e-01
    
```

```

; GOR correction -SEPG
Multiply moles of N2 to C35+ in SEPG by
fg
Mix Recm-oil 1 Tank SEPG SEPO 1.000 TMOLE

Mix Feed Recm-oil 1.000 Mole
TEMP 130.000 C
Psat
CCE
Basis 1.000 mole
Press Temp GOR WT
psia F scf/bbl
14.700 60.000 735.700 ?gor?
END
    
```

; EXP CCE: Recm-oil

```

Restore EOS-C35+

Mix Feed Recm-oil 1.000 Mole
Temp 130.000 C
Pres 000 bara

CCE
ID "CCE: Recm-oil"
Basis 1.000 Mole
Satp 242.000 bara Weight ?satp?
PRES LSAT GZ K-C16-C22 K-C23-C34 K-C35+ K-C1 K-CO2 K-C2 K-C3 K-C4 K-C5 K-C6
    
```

```

bara      %
WT        0; ?lrvol?   ?gz?
          100.000
232.244  96.932
221.802  93.949
206.687  90.199
194.321  87.216
182.779  83.977
171.237  80.313
160.244  77.074
138.534  69.574
112.427  59.347
92.916   50.313
81.924   45.199

End

;DLE: Recm-oil

Restore   EOS-C35+

Mix       Feed      Recm-oil  1.000    Mole
Temp     130.000    C
Pres     0.000E+0   bara

DLE
ID        " ;DLE: Recm-oil"
Basis    1.480      bbl
Satp     242.000   bara      Weight  ?satp?
PRES     TEMP     MR       LVOL    LDEN    GSG     GZ      WT
bara     C        SCF     bbl     g/cc
WT       0.000E+0  ?mr?   ?lrvol? ?lden?  ?gsg?   ?gz?
395.077  130.000        1.432
384.923  130.000        1.435
375.385  130.000        1.437
364.923  130.000        1.441
354.154  130.000        1.444
344.000  130.000        1.447
333.538  130.000        1.450
323.385  130.000        1.453
313.538  130.000        1.456
304.000  130.000        1.459
294.154  130.000        1.462
283.692  130.000        1.465
273.231  130.000        1.469
263.385  130.000        1.472
252.308  130.000        1.476
242.000  130.000        1.480      6.700E-1
232.000  130.000        1.457
221.846  130.000        1.433
206.462  130.000        1.405

;CCE: Recm-oil

Mix       Feed      Recm-oil  1.000    Mole
Temp     130.000    C
Pres     242.000   bara

CCE
ID        ";CCE: Recm-oil"
Basis    1.000      Mole
Satp     242.000   bara      Weight  ?satp?
PRES     DEN      LDEN
bara     g/cc     g/cc
WT       ?lden?
395.000  6.930E-1
375.000  6.903E-1
350.000  6.872E-1
325.000  6.839E-1
300.000  6.804E-1
275.000  6.761E-1
250.000  6.719E-1
242.000  6.705E-1
230.000  6.596E-1
220.000  6.501E-1
210.000  6.383E-1

END

```

```

-----
; EXP Swelling test Oil-CO2
-----
Restore    EOS-C35+

Mix      Feed      Recm-oil  1 Mole
Temp    130.450    C
Pres    250.38    bara    ; 250.380
Mix      Injectant CO2

SWELL      ID      "CO2 swelling test"
Basis      1.000    Mole
Stg  Press  RMI      PSAT  LSAT  IFT  EQL  EQV  LDens  Z-CO2  WT  ; CO2 mol. Injected
      bara                bara  %    dyne/cm                g/cc                ;
WT      ?satp?      00
1.000    0.000E+0    242    100                ;    0.000E+0
2.000    3.780E-1    288    100                ;    9.600E-2
3.000    6.024E-1    317    100                CO2-36    ;    1.530E-1
4.000    8.386E-1    340    100                ;    2.130E-1
5.000    1.437    387    100                CO2-57    ;    3.650E-1
6.000    1.752    410    100                CO2-62    CO2-63    ;    4.450E-1
7.000    2.220    450    0                CO2-67    ;    5.640E-1
End

Mix CRIT-MIX CO2-62 1 Mole

Variable Fg-crit  9.93852e-01; 0.9985  0.995  0.999  ; 0.284514
Multiply  moles of N2 to C35+  in CRIT-MIX by Fg-crit
Mix Feed 1 Tank CRIT-MIX CO2-67  1 TMOLE
TEMP 130.45 C
Pres 0 bara
CCE
ID " Critical ponit"
Basis 1 mole
PRES TEMP K-C16-C22 K-C23-C34 K-C35+ K-C1 K-CO2 K-C2 K-C3 K-C4 K-C5 K-C6
bara C
WT 0 ?K30? ?K30? ?K30? ?K30? ?K30? ?K30? ?K30? ?K30? ?K30?
130.45 1 1 1 1 1 1 1 1 1 1
END

;CCE test Oil-CO2
Mix      Feed      CO2-36  1.000  Mole
Temp    130.450    C
Pres    0    bara

CCE
ID      "CCE-CO2-36"
Basis  1.000    Mole
Satp   317.000    bara    Weight    ?satp?
PRES   LSAT
bara   %
WT     ?lrvol?
100.00
296.981  93.618
266.053  84.444
237.776  76.966
208.616  69.288
180.781  61.211
160.898  55.328
132.622  46.054
100.810  34.487
92.415   31.296
END

Mix      Feed      CO2-57  1.000  Mole
Temp    130.450    C
Pres    0    bara

CCE
ID      "CCE-CO2-57"
Basis  1.000    Mole
Satp   387.000    bara    Weight    ?satp?
PRES   LSAT
bara   %
WT     ?lrvol?

```

```

100.000
376.735 89.238
346.122 74.170
321.020 68.431
298.980 64.126
272.041 58.984
251.224 54.918
219.388 49.178
201.633 45.112
181.429 40.807
156.327 34.469
129.388 27.653
END

```

```

Mix      Feed      CO2-62    1.000    Mole
Temp    130.450  C
Pres    0      bara
CCE
ID      "CCE-CO2-62"
Basis   1.000    Mole
Satp    410.000  bara      Weight   ?satp?
PRES    LSAT
bara    %
WT      ?lrvol?
100.000
399     85.16
389     71.88
379     68.16
351     62.89
306     56.64
261     49.80
225     43.95
189     38.09
146     27.73
END

```

```

Mix      Feed      CO2-67    1.000    Mole
Temp    130.450  C
Pres    0      bara
CCE
ID      "CCE-CO2-67"
Basis   1.000    Mole
Satp    450.000  bara      Weight   ?satp?
PRES    LSAT
bara    %
WT      ?lrvol?
0.000E+0
449.6
445
423.404 31.101
405.728 45.639
399.100 48.194
383.633 50.573
359.329 50.308
335.025 48.811
307.774 47.577
266.530 42.731
247.381 40.529
212.766 35.595
174.468 29.075
152.373 25.463
106.710 16.212
93.453  13.480
END

```

```

Restore EOS-C35+
Mix      Feed      CO2    1 Mole
Temp    130.45  C
Pres    450    bara
Mix      Injectant  Recm-oil

```

```

SWELL ID "CO2 swelling test"

```

Input Data Sets

A27

```

Basis 1 Mole
Stg Press RMI Psat LSAT IFT EQV Dens Z-CO2 WT
      bara      bara % dyne/cm g/cc
WT      0      ?satp? 1
1      450 0.000      0      0
2      0.058      0      CO2-95      0
3      0.143 605 0      CO2-87
4      0.319 516 0      CO2-75
End
  
```

```

Mix      Feed      CO2-87      1.000      Mole
Temp      130.450      C
Pres      0      bara
CCE
ID      "CCE-CO2-87"
Basis      1.000      Mole
Satp      605.000      bara      Weight 0; ?satp?
PRES      LSAT
bara      %
WT      ?lrvol?
      0.000
502      3.70
483      5.07
454      7.02
401      9.94
362      11.31
317      12.87
269      13.65
241      12.87
210      11.50
  
```

END

```

Mix      Feed      CO2-75      1.000      Mole
Temp      130.450      C
Pres      0      bara
CCE
ID      "CCE-CO2-75"
Basis      1.000      Mole
Satp      516.000      bara      Weight 0 ; ?satp?
PRES      LSAT
bara      %
WT      ?lrvol?
      0.000
469      12.09
446      19.49
398      27.10
355      30.60
318      31.58
283      30.80
243      27.88
212      25.15
184      21.83
173      20.47
112      12.28
  
```

END

```

Mix      Feed      CO2-95      1.000      Mole
Temp      130.450      C
Pres      0      bara
CCE
ID      "CCE-CO2-95"
Basis      1.000      Mole
Satp      320.000      bara      Weight 0; ?satp?
PRES      LSAT
bara      %
WT      ?lrvol?
      0.000
318      1.36
291      1.75
252      2.53
225      2.34
203      2.73
  
```

```

182      2.53
END

-----
; EXP Viscosity
-----
Restore  EOS-C35+

Mix      Feed      Recm-oil  1.000    Mole
Temp    130.000    C
Pres    300.000    bara

DLE
ID      "Viscosity-Recm-oil"
Basis   1.000    Mole
Satp    242.000    bara      Weight    0.000E+0
PRES    TEMP      LVIS      LDEN      GDEN      GMDens    LMDens    ; Weight
bara    C          cp        g/cc     g/cc     gmol/cm3   gmol/cm3
WT      0.000E+0    ?lvis-1? ?lden?
300.000 130.000    3.500E-1 6.800E-1

END

-----
; Creating mixtrure for Viscosity Experiment
-----
Restore  EOS-C35+
Variable fg-6    5.20019e-02 ; 0.000E+0 1.000 ; 5.18564e-02
Variable fg-11  1.10495e-01 ; 0.000E+0 1.000 ; 1.10359e-01
Variable fg-17  1.71006e-01 ; 0.000E+0 1.000 ; 1.70879e-01
Variable fg-27  2.65806e-01 ; 0.000E+0 1.000 ; 2.65693e-01
Variable fg-46  4.87789e-01 ; 0.000E+0 1.000 ; 4.90852e-01
Variable fg-58  6.63342e-01 ; 0.000E+0 1.000 ; 6.67081e-01
Variable fg-65  8.29761e-01 ; 0.000E+0 1.000 ; 8.41806e-01

Mix CO2-6 CO2
Multiply moles of CO2 in CO2-6 by fg-6
Mix CO2-6 1 Tank CO2-6 Recm-oil 1.000 TMOLE

Mix      Feed      CO2-6    1.000    Mole
Temp    130.000    C
Pres    300.000    bara
DLE     ID      "Viscosity-CO2-6"
Basis   1.000    Mole
PRES    TEMP      LVIS      LDEN      X-CO2
bara    C          cp        g/cc
WT      0.000E+0    ?lvis? ?lden_vis? ?x-co2?
300.000 130.000    3.300E-1 6.650E-1 0.06

End

Mix CO2-11.8 CO2
Multiply moles of CO2 in CO2-11.8 by fg-11
Mix CO2-11.8 1 Tank CO2-11.8 Recm-oil 1.000 TMOLE

Mix      Feed      CO2-11.8 1.000    Mole
Temp    130.000    C
Pres    300.000    bara
DLE     ID      "Mixture of X-CO2 = 11.8"
Basis   1.000    Mole
PRES    TEMP      LVIS      LDEN      X-CO2
bara    C          cp        g/cc
WT      0.000E+0    ?lvis? ?lden_vis? ?x-co2?
300.000 130.000    3.100E-1 0.650 0.118

End

Mix CO2-17.8 CO2
Multiply moles of CO2 in CO2-17.8 by fg-17
Mix CO2-17.8 1 Tank CO2-17.8 Recm-oil 1.000 TMOLE

Mix      Feed      CO2-17.8 1.000    Mole
Temp    130.000    C
Pres    300.000    bara

```

Input Data Sets

A29

```
DLE      ID      "Mixture of X-CO2 = 17.8"
Basis    1.000    Mole
PRES     TEMP     LVIS      LDEN      X-CO2
bara     C          cp        g/cc
WT       0.000E+0    ?lvis?   ?lden_vis? ?x-co2?
300.000  130.000    2.800E-1 0.635     0.178
```

End

```
Mix CO2-27.2 CO2
Multiply moles of CO2 in CO2-27.2 by fg-27
Mix CO2-27.2 1 Tank CO2-27.2 Recm-oil 1.000 TMOLE
```

```
Mix      Feed    CO2-27.2    1.000    Mole
Temp     130.000    C
Pres     300.000    bara
DLE      ID      "Mixture of X-CO2 = 27.2"
Basis    1.000    Mole
PRES     TEMP     LVIS      LDEN      X-CO2
bara     C          cp        g/cc
WT       0.000E+0    ?lvis?   ?lden_vis? ?x-co2?
300.000  130.000    1.800E-1 0.612     0.272
```

End

```
Mix CO2-46.8 CO2
Multiply moles of CO2 in CO2-46.8 by fg-46
Mix CO2-46.8 1 Tank CO2-46.8 Recm-oil 1.000 TMOLE
```

```
Mix      Feed    CO2-46.8    1.000    Mole
Temp     130.000    C
Pres     300.000    bara
DLE      ID      "Mixture of X-CO2 = 11.8"
Basis    1.000    Mole
PRES     TEMP     LVIS      LDEN      X-CO2
bara     C          cp        g/cc
WT       0.000E+0    ?lvis-1? ?lden_vis? ?x-co2?
300.000  130.000    2.400E-1 0.624     0.468
```

End

```
Mix CO2-58.1 CO2
Multiply moles of CO2 in CO2-58.1 by fg-58
Mix CO2-58.1 1 Tank CO2-58.1 Recm-oil 1.000 TMOLE
```

```
Mix      Feed    CO2-58.1    1.000    Mole
Temp     130.000    C
Pres     300.000    bara
DLE      ID      "Mixture of X-CO2 = 58.1"
Basis    1.000    Mole
PRES     TEMP     LVIS      LDEN      X-CO2
bara     C          cp        g/cc
WT       0.000E+0    ?lvis?   ?lden_vis? ?x-co2?
300.000  130.000    2.900E-1 0.735     0.581
```

End

```
Mix CO2-65.9 CO2
Multiply moles of CO2 in CO2-65.9 by fg-65
Mix CO2-65.9 1 Tank CO2-65.9 Recm-oil 1.000 TMOLE
```

```
Mix      Feed    CO2-65.9    1.000    Mole
Temp     130.000    C
Pres     300.000    bara
DLE      ID      "Mixture of X-CO2 = 65.9"
Basis    1.000    Mole
PRES     TEMP     LVIS      LDEN      X-CO2
bara     C          cp        g/cc
WT       0.000E+0    ?lvis-1? ?lden_vis? ?x-co2?
300.000  130.000    3.700E-1 0.759     0.659
```

End

```
Mix Feed CO2
Temp 130 C
Pres 450 bara
CCE
Pres Temp GDens LDens Dens Lvis Vis GMDens LMDens
bara C g/cc g/cc g/cc cp cp gmol/cm3 gmol/cm3
WT 0 0 0
450 130 0.7 0.7
300 130
End

Mix Feed Recm-oil 1.000 Mole
Temp 130.000 C
Pres 300.000 bara
Mix Solvent CO2
MMP 50
;MMP 100
;MMP 500

END
```


Input Data Set Used to Model Haft Kel Matrix-Fracture
System (without Diffusion) in Chapter 6
Base case SENSOR input data set


```

TITLE
Haft kel simulation without diffusion
Half block model
11 Component EOS
Base:
- A1 : Nx = 10
- B1 : Nz = 50
- C1 : Kma = 0.8 md
- D1 : Hma = 8 ft
- E1 : Pinit = 1400 psia
- F1 : Inj gas = Eq gas
- G1 : No blocKs = 1
- H1 : Displacement=2D
ENDTITLE

C -----
C Dimension and Solution Options
C -----

GRID 10 1 50

CPU

IMPLICIT

MAPSPRINT 1 SO P GG GO TENS X Y TENS TX TZ PCGO ! Initialization output

C -----
C Grid Block Properties
C -----
DELX XVAR
9*0.4444444 0.01
DELY CON
8
DEPTH CON
1000
THICKNESS ZVAR
0.01 48*0.166667 0.01
KX CON
100000
MOD
1 9 1 1 2 49 = 0.8
KY EQUALS KX
KZ EQUALS KX
POROS CON
1.
MOD
1 9 1 1 2 49 = 0.10

C -----
C Regions: Region 1 = Matrix, Region 2 = Fracture
C -----
ROCKTYPE CON ! Rock (saturation table) regions
2
MOD
1 9 1 1 2 49 = 1
REGION CON ! Initialization regions
2
MOD
1 9 1 1 2 49 = 1
INITREG CON ! Fluid in place regions
2
MOD
1 9 1 1 2 49 = 1

C -----
C Rel-perm and capillary pressure data
C -----
! Rock type 1 (Matrix)
KRANALYTICAL 1
0.2 0.2 0.2 0.05 ! Swc Sorw Sorg Sgc
1.0 0.653 1 ! krw(Sorw) krg(Swc) kro(Swc)
2.0 2.0 1.3 3.98 ! nw now ng nog
0.397 4.166 1.079 PCGO ! c1 c2 c3 gas-oil

! Rock type 2 (Fracture, Pc = 0)
KRANALYTICAL 2

```

```

0.0 0.0 0.0 0.0          ! Swc Sorw Sorg Sgc
1.0 1.0 1.0             ! krw(Sorw) krg(Swc) kro(Swc)
1.0 1.0 1.0 1.0        ! nw now ng nog

! Interfacial tension scaling
TENSION 10 30          ! ref_tension, max_tension

C -----
C Fluid PVT data
C -----
PVTEOS SRK
110                    ! Reservoir temperature deg F

CPT          PC      TC      MW      AC      SHIFT  ZCRIT      PCHOR  OMEGA      OMEGB
C           psia      R
N2          492.84  227.16  28.014  0.03700 -0.00090 0.29178   59.10  0.4274700  0.0866400
CO2         1069.51  547.42  44.010  0.22500  0.21749 0.27433   80.00  0.4274700  0.0866400
H2S         1299.97  672.12  34.082  0.09000  0.10153 0.28292   80.10  0.4274700  0.0866400
C1          667.03  343.01  16.043  0.01100 -0.00247 0.28620   71.00  0.4274700  0.0866400
C2          706.62  549.58  30.070  0.09900  0.05894 0.27924  111.00  0.4274700  0.0866400
C3          616.12  665.69  44.097  0.15200  0.09075 0.27630  151.00  0.4274700  0.0866400
C4-C6       527.88  840.66  70.433  0.21405  0.09829 0.27403  216.05  0.4274802  0.0866404
C7-C14      411.95  1147.73 136.819  0.35302  0.09872 0.29826  384.35  0.4274802  0.0866404
C15-C21     283.74  1395.61 239.679  0.60452  0.13147 0.29826  657.60  0.4274801  0.0866403
C22-C29     225.55  1546.43 341.306  0.81842  0.12980 0.29826  855.51  0.4274801  0.0866404
C30+        184.60  1692.33 487.101  1.06576  0.09103 0.29826 1062.75  0.4274810  0.0866404

BIN
0.00000 0.00000 0.02500 0.01000 0.09000 0.10401 0.11000 0.11000 0.11000 0.11000
      0.12000 0.10500 0.13000 0.12500 0.11541 0.11500 0.11500 0.11500 0.11500
            0.08000 0.07000 0.07000 0.05436 0.05000 0.05000 0.05000 0.05000
                  0.00000 0.00000 0.00000 0.00000 0.00000 0.00000 0.00000 0.00000
                        0.00000 0.00000 0.00000 0.00000 0.00000 0.00000
                              0.00000 0.00000 0.00000 0.00000
                                  0.00000 0.00000 0.00000
                                      0.00000 0.00000
                                          0.00000 0.00000
                                              0.00000

C -----
C Initialisation
C -----

INITIAL 1
!depth psat  N2      CO2      H2S      C1      C2      C3      C4-C6  C7-C14  C15-C21  C22-C29  C30+
DEPTH
1000 1406 0.000936 0.004250 0.012956 0.295681 0.049689 0.050642 0.128152 0.334292 0.088677
0.026569 0.008156
PINIT 1406
ZINIT 1000

INITIAL 2
!depth psat  N2      CO2      H2S      C1      C2      C3      C4-C6  C7-C14  C15-C21  C22-C29  C30+
DEPTH
1000 1406 0.00753 0.00645 0.00820 0.89991 0.04511 0.02012 0.01169 0.00098 0.000 0.000 0.000
PINIT 1406
ZINIT 1000
ENDINIT

MODIFY PV
10 10 1 1 2 49 * 1E8 ! Vertical fracture
1 10 1 1 1 1 * 1E8 ! Top fracture
1 10 1 1 50 50 * 1E8 ! Bottom fracture

C -----
C Output specifications
C -----
! PSM
MAPSFREQ 1
MAPSFILE SAT SG SO TENS GO GG
MAPSFILEFREQ 1 ! maps written to fort.71

C          days      freq
TIME      3650      30
TIME      5000      100
TIME      10000     300
END

```

Input Data Set Used to Model Haft Kel Matrix-Fracture
System (with Diffusion) in Chapter 7
Base case ECLIPSE 300 input data set


```

RUNSPEC

-- Using Haft Kel rock type and matrix dimension
-- Half block model
-- 11 Component EOS
-- Diff-f2g3h2-ecl:
--   - A1 : Nx = 10
--   - B1 : Nz = 100
--   - C1 : Kma = 0.8 md
--   - D1 : Matrix Dim. = 8x8 ft
--   - E1 : Pinit = 1000 psia
--   - F1 : Inj gas = CO2 gas
--   - G3 : Diffusion = Chemical potential
--   - H2 : Fluid = Haft Kel

MESSAGES
8* 100000 /

--IMPES
FULLIMP

DIMENS
  11  1  102 /

-- Phases present
WATER
OIL
GAS

OPTIONS3
--switch 4      19      26      68      74
4*      14* 0  6* 2  41* 1  5* 1 /

--Enables molecular diffusion
DIFFUSE

-- Units
FIELD

-- Define Component in EOS
COMPS
11 /

REGDIMS
-- Max.FIPREG  FIPREG
  2      2      0      2/

TABDIMS
--No.sat.tab  No.pvt.tab  max.sat.nods  max.sat.nods  Max.FIPREG
  2      1      50      50      2/

EQLDIMS
---Eqrqn  Deptab
  2      50 /

WELLDIMS
5  20  3*  20/

MISCIBLE
/
RSSPEC

FMTOUT

-- To unified output files
UNIFOUT

GRID  =====

--Requests output of an INIT file (Need for FloViz)
INIT

RPTGRID
DX DZ PERMR PERMZ PORO PORV TRANR TRANZ NNC /

```

```

MINPORV
0.000000001/
-- SPECIFY GRID BLOCK DIMENSIONS IN THE R DIRECTION
DXV
10*0.4 0.01 / ft
DYV
8.0/
DZV
0.01 100*0.08 0.01 / FT

EQUALS
TOPS      10000      1 11 1 1 1 1 /
PORO      1.0        1 11 1 1 1 102 /      Fracture porosity
PORO      0.10       1 10 1 1 2 101 /      Martix porosity
PERMX     100000     1 11 1 1 1 102 /      Fracture permeabiliy
PERMX     0.8        1 10 1 1 2 101 /      Martix permeabiliy
/
COPY
'PERMX'   'PERMY' /
'PERMX'   'PERMZ' /
/
GRIDFILE
2 /
PROPS =====
MESSAGES
8* 100000 /
EOS
SRK /
-- Reservoir temperatures Deg F
RTEMP
110 /
CNAMEs
N2  CO2  H2S  C1  C2  C3  C4-C6  C7-C14  C15-C21  C22-C29  C30+ /

-- Critical temperatures Deg R
TCRIT
227.16  547.42  672.12  343.01  549.58  665.69  840.66  1147.73  1395.61  1546.43  1692.33 /

-- Critical pressures psia
PCRIT
492.84  1069.51  1299.97  667.03  706.62  616.12  527.88  411.95  283.74  225.55  184.6 /

-- Critical Z-factors
ZCRIT
0.29178  0.27433  0.28292  0.2862  0.27924  0.2763  0.27403  0.25616  0.23658  0.22253  0.20718 /

ZCRITVIS
0.29178  0.27433  0.28292  0.2862  0.27924  0.2763  0.27403  0.29826  0.29826  0.29826  0.29826 /

-- 3-Parameter EoS Shift Coefficients
SSHIFT
-0.0009  0.21749  0.10153  -0.00247  0.05894  0.09075  0.09829  0.09872  0.13147  0.1298  0.09103 /

-- Acentric factors
ACF
0.037  0.225  0.09  0.011  0.099  0.152  0.21405  0.35302  0.60452  0.81842  1.06576 /

-- Molecular Weights
MW
28.014  44.01  34.082  16.043  30.07  44.097  70.433  136.819  239.679  341.306  487.101 /

-- Parachors (Dynes/cm)
PARACHOR
59.1  80  80.1  71  111  151  216.05  384.35  657.6  855.51  1062.75 /

-- Binary Interaction Coefficients
BIC
0.00000
0.00000  0.12000
0.02500  0.10500  0.08000
0.01000  0.13000  0.07000  0.0000
0.09000  0.12500  0.07000  0.0000  0.0000
0.10401  0.11541  0.05436  0.0000  0.0000  0.0000
0.11000  0.11500  0.05000  0.0000  0.0000  0.0000  0.0000
0.11000  0.11500  0.05000  0.0000  0.0000  0.0000  0.0000  0.0000

```



```

0.11000  0.11500  0.05000  0.0000  0.0000  0.0000  0.0000  0.0000  0.0000
0.11000  0.11500  0.05000  0.0000  0.0000  0.0000  0.0000  0.0000  0.0000  0.0000 /

--Interfacial tension scaling
MISCSTR
--ref_tension, max_tension
10 30 107/
-- (IFT/IFT.ref)^n in rel perm.; n=MISCEXP
MISCEXP
0/

SGOF
--Sg      Krg      Krog      Pcog
0.0      0.0      1.0      0.0
0.01     0.0      0.99     0.0
0.1      0.1      0.9      0.0
0.2      0.2      0.8      0.0
0.3      0.3      0.7      0.0
0.4      0.4      0.6      0.0
0.5      0.5      0.5      0.0
0.6      0.6      0.4      0.0
0.7      0.7      0.3      0.0
0.8      0.8      0.2      0.0
0.9      0.9      0.1      0.0
1.0      1.0      0.0      0.0 / table 1 (fracture)
0.0000   0.0000   1.0000   0.397
0.0400   0.0000   0.7599   0.561
0.0500   0.0000   0.7073   0.606
0.1200   0.0448   0.4114   0.935
0.1600   0.0806   0.2910   1.131
0.2000   0.1206   0.1991   1.330
0.2400   0.1640   0.1309   1.533
0.2800   0.2102   0.0819   1.739
0.3200   0.2589   0.0482   1.947
0.3600   0.3099   0.0261   2.157
0.4000   0.3629   0.0126   2.369
0.4400   0.4177   0.0052   2.583
0.4800   0.4742   0.0017   2.798
0.5200   0.5323   0.0003   3.014
0.5600   0.5919   0.0000   3.232
0.6000   0.6530   0.0000   3.451
0.6400   0.7154   0.0000   3.672
0.6800   0.7791   0.0000   3.893
0.7200   0.8440   0.0000   4.115
0.7600   0.9101   0.0000   4.339
0.8000   1.0000   0.0000   4.563 / table 2 (Matrix)

SWOF
--Sw      Krw      Krow      Pcow
0.0      0.0      1.0      0
0.01     0.0      0.99     0
0.1      0.1      0.9      0.0
0.2      0.2      0.8      0
0.3      0.3      0.7      0
0.4      0.4      0.6      0
0.5      0.5      0.5      0
0.6      0.6      0.4      0
0.7      0.7      0.3      0
0.8      0.8      0.2      0.0
0.9      0.9      0.1      0.0
1.0      1.0      0.0      0.0 / table 1 (fracture)
0.2000   0.0000   1.0000   0.000
0.2400   0.0044   0.8711   0.000
0.2800   0.0178   0.7511   0.000
0.3200   0.0400   0.6400   0.000
0.3600   0.0711   0.5378   0.000
0.4000   0.1111   0.4444   0.000
0.4400   0.1600   0.3600   0.000
0.4800   0.2178   0.2844   0.000
0.5200   0.2844   0.2178   0.000
0.5600   0.3600   0.1600   0.000
0.6000   0.4444   0.1111   0.000
0.6400   0.5378   0.0711   0.000
0.6800   0.6400   0.0400   0.000
0.7200   0.7511   0.0178   0.000
0.7600   0.8711   0.0044   0.000
0.8000   1.0000   0.0000   0.000

```

```

0.8400 1.0000 0.0000 0.000
0.8800 1.0000 0.0000 0.000
0.9200 1.0000 0.0000 0.000
0.9600 1.0000 0.0000 0.000
1.0000 1.0000 0.0000 0.000 / table 2 (Matrix)

FACTLI
1 0.9/

DIFFGAS
-- N2 CO2 H2S C1 C2 C3 C4-C6 C7-C14 C15-C21 C22-C29 C30+
(field units: 1 cm2/s = 92.9979 ft2/Day)
0.02180 0.01598 0.01579 0.01459 0.01508 0.01191 0.00908 0.00611 0.00427 0.00343 0.00279/

DIFFOIL
-- N2 CO2 H2S C1 C2 C3 C4-C6 C7-C14 C15-C21 C22-C29 C30+ -
--(field units: 1 cm2/s = 92.9979 ft2/Day)
0.00034 0.00023 0.00023 0.00032 0.00023 0.00017 0.00012 0.00010 0.00006 0.00005 0.00004/

REGIONS =====
-- Region 2= Matrix
-- Region 1= Fracture
EQUALS
FIPNUM 1 / Fluid In Place reg. no.
FIPNUM 2 1 10 1 1 2 101 / Fluid In Place reg. no.
SATNUM 1 / Saturation reg. no.
SATNUM 2 1 10 1 1 2 101 / Saturation reg. no.
EQLNUM 1 /
EQLNUM 2 1 10 1 1 2 101 /
/

SOLUTION =====
DATUMR
10000.0 10000.01 /
PRESSURE
1122*1000 /
EQUALS
SWAT 0/
SWAT 0.2 1 10 1 1 2 101/
SOIL 0.0/
SOIL 0.8 1 10 1 1 2 101/
/
--N2 CO2 H2S C1 C2 C3 C4-C6 C7-C14 C15-C21 C22-C29 C30+
NEI
0.0000 1.0000 0.0000 0.0000 0.0000 0.0000 0.0000 0.0000 0.0000 0.0000 0.0000/
0.000430 0.003867 0.013348 0.221131 0.049395 0.054161 0.142768 0.376053 0.099776 0.029894
0.009177 /

RPTSOL
PRESSURE SOIL SGAS PSAT XMF YMF ZMF/

RPTRST
BASIC=2 SOIL PCOG/

SUMMARY =====
MESSAGES
8* 100000 /
--data be written to the Summary file only at report time
RPTONLY
--ALL
FOPR
FOPT
FGPT
FPR

ROSAT
/
ROIP
/
ROIPL
/

WBHP
/

```

```

WGPR
/
WGIR
/

RUNSUM
EXCEL

SCHEDULE =====
----- THE SCHEDULE SECTION DEFINES THE OPERATIONS TO BE SIMULATED
-----

MESSAGES
8* 100000 /

WELSPCLS
PROD Field 1 1 1* GAS /
GINJ Field 1 1 1* GAS /
/
-- defining gas injection composition
WELLSTRE
--well St.name N2 CO2 H2S C1 C2 C3 C4-C6 C7-C14 C15-C21 C22-C29 C30+
--EQV 0.00497991 0.00730661 0.00982485 0.89132114 0.05203481 0.02252617 0.0113755
--0.00063026 0.00000075 0.0000 0.0000 /
CO2-gas 0.0000 1.0000 0.0000 0.0000 0.0000 0.0000 0.0000 0.0000 0.0000 0.0000 0.0000 /
/

COMPDAT
--Well name I J K1 K2 Status SatTable PI
PROD 1 1 102 102 OPEN 1 100 /
PROD 2 1 102 102 OPEN 1 100 /
PROD 3 1 102 102 OPEN 1 100 /
PROD 4 1 102 102 OPEN 1 100 /
PROD 5 1 102 102 OPEN 1 100 /
PROD 6 1 102 102 OPEN 1 100 /
PROD 7 1 102 102 OPEN 1 100 /
PROD 8 1 102 102 OPEN 1 100 /
PROD 9 1 102 102 OPEN 1 100 /
PROD 10 1 102 102 OPEN 1 100 /
PROD 11 1 102 102 OPEN 1 100 /
GINJ 1 1 1 1 OPEN 1 100 /
GINJ 2 1 1 1 OPEN 1 100 /
GINJ 3 1 1 1 OPEN 1 100 /
GINJ 4 1 1 1 OPEN 1 100 /
GINJ 5 1 1 1 OPEN 1 100 /
GINJ 6 1 1 1 OPEN 1 100 /
GINJ 7 1 1 1 OPEN 1 100 /
GINJ 8 1 1 1 OPEN 1 100 /
GINJ 9 1 1 1 OPEN 1 100 /
GINJ 10 1 1 1 OPEN 1 100 /
GINJ 11 1 1 1 OPEN 1 100 /
/

WCONPROD
--Wellname status control oil-s.rate wat-s.rate gas-s.rate liq-s.rate res.rate BHP
--Unit stb/d stb/d Mscf/d stb/d rrbbl/d
psia
PROD OPEN BHP 2* 50.00 2*
1000.50/ GRAT
/

WCONINJE
--Wellname type status control Surf.rate res.rate BHP
--Unit Mscf/d rrbbl/d psia
GINJ GAS OPEN RATE 3.0 1* 100000.0/
/

WINJGAS
-- Well name Stream Stream name
GINJ STREAM CO2-gas/
/

-- Creat Restart file
RPTRST
BASIC=2 SOIL/

```

```
RPTPRINT
8*/

RPTSCHED
'CPU=1' 'FIP=3' 'SOIL' PRES 'WELLS=5' PSAT PCOG STEN 'ZMF' XMF YMF DENG DENO /
IFTGO KRO KRG MULT

--TUNING
--8* /
--4* /
--2* 200000 /

TSCRIT
--ini min max
0.001 0.001 /0.2

--TSTEP
--5*1 /

TSTEP
12*10 68*10 34*50 60*100 60*100 55*100 30*1000 / 2000 days

END
```

Input Data Set Used to Model Laboratory System with
Synthetic C₁-C₅ mixture (with Diffusion) in Chapter 7
Base case ECLIPSE 300 input data set


```

RUNSPEC

-- Using Haft kel rock type and matrix dimension
-- Lab model
-- 4 Component EOS
-- Diff-d2f2g3-ecl:
--   - A1 : Nx = 10
--   - B1 : Nz = 100
--   - C1 : Kma = 0.8 md
--   - D2 : Matrix Dim. = 0.2x2 ft
--   - E1 : Pinit = 1000 psia =68.05 atma
--   - F2 : Inj gas = CO2 gas
--   - G3 : Diffusion = Chemical potential

FULLIMP
DIMENS
  11  1  102  /

-- Phases present
WATER
OIL
GAS

OPTIONS3
--switch 19  21  26  46  68  74
18*  0  1* 200 4* 2  19* 200 21* 1  5* 1 /

--Enables molecular diffusion
DIFFUSE

CART
-- Units
--FIELD
LAB

-- Define Component in EOS
COMPS
4  /

REGDIMS
-- Max.FIPREG  FIPREG
  2  2  0  2/

TABDIMS
--No.sat.tab  No.pvt.tab  max.sat.nods  max.sat.nods  Max.FIPREG
2  1  50  50  2/

EQLDIMS
----Eqrqn  Deptab
  2  50  /

WELLDIMS
5  20  3*  20/

MISCIBLE
/

RSSPEC
FMTOUT
-- To unified output files
UNIFOUT

GRID  =====
--Requests output of an INIT file (Need for FloViz)
INIT

RPTGRID
DX DZ PERMR PERMZ PORO PORV TRANR  TRANZ NNC  /

MINPORV
0.000000001/

-- SPECIFY GRID BLOCK DIMENSIONS IN THE R DIRECTION
DXV
10*0.3048 0.3048  / cm
DYV

```

```

6.096/
DZV
0.3048 100*0.6096 0.3048 / cm
EQUALS
  TOPS      1      1 11 1 1 1 1 /
  PORO      1.0    1 11 1 1 1 102 / Fracture porosity
  PORO      0.10   1 10 1 1 2 101 / Martix porosity
  PERMX     100000 1 11 1 1 1 102 / Fracture permeabiliy
  PERMX     0.8    1 10 1 1 2 101 / Martix permeabiliy
/
COPY
  'PERMX' 'PERMY' /
  'PERMX' 'PERMZ' /
/
GRIDFILE
2 /

PROPS =====
EOS
SRK /
-- Reservoir temperatures Deg C
RTEMP
85 /

CNAMEs
C1 C5 CO2 N2 /

-- Critical temperatures Deg K
TCRIT
190.56      470.14      304.12      126.20      /

-- Critical pressures atma
PCRIT
45.3886     34.2407     72.7757     33.5357     /

-- Critical Z-factors
ZCRIT
0.2862     0.27119     0.27433     0.29178     /

-- 3-Parameter EoS Shift Coefficients
SSHIFT
-0.00247     0.11942     0.21749     -0.0009     /

-- Acentric factors
ACF
0.011     0.22895     0.225     0.037     /

-- Molecular Weights
MW
16.043     70.905     44.01     28.014     /

-- Parachors (Dynes/cm)
PARACHOR
71     205.17     80     59.1     /

-- Binary Interaction Coefficients
BIC
0.0
0.12000     0.15000
0.02000     0.08000     0.00000/

--Interfacial tension scaling
MISCSTR
--ref_tension, max_tension
10 30 114/

-- (IFT/IFT.ref)^n in rel perm.; n=MISCEXP
MISCEXP
0/

SGOF
--Sg      Krg      Krog      Pcog
0.0      0.0      1.0      0
0.01     0.0      0.99     0
0.1      0.1      0.9      0.0
0.2      0.2      0.8      0

```



```

0.3      0.3      0.7      0
0.4      0.4      0.6      0
0.5      0.5      0.5      0
0.6      0.6      0.4      0
0.7      0.7      0.3      0
0.8      0.8      0.2      0.0
0.9      0.9      0.1      0.0
1.0      1.0      0.0      0.0 / table 1 (fracture)
0.0000   0.0000   1.0000   0.0270
0.0400   0.0000   0.7599   0.0382
0.0500   0.0000   0.7073   0.0412
0.1200   0.0448   0.4114   0.0636
0.1600   0.0806   0.2910   0.0770
0.2000   0.1206   0.1991   0.0905
0.2400   0.1640   0.1309   0.1043
0.2800   0.2102   0.0819   0.1183
0.3200   0.2589   0.0482   0.1325
0.3600   0.3099   0.0261   0.1468
0.4000   0.3629   0.0126   0.1612
0.4400   0.4177   0.0052   0.1758
0.4800   0.4742   0.0017   0.1904
0.5200   0.5323   0.0003   0.2051
0.5600   0.5919   0.0000   0.2199
0.6000   0.6530   0.0000   0.2348
0.6400   0.7154   0.0000   0.2499
0.6800   0.7791   0.0000   0.2649
0.7200   0.8440   0.0000   0.2800
0.7600   0.9101   0.0000   0.2953
0.8000   1.0000   0.0000   0.3105 / table 2 (Matrix)

SWOF
--Sw      Krw      Krow      Pcow
0.0      0.0      1.0      0
0.01     0.0      0.99     0
0.1      0.1      0.9      0.0
0.2      0.2      0.8      0
0.3      0.3      0.7      0
0.4      0.4      0.6      0
0.5      0.5      0.5      0
0.6      0.6      0.4      0
0.7      0.7      0.3      0
0.8      0.8      0.2      0.0
0.9      0.9      0.1      0.0
1.0      1.0      0.0      0.0 / table 1 (fracture)
0.2000   0.0000   1.0000   0.000
0.2400   0.0044   0.8711   0.000
0.2800   0.0178   0.7511   0.000
0.3200   0.0400   0.6400   0.000
0.3600   0.0711   0.5378   0.000
0.4000   0.1111   0.4444   0.000
0.4400   0.1600   0.3600   0.000
0.4800   0.2178   0.2844   0.000
0.5200   0.2844   0.2178   0.000
0.5600   0.3600   0.1600   0.000
0.6000   0.4444   0.1111   0.000
0.6400   0.5378   0.0711   0.000
0.6800   0.6400   0.0400   0.000
0.7200   0.7511   0.0178   0.000
0.7600   0.8711   0.0044   0.000
0.8000   1.0000   0.0000   0.000
0.8400   1.0000   0.0000   0.000
0.8800   1.0000   0.0000   0.000
0.9200   1.0000   0.0000   0.000
0.9600   1.0000   0.0000   0.000
1.0000   1.0000   0.0000   0.000 / table 2 (Matrix)

FACTLI
1 0.9/

DIFFGAS
-- C1      C5      CO2      N2 (cm2/hr)
1.0505   1.0505   0.8087   0.000/

DIFFOIL
-- C1      C5      CO2      N2 (cm2/hr)
0.07152  0.07152  0.05539  0.000/

```

```

REGIONS =====
-- Regoin 2= Matrix
-- Regoin 1= Fracture
EQUALS
FIPNUM 1 / Fluid In Place reg. no.
FIPNUM 2 1 10 1 1 2 101 / Fluid In Place reg. no.
SATNUM 1 / Saturation reg. no.
SATNUM 2 1 10 1 1 2 101 / Saturation reg. no.
EQLNUM 1 /
EQLNUM 2 1 10 1 1 2 101 /
/

SOLUTION =====
DATUMR
1.0 1.01 /

PRESSURE
1122*68.05 / atma
EQUALS
SWAT 0/
SWAT 0.2 1 10 1 1 2 101/
SOIL 0.0/
SOIL 0.8 1 10 1 1 2 101/
/

NEI
0.0000 0.0000 1.0000 0.0000/
0.27350364 0.72649636 0.0000 0.0000/

RPTSOL
PRESSURE SOIL SGAS PSAT XMF YMF ZMF/

RPTRST
BASIC=2 SOIL PCOG/

SUMMARY =====
--data be written to the Summary file only at report time
RPTONLY
--ALL
FOPR
FOPT
FGPT
FPR
ROSAT
/
ROIP
/
ROIPL
/
WBHP
/
WGPR
/
WGIR
/

RUNSUM
EXCEL

SCHEDULE =====
----- THE SCHEDULE SECTION DEFINES THE OPERATIONS TO BE SIMULATED
-----

WELSPEDS
PROD Field 1 1 1* GAS /
GINJ Field 1 1 1* GAS /
/
-- defining gas injection composition
WELLSTRE
--well St.name Z-C1 Z-nC7 Z-CO2 Z-N2
EQV 0.86284482 0.13715518 0.0000 0.0000/
CO2-gas 0.0000 0.0000 1.0000 0.0000 /
/

COMPDAT
--Well name I J K1 K2 Status SatTable PI
PROD 1 1 102 102 OPEN 1 10000000 /

```

```
GINJ      1 1 1 1 OPEN 1      10000000 /
/

WCONPROD
--Wellname status control oil-s.rate wat-s.rate gas-s.rate liq-s.rate res.rate BHP
--Unit      scc/hr      scc/hr      scc/hr      scc/hr      rcc/hr      atma
PROD      OPEN      BHP      2*          2*          2*          600      68.05/
/

WCONINJE
--Wellname type status control Surf.rate res.rate BHP
--Unit      scc/hr      rcc/hr      atma
GINJ      GAS      OPEN      RESV      1*          30      1000.00/
/

WINJGAS
-- Well name Stream Stream name
GINJ      STREAM CO2-gas/
/

-- Creat Restart file
RPTRST
BASIC=2 SOIL/

RPTPRINT
8*/

RPTSCHED
'CPU=1' 'FIP=3' 'SOIL' PRES 'WELLS=5' PSAT PCOG STEN KRO KRG 'ZMF' XMF YMF MULT
/ IPTGO

TUNING
8* /
4* /
50 1* 2000 /

TSCRIT
--ini min max
0.05 0.05 0.05 /

TSTEP
50*2.4 /

END
```


Appendix B

Papers

Paper I

CO₂ EOR Potential in Naturally-Fractured Haft Kel Field, Iran

SPE Reservoir Evaluation and Engineering: 720-729. SPE-139528-PA

Is not included due to copyright

Modeling CO₂ Injection in a Fractured-Chalk Experiment

*Paper SPE 125362 presented at the 2009 SPE/EAGE Reservoir Characterization and
Simulation Conference, Abu Dhabi, UAE, 19–21 October*

Paper II

Is not included due to copyright

Scale Dependence of Diffusion in Naturally
Fractured Reservoirs for CO₂ Injection

*Paper SPE 129666 presented at the 2010 SPE Improved Oil Recovery Symposium,
Tulsa, Oklahoma, USA, 24–28 April*

Paper III

Is not included due to copyright

Modeling CO₂ Injection Including Diffusion
in a Fractured-Chalk Experiment

*Paper SPE 135339 presented at the 2010 Annual Technical Conference and Exhibition,
Florence, Italy, 19–22 September*

Paper IV

Is not included due to copyright

